

WL-TR-95-2011

NUMERICAL UNSTEADY AERODYNAMIC
SIMULATOR FOR BLADE FORCED RESPONSE PHENOMENA



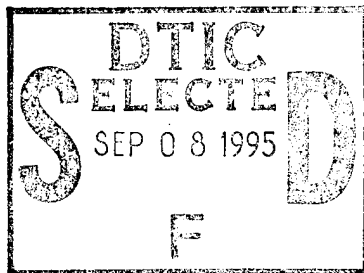
T. C. AYER
J. M. VERDON

UNITED TECHNOLOGIES RESEARCH CENTER
EAST HARTFORD CT 06108

DECEMBER 1994

FINAL REPORT FOR 06/01/92-12/01/94

APPROVED FOR PUBLIC RELEASE; DISTRIBUTION IS UNLIMITED.



AEROPROPULSION AND POWER DIRECTORATE
WRIGHT LABORATORY
AIR FORCE MATERIEL COMMAND
WRIGHT PATTERSON AFB OH 45433-7251

DTIC QUALITY INSPECTED 5

19950906 047

NOTICE

When Government drawings, specifications, or other data are used for any purpose other than in connection with a definitely Government-related procurement, the United States Government incurs no responsibility or any obligation whatsoever. The fact that the government may have formulated or in any way supplied the said drawings, specifications, or other data, is not to be regarded by implication, or otherwise in any manner construed, as licensing the holder, or any other person or corporation; or as conveying any rights or permission to manufacture, use, or sell any patented invention that may in any way be related thereto.

This report is releasable to the National Technical Information Service (NTIS). At NTIS, it will be available to the general public, including foreign nations.

This technical report has been reviewed and is approved for publication.

Scott M. Richardson
SCOTT M. RICHARDSON
Aerospace Engineer
Fan/Compressor Branch
Turbine Engine Division
Aero Propulsion & Power Directorate

Marvin A. Stibich
MARVIN A. STIBICH
Chief, Fan/Compressor Branch
Turbine Engine Division
Aero Propulsion & Power Directorate

FOR THE COMMANDER

Richard J. Hill
RICHARD J. HILL
Chief of Technology
Turbine Engine Division
Aero Propulsion & Power Directorate

If your address has changed, if you wish to be removed from our mailing list, or if the addressee is no longer employed by your organization please notify WL/POTF, WPAFB, OH 45433-7251 to help us maintain a current mailing list.

Copies of this report should not be returned unless return is required by security considerations, contractual obligations, or notice on a specific document.

REPORT DOCUMENTATION PAGE

Form Approved
OMB No. 0704-0188

Public reporting burden for this collection of information is estimated to average 1 hour per response, including the time for reviewing instructions, searching existing data sources, gathering and maintaining the data needed, and completing and reviewing the collection of information. Send comments regarding this burden estimate or any other aspect of this collection of information, including suggestions for reducing this burden, to Washington Headquarters Services, Directorate for Information Operations and Reports, 1215 Jefferson Davis Highway, Suite 1204, Arlington, VA 22202-4302, and to the Office of Management and Budget, Paperwork Reduction Project (0704-0188), Washington, DC 20503.

1. AGENCY USE ONLY (Leave blank)	2. REPORT DATE	3. REPORT TYPE AND DATES COVERED	
	DEC 1994	FINAL	06/01/92--12/01/94
4. TITLE AND SUBTITLE		5. FUNDING NUMBERS	
NUMERICAL UNSTEADY AERODYNAMIC SIMULATOR FOR BLADE FORCED RESPONSE PHENOMENA		C F33615-92-C-2212 PE 62203 PR 3066 TA 12 WU TF	
6. AUTHOR(S)		8. PERFORMING ORGANIZATION REPORT NUMBER	
T. C. AYER J. M. VERDON		R94-970312-4	
7. PERFORMING ORGANIZATION NAME(S) AND ADDRESS(ES)		9. SPONSORING / MONITORING AGENCY NAME(S) AND ADDRESS(ES)	
UNITED TECHNOLOGIES RESEARCH CENTER EAST HARTFORD CT 06108		AEROPROPULSION AND POWER DIRECTORATE WRIGHT LABORATORY AIR FORCE MATERIEL COMMAND WRIGHT-PATTERSON AFB OH 45433-7251	
10. SPONSORING / MONITORING AGENCY REPORT NUMBER			
WL-TR-95-2011			
11. SUPPLEMENTARY NOTES			
12a. DISTRIBUTION / AVAILABILITY STATEMENT		12b. DISTRIBUTION CODE	
APPROVED FOR PUBLIC RELEASE; DISTRIBUTION IS UNLIMITED.			
13. ABSTRACT (Maximum 200 words)			
<p>This report describes the application of a modern, time-accurate, Euler/Navier-Stokes analysis to the prediction of unsteady subsonic and transonic flows through a two-dimensional cascade. In particular, unsteady flows excited by harmonic, pure torsional and pure bending vibrations of the blades of the Tenth Standard Cascade. The purpose of this study is to validate the Euler/Navier-Stokes analysis along with an existing linearized inviscid analysis for unsteady flows that are representative of those associated with blade flutter in modern fans and compressors. The analysis is also applied to determine the relative importance of nonlinear and viscous effects in the unsteady response of a cascade to prescribed blade motions.</p> <p>The results of the study indicate a close agreement between inviscid and viscous blade loadings for unsteady subsonic flows. For unsteady transonic flows, shocks and their motions introduce significant nonlinear or second and higher harmonic contributions to the local unsteady response.</p>			
14. SUBJECT TERMS		15. NUMBER OF PAGES	
COMPUTATIONAL FLUID DYNAMICS, UNSTEADY FLOW, FORCED RESPONSE		72	
16. PRICE CODE			
17. SECURITY CLASSIFICATION OF REPORT	18. SECURITY CLASSIFICATION OF THIS PAGE	19. SECURITY CLASSIFICATION OF ABSTRACT	20. LIMITATION OF ABSTRACT
UNCLASSIFIED	UNCLASSIFIED	UNCLASSIFIED	UL

Numerical Unsteady Aerodynamic Simulator for Vibrating Blade Rows

Contents

Summary	1
1 Introduction	2
2 Physical Problem and Mathematical Description	4
2.1 Unsteady Flow through a Two-Dimensional Cascade	4
2.2 Fluid Dynamic Equations	5
3 Nonlinear Unsteady Aerodynamic Models	7
3.1 Viscous Flow — The Reynolds-Averaged Navier-Stokes Equations	7
3.2 High Reynolds Number Flow — The Thin-Layer Navier-Stokes Equations . .	8
3.3 Inviscid Flow — The Euler Equations	10
4 The NPHASE Analysis	12
4.1 Finite Volume Approximation	12
4.2 Flux Evaluations and Approximate Factorization	14
4.3 Viscous Terms	17
5 Unsteady Excitation and Aerodynamic Response	19
5.1 Blade Motion	19
5.2 Unsteady Aerodynamic Response at a Moving Blade Surface	19
6 Numerical Results	23
6.1 Computational Data, Steady Background Flows	23
6.2 Unsteady Subsonic Flows	25
6.3 Unsteady Transonic Flows	27
7 Concluding Remarks	31
8 References	33
Figures 1 through 29	36

Accession For	
NTIS	CRA&I <input checked="" type="checkbox"/>
DTIC	TAB <input type="checkbox"/>
Unannounced <input type="checkbox"/>	
Justification _____	
By _____	
Distribution / _____	
Availability Codes	
Dist	Avail and/or Special
A-1	

List of Figures

Figure	Page
1 Two-dimensional transonic compressor cascade; $M_{+\infty} < M_{-\infty} < 1$.	36
2 Unsteady excitations: blade motion, incident vortical and entropic disturbances from upstream, and incident acoustic disturbances from upstream and downstream.	37
3 Steady state, ———, and instantaneous, - - - -, blade, wake and shock positions.	38
4 H-mesh used for the NPHASE, steady and unsteady, inviscid, transonic simulations.	39
5 Composite H/C mesh used for the LINFL0 unsteady transonic calculations.	40
6 Predicted steady surface pressure (a) and skin friction (b) distributions for inviscid and viscous (at $Re = 10^6$) subsonic ($M_{-\infty} = 0.7$, $\Omega_{-\infty} = 55$ deg) flows through the 10th Standard Cascade.	41
7 Predicted steady surface pressure (a) and skin friction (b) distributions for inviscid and viscous (at $Re = 10^6$) transonic ($M_{-\infty} = 0.8$, $\Omega_{-\infty} = 58$ deg) flows through the 10th Standard Cascade.	42
8 Instantaneous surface pressure distributions for inviscid flows through the subsonic ($M_{-\infty} = 0.7$, $\Omega_{-\infty} = 55$ deg) 10th Standard Cascade undergoing prescribed blade vibrations: (a) in-phase torsional vibration about midchord at $ \alpha = 2$ deg, $\omega = 1$, and $\sigma = 0$ deg; (b) out-of-phase bending vibration at $ h_y = 0.01$, $\omega = 1$, $\sigma = 180$ deg.	43
9 Instantaneous surface pressure distributions for viscous flows at $Re = 10^6$ through the subsonic ($M_{-\infty} = 0.7$, $\Omega_{-\infty} = 55$ deg) 10th Standard Cascade undergoing prescribed blade vibrations: (a) in-phase torsional vibration about midchord at $ \alpha = 2$ deg, $\omega = 1$, and $\sigma = 0$ deg; (b) out-of-phase bending vibration at $ h_y = 0.01$, $\omega = 1$, $\sigma = 180$ deg.	44
10 Pressure-displacement function distributions for inviscid subsonic flow ($M_{-\infty} = 0.7$, $\Omega_{-\infty} = 55$ deg) through the 10th Standard Cascade undergoing an in-phase torsional vibration about midchord at $ \alpha = 2$ deg, $\omega = 1$, and $\sigma = 0$ deg: (a) NPHASE nonlinear prediction; (b) NPHASE first-harmonic.	45
11 Real components of the Fourier amplitudes of the unsteady surface pressure distribution for inviscid subsonic ($M_{-\infty} = 0.7$, $\Omega_{-\infty} = 55$ deg) flow through the 10th Standard Cascade undergoing an in-phase torsional vibration about midchord at $ \alpha = 2$ deg, $\omega = 1$, and $\sigma = 0$ deg: (a) Suction surface; (b) Pressure surface.	46

Figure	Page
12 Imaginary components of the Fourier amplitudes of the unsteady surface pressure distribution for inviscid subsonic ($M_{\infty} = 0.7$, $\Omega_{\infty} = 55$ deg) flow through the 10th Standard Cascade undergoing an in-phase torsional vibration about midchord at $ \alpha = 2$ deg, $\omega = 1$, and $\sigma = 0$ deg: (a) Suction surface; (b) Pressure surface.	47
13 Pressure-displacement function distribution for inviscid subsonic ($M_{\infty} = 0.7$, $\Omega_{\infty} = 55$ deg) flow through the 10th Standard Cascade undergoing an out-of-phase bending vibration at $ h_y = 0.01$, $\omega = 1$, and $\sigma = 180$ deg: (a) NPHASE nonlinear prediction; (b) NPHASE first-harmonic prediction.	48
14 Real components of the Fourier amplitudes of the unsteady surface pressure distribution for inviscid subsonic ($M_{\infty} = 0.7$, $\Omega_{\infty} = 55$ deg) flow through the 10th Standard Cascade undergoing an out-of-phase bending vibration at $ h_y = 0.01$, $\omega = 1$, and $\sigma = 180$ deg: (a) Suction surface; (b) Pressure surface.	49
15 Imaginary components of the Fourier amplitudes of the unsteady surface pressure distribution for inviscid subsonic ($M_{\infty} = 0.7$, $\Omega_{\infty} = 55$ deg) flow through the 10th Standard Cascade undergoing an out-of-phase bending vibration at $ h_y = 0.01$, $\omega = 1$, and $\sigma = 180$ deg: (a) Suction surface; (b) Pressure surface.	50
16 Work per cycle versus interblade phase angle for inviscid and viscous (at $Re = 10^6$) subsonic flows through the 10th Standard Cascade undergoing prescribed blade motions at unit frequency ($\omega = 1$): (a) torsional vibrations at $ \alpha = 2$ deg about midchord; (b) bending vibrations at $ h_y = 0.01$.	51
17 Instantaneous surface pressure distributions for inviscid flows through the transonic ($M_{\infty} = 0.8$, $\Omega_{\infty} = 58$ deg) 10th Standard Cascade undergoing prescribed blade vibrations: (a) in-phase torsional vibration about midchord at $ \alpha = 1$ deg, $\omega = 1$, and $\sigma = 0$ deg; (b) out-of-phase bending vibration at $ h_y = 0.01$, $\omega = 1$, $\sigma = 180$ deg.	52
18 Instantaneous surface pressure distributions for viscous flows (at $Re = 10^6$) through the transonic ($M_{\infty} = 0.8$, $\Omega_{\infty} = 58$ deg) 10th Standard Cascade undergoing prescribed blade vibrations: (a) in-phase torsional vibration about midchord at $ \alpha = 1$ deg, $\omega = 1$, and $\sigma = 0$ deg; (b) out-of-phase bending vibration at $ h_y = 0.01$, $\omega = 1$, $\sigma = 180$ deg.	53
19 Pressure-displacement function distribution for viscous (at $Re = 10^6$) and inviscid transonic flows ($M_{\infty} = 0.8$, $\Omega_{\infty} = 58$ deg) through the 10th Standard Cascade undergoing an in-phase torsional vibration about midchord at $ \alpha = 1$ deg, $\omega = 1$, and $\sigma = 0$ deg: (a) NPHASE nonlinear predictions; (b) NPHASE first-harmonic predictions.	54

Figure		Page
20	Real components of the Fourier amplitudes of the unsteady surface pressure distribution for viscid (at $Re = 10^6$) and inviscid transonic ($M_{\infty} = 0.8$, $\Omega_{\infty} = 58$ deg) flows through the 10th Standard Cascade undergoing an in-phase torsional vibration about midchord at $ \alpha = 1$ deg, $\omega = 1$, and $\sigma = 0$ deg: (a) Suction surface; (b) Pressure surface.	55
21	Imaginary components of the Fourier amplitudes of the unsteady surface pressure distribution for viscid (at $Re = 10^6$) and inviscid transonic ($M_{\infty} = 0.8$, $\Omega_{\infty} = 58$ deg) flows through the 10th Standard Cascade undergoing an in-phase torsional vibration about midchord at $ \alpha = 1$ deg, $\omega = 1$, and $\sigma = 0$ deg: (a) Suction surface; (b) Pressure surface.	56
22	Real components of the Fourier amplitudes of the unsteady surface pressure distribution for inviscid transonic ($M_{\infty} = 0.8$, $\Omega_{\infty} = 58$ deg) flow through the 10th Standard Cascade undergoing an in-phase torsional vibration about midchord at $ \alpha = 1$ deg, $\omega = 1$, and $\sigma = 0$ deg: (a) Suction surface; (b) Pressure surface.	57
23	Imaginary components of the Fourier amplitudes of the unsteady surface pressure distribution for inviscid transonic ($M_{\infty} = 0.8$, $\Omega_{\infty} = 58$ deg) flow through the 10th Standard Cascade undergoing an in-phase torsional vibration about midchord at $ \alpha = 1$ deg, $\omega = 1$, and $\sigma = 0$ deg: (a) Suction surface; (b) Pressure surface.	58
24	Pressure-displacement function distribution for viscid (at $Re = 10^6$) and inviscid transonic ($M_{\infty} = 0.8$, $\Omega_{\infty} = 58$ deg) flows through the 10th Standard Cascade undergoing an out-of-phase bending vibration at $ h_y = 0.01$, $\omega = 1$, and $\sigma = 180$ deg: (a) NPHASE nonlinear predictions; (b) NPHASE first-harmonic predictions.	59
25	Real components of the Fourier amplitudes of the unsteady surface pressure distribution for viscid (at $Re = 10^6$) and inviscid transonic ($M_{\infty} = 0.8$, $\Omega_{\infty} = 58$ deg) flows through the 10th Standard Cascade undergoing an out-of-phase bending vibration at $ h_y = 0.01$, $\omega = 1$, and $\sigma = 180$ deg: (a) Suction surface; (b) Pressure surface.	60
26	Imaginary components of the Fourier amplitudes of the unsteady surface pressure distribution for viscid (at $Re = 10^6$) and inviscid transonic ($M_{\infty} = 0.8$, $\Omega_{\infty} = 58$ deg) flows through the 10th Standard Cascade undergoing an out-of-phase bending vibration at $ h_y = 0.01$, $\omega = 1$, and $\sigma = 180$ deg: (a) Suction surface; (b) Pressure surface.	61
27	Real components of the Fourier amplitudes of the unsteady surface pressure distribution for inviscid transonic ($M_{\infty} = 0.8$, $\Omega_{\infty} = 58$ deg) flow through the 10th Standard Cascade undergoing an out-of-phase bending vibration at $ h_y = 0.01$, $\omega = 1$, and $\sigma = 180$ deg: (a) Suction surface; (b) Pressure surface.	62

Figure	Page
28 Imaginary components of the Fourier amplitudes of the unsteady surface pressure distribution for inviscid ($M_{\infty} = 0.8$, $\Omega_{\infty} = 58$ deg) flow through the 10th Standard Cascade undergoing an out-of-phase bending vibration at $ h_y = 0.01$, $\omega = 1$, and $\sigma = 180$ deg: (a) Suction surface; (b) Pressure surface.	63
29 Work per cycle versus interblade phase angle for inviscid and viscous (at $Re = 10^6$) transonic flows through the 10th Standard Cascade undergoing prescribed blade motions at unit frequency ($\omega = 1$): (a) torsional vibrations at $ \alpha = 1$ deg about midchord; (b) bending vibrations at $ h_y = 0.01$.	64

Numerical Unsteady Aerodynamic Simulator for Vibrating Blade Rows

Summary

In this report we describe the application of a modern, time-accurate, Euler/Navier-Stokes analysis, or numerical unsteady aerodynamic simulator, to the prediction of unsteady subsonic and transonic flows through a two-dimensional cascade. In particular, we consider unsteady flows excited by harmonic, pure torsional and pure bending vibrations of the blades of the Tenth Standard Cascade. One purpose of this study is to validate the Euler/Navier Stokes analysis along with an existing linearized inviscid analysis via result comparisons for unsteady flows that are representative of those associated with blade flutter in modern fans and compressors. We have also applied the nonlinear, time-accurate analysis to determine the relative importance of nonlinear and viscous effects on the unsteady response of a cascade to prescribed blade motions. It is anticipated that such applications will guide the further development of time-accurate, nonlinear analyses as well as the approximate, but very efficient, unsteady aerodynamic analyses that are used in turbomachinery aeroelastic and aeroacoustic design prediction systems.

The results of the present study reveal a close agreement between inviscid and viscous blade loadings for unsteady subsonic flows. Also, the unsteady surface pressure and local work per cycle responses in such flows are essentially linear, and they are predicted quite accurately using a linearized inviscid analysis. For unsteady transonic flows, shocks and their motions introduce significant nonlinear or second and higher harmonic contributions to the local unsteady response. Viscous displacement effects tend to diminish shock strength and the impulsive unsteady loads associated with shocks and their motions. The energy transfer between the fluid and structural motions in both subsonic and transonic flows is essentially captured by the first-harmonic component of the nonlinear inviscid and viscous solutions, but in transonic flows the nonlinear, first-harmonic and the linearized inviscid response predictions differ significantly in the vicinity of shocks and in the supersonic regions upstream of the shocks.

1. Introduction

A time-accurate Navier-Stokes analysis, or numerical simulator, is needed for understanding the relative importance of nonlinear and viscous effects on the unsteady flows associated with turbomachinery blade vibrations and blade-row noise generation. Once validated, such an analysis could also serve as a benchmark for evaluating and guiding the further development of the asymptotic unsteady aerodynamic models that are currently used in turbomachinery aeroelastic and aeroacoustic design prediction systems.

Until recently, the unsteady aerodynamic analyses that have been used in aeroelastic and aeroacoustic design studies were based on classical linearized, inviscid, flow theory (see [Whi87] for a review), which essentially applies to cascades of unloaded flat-plate blades that operate in entirely subsonic or entirely supersonic flow environments. Over the past decade, more general inviscid, unsteady, aerodynamic linearizations have been developed (e.g., see [Whi90, Ver92, HC93]). These account for the effects of important design features, such as real blade geometry, steady blade loading, and operation at transonic Mach numbers, on the unsteady aerodynamic response of blade rows. This type of model has received considerable attention in recent years, and numerical methods and computer codes for solving the resulting linearized equation sets are now being applied in turbomachinery aeroelastic design prediction systems [Smi90, MM93].

Although linearized inviscid analyses meet the needs of designers for efficient unsteady aerodynamic response predictions, of necessity, they ignore potentially important physical and geometrical properties of the flow, including the effects of moderate to large amplitude unsteady excitation and the effects of viscous-layer displacement and separation. Since the early 1980's, a number of time-accurate Euler and Navier-Stokes procedures have been developed to predict unsteady flows (see [Ver93] for a review). These have been applied to predict flows through single blade rows in which the unsteadiness is caused by prescribed blade vibrations ([HR89, He90, Sid91]) or by prescribed aerodynamic disturbances at the inflow or outflow boundaries [Gil88], and flows through aerodynamically coupled arrays in which the unsteadiness is caused by the relative motions of adjacent blade rows ([Rai87, Rai89]).

These recent and important advances in the numerical simulation of unsteady turbomachinery flows suggest that it is now appropriate to carefully validate and, if necessary, extend a time-accurate, Euler/Navier-Stokes procedure for the prediction of turbomachinery aeroelastic and aeroacoustic response phenomena. Usually, numerical procedures are verified via comparisons with experimental data (e.g., [MW92]), but because of the numerous controlling parameters and uncertainties involved, it is often difficult to ascertain causes for the differences between the numerical and experimental results. In the present effort, we are taking an alternative approach; one in which solutions based upon very different analytical procedures are compared, both to validate the procedures and to better understand the relevant unsteady flow phenomena.

A validated Navier-Stokes analysis for turbomachinery unsteady flows will represent an important advance in unsteady aerodynamic theory. This numerical simulator (or "wind tunnel") can provide engineers with useful insights on the nonlinear and viscous effects associated with blade vibration and discrete-tone noise generation. It can also provide a test-bed for assessing and improving the asymptotic, i.e., the linearized inviscid and high

Reynolds number, inviscid/viscid interaction, models that are currently being developed for use in turbomachinery aeroelastic and aeroacoustic design prediction systems.

For this purpose, in a previous investigation, an existing multi-blade-row Navier-Stokes analysis, i.e., the ROTOR2 analysis developed by Rai [Rai87, Rai89], was modified and applied to predict the unsteady flows through isolated, two-dimensional blade rows. In this work [DV94] unsteady subsonic flows excited by prescribed aerodynamic disturbances at inlet and exit that carry energy towards the blade row (the gust response problem) were considered. To evaluate this single blade row analysis, called NGUST, numerical simulations were performed for benchmark inviscid and viscous unsteady flows, and the predicted results were compared with those based on linearized inviscid flow theory. For small amplitude unsteady excitations, the unsteady pressure responses predicted with the nonlinear and linearized analyses showed very good agreement, both in the field and along the blade surfaces. Based upon a limited range of parametric studies, it was also observed that the unsteady responses to inlet vortical and acoustic excitations were linear over a surprisingly wide range of excitation amplitudes, but acoustic excitations from downstream produce responses with significant nonlinear content.

The objectives of the present GUIde program are to further develop a numerical simulator for inviscid and viscous unsteady flows through two-dimensional blade rows, and to gain insight into the relative importance of nonlinear and viscous effects on unsteady aerodynamic responses to prescribed blade motions (the flutter problem). In particular, time-accurate, Euler and Navier-Stokes solutions, based on the NPHASE analysis, see [SLH⁺94] for a detailed description, have been determined for subsonic and transonic unsteady cascade flows excited by prescribed pure torsional and pure bending vibrations of the blading. The NPHASE analysis which is based upon the high-resolution, wave-split, implicit, time marching, numerical scheme developed by Whitfield, Janus and Simpson [WJS88], is a multi-block, finite-volume analysis constructed by Huff, Swafford and Reddy [HSR91] for the time-accurate resolution of nonlinear, two-dimensional, unsteady flows through vibrating cascades.

In this report numerical results are presented for two-dimensional unsteady flows through a representative high-speed compressor cascade, i.e., the so-called Tenth Standard Cascade Configuration [FS83, FV93]. In particular, we consider unsteady subsonic and transonic flows driven by prescribed single-degree-of-freedom, torsional and bending vibrations of the blades. The Euler/Navier-Stokes results are compared with those obtained from the linearized inviscid flow analysis, LINFLOW [Ver92] to help validate and demonstrate Euler/Navier-Stokes capabilities for unsteady cascade flows.

2. Physical Problem and Mathematical Description

2.1 Unsteady Flow through a Two-Dimensional Cascade

We consider time-dependent flow, at high Reynolds number (Re) and with negligible body forces, of a perfect gas with constant specific heats through a two-dimensional cascade, such as the one shown in Figure 1. In general, the unsteady fluctuations in the flow can arise from one or more of the following sources: blade motions and aerodynamic disturbances at inlet and exit, that carry energy toward the blade row. In the absence of unsteady excitation, the flows far upstream and far downstream from the blade row are assumed to be at most a small steady perturbation from a uniform free stream. In this case any arbitrary unsteady aerodynamic motion of small amplitude can be represented approximately as the sum of independent entropic, vortical, and acoustic disturbances, as indicated in Figure 2. Inlet entropic and vortical excitations model the wakes from upstream blade rows; inlet and exit acoustic excitations, the potential flow variations associated with adjacent blade rows.

In the present discussion all physical variables are dimensionless. Lengths have been scaled with respect to blade chord, time with respect to the ratio of blade chord to upstream freestream flow speed, density viscosity, and thermal conductivity with respect to the upstream freestream values of these flow variables, velocity with respect to the upstream freestream flow speed, and stress, and therefore, pressure, with respect to the product of the upstream freestream density and the square of the upstream freestream speed. The scalings for the remaining variables can be determined from the equations given below, which have the same forms as their dimensional counterparts.

We will analyze the unsteady flow in a blade-row fixed coordinate frame in terms of the Cartesian spatial coordinates, e.g., (x, y) , where x and y measure distances along and normal to the reference blade chord, and the time t . To describe flows in which the fluid domain varies with time, it is useful to consider two sets of independent variables, say (\mathbf{x}, t) and $(\bar{\mathbf{x}}, t)$. The position vector $\mathbf{x}(\bar{\mathbf{x}}, t) = \bar{\mathbf{x}} + \mathcal{R}(\bar{\mathbf{x}}, t)$ describes the instantaneous location of a moving field or boundary point, say \mathcal{P} , $\bar{\mathbf{x}}$ refers to the reference or steady-state position of \mathcal{P} , and $\mathcal{R}(\bar{\mathbf{x}}, t)$ is the displacement of \mathcal{P} from its reference position. The displacement field, \mathcal{R} , is usually prescribed so that the solution domain moves with solid boundaries and is stationary far from the blade row.

The mean or steady-state positions of the blade chord lines coincide with the line segments $\bar{\eta} = \bar{\xi} \tan \Theta + mG$, $0 \leq \bar{\xi} \leq \cos \Theta$, $m = 0, \pm 1, \pm 2, \dots$, where $\bar{\xi}$ and $\bar{\eta}$ are Cartesian coordinates in the axial flow and cascade tangential directions, respectively, m is a blade number index, Θ is the cascade stagger angle, and $G = |\mathbf{G}|$, where \mathbf{G} is the cascade gap vector which is directed along the η -axis with magnitude equal to the blade spacing (see Figure 1). The blade motions (see Figure 3), are defined by $\mathbf{x}_{B_m} = \bar{\mathbf{x}}_{B_m} + \mathcal{R}_{B_m}(\bar{\mathbf{x}}_{B_m}, t)$, $m = 0, \pm 1, \pm 2, \dots$. Here, \mathcal{R}_{B_m} is a prescribed function of the position $\bar{\mathbf{x}}$, for $\bar{\mathbf{x}} \in B_m$, and the time t . It describes the displacement of a point on a moving blade surface, B_m , relative to its mean or steady-state position on B_m . In the present study we are interested primarily in unsteady flows excited by prescribed blade motions. However, entropic, $\tilde{s}_{-\infty}(\bar{\mathbf{x}}, t)$, vortical, $\tilde{\zeta}_{-\infty}(\bar{\mathbf{x}}, t)$, and acoustic, $\tilde{p}_{I, \mp\infty}(\bar{\mathbf{x}}, t)$, excitations, where the subscripts $-\infty$ and $+\infty$ refer to regions far upstream ($\bar{\xi} \leq \bar{\xi}_-$) and far downstream ($\bar{\xi} \geq \bar{\xi}_+$) from the blade row, respectively, can also

be prescribed as functions of $\bar{\mathbf{x}}$ and t . These functions must be solutions of the fluid dynamic field equations, which describe disturbances that carry energy toward the blade row.

2.2 Fluid Dynamic Equations

The equations that govern the flow are determined from the conservation laws for mass, momentum and energy, the constitutive relations for a Newtonian fluid, and the thermodynamic relations for a perfect gas. To describe unsteady flows, it is convenient to express the conservation laws relative to an arbitrary moving control volume $\mathcal{V}(t)$, which is bounded by the moving control surface $\mathcal{S}(\mathbf{x}, t)$, i.e.,

$$\frac{d}{dt} \int_{\mathcal{V}} \tilde{\rho} d\mathcal{V} + \int_{\mathcal{S}} \tilde{\rho} (\tilde{\mathbf{V}} - \dot{\mathcal{R}}) \cdot \mathbf{n} d\mathcal{S} = 0, \quad (2.1)$$

$$\frac{d}{dt} \int_{\mathcal{V}} \tilde{\rho} \tilde{\mathbf{V}} d\mathcal{V} + \int_{\mathcal{S}} \tilde{\rho} [\tilde{\mathbf{V}} \otimes (\tilde{\mathbf{V}} - \dot{\mathcal{R}})] \cdot \mathbf{n} d\mathcal{S} = \int_{\mathcal{S}} \tilde{\mathbf{T}} \cdot \mathbf{n} d\mathcal{S} \quad (2.2)$$

and

$$\frac{d}{dt} \int_{\mathcal{V}} \tilde{\rho} \tilde{E}_T d\mathcal{V} + \int_{\mathcal{S}} \tilde{\rho} \tilde{E}_T (\tilde{\mathbf{V}} - \dot{\mathcal{R}}) \cdot \mathbf{n} d\mathcal{S} = \int_{\mathcal{S}} \tilde{\mathbf{V}} \cdot \tilde{\mathbf{T}} \cdot \mathbf{n} d\mathcal{S} - \int_{\mathcal{S}} \tilde{\mathbf{Q}} \cdot \mathbf{n} d\mathcal{S}. \quad (2.3)$$

Here $\tilde{\rho}$, $\tilde{\mathbf{V}}$ and $\tilde{E}_T = \tilde{E} + \tilde{V}^2/2$ are the fluid density, velocity and specific total internal energy, respectively, $\dot{\mathcal{R}}$ is the velocity of a point on the control surface, $\tilde{\mathbf{T}}$ is the stress tensor, $\tilde{\mathbf{Q}}$ is the heat flux vector, \mathbf{n} is a unit outward normal vector, and \otimes denotes the tensor or dyadic product of two vectors.

For a Newtonian fluid having zero coefficient of bulk viscosity, the stress tensor (dyadic) is related to the fluid (thermostatic) pressure, \tilde{P} , and velocity, $\tilde{\mathbf{V}}$, by

$$\tilde{\mathbf{T}} = -\tilde{P}\mathbf{I} + \tilde{\mathbf{H}} = \tilde{P}\mathbf{I} - \tilde{\mu} Re^{-1}[(2\nabla \cdot \tilde{\mathbf{V}}/3)\mathbf{I} - \nabla \otimes \tilde{\mathbf{V}} - (\nabla \otimes \tilde{\mathbf{V}})_c], \quad (2.4)$$

where \mathbf{I} is the unit tensor; $\tilde{\mathbf{H}}$ is the viscous stress tensor; $\tilde{\mu}$ is the coefficient of shear viscosity; $Re = \bar{\rho}^* V^* L^* / \bar{\mu}^*$ is the flow Reynolds number; the superscript $*$ refers to a dimensional reference value of a flow variable; and the subscript c denotes the conjugate dyadic. The heat flux $\tilde{\mathbf{Q}}$ is related to the gradient of the temperature \tilde{T} or specific enthalpy, $\tilde{H} = \tilde{T}$, via Fourier's law, i.e.,

$$\tilde{\mathbf{Q}} = -\tilde{k} Pr^{-1} Re^{-1} \nabla \tilde{T}, \quad (2.5)$$

where \tilde{k} is the coefficient of thermal conductivity, $Pr = \bar{\mu}^* C_p^* / \bar{k}^*$ is the Prandtl number of the flow, and C_p^* is the (dimensional) specific heat of the fluid at constant pressure. Note that because of the nondimensionalization used in the present study, the temperature and specific enthalpy have identical numerical values.

The coefficients $\tilde{\mu}$ and \tilde{k} are assumed to be known functions of the temperature \tilde{T} . For example, the following empirical laws relating the molecular viscosity and the thermal conductivity to the temperature, e.g.,

$$\tilde{\mu} = \tilde{k} = \left(\frac{\tilde{T}}{T_{-\infty}} \right)^{3/2} \frac{T_{-\infty} + T_C}{\tilde{T} + T_C}, \quad (2.6)$$

are often used in Navier-Stokes calculations. Equations (2.6) are a form of Sutherland's Law. Here $T_{-\infty} = C_P^* T_{-\infty}^* / (V_{-\infty}^*)^2$ is the nondimensional reference temperature, and T_C is a constant, which for air has a dimensional value, T_C^* , of 110°K [Sch60].

In addition to the foregoing equations, two relations from classical thermodynamics are required; in particular, the equation of state for a thermally perfect gas and the equation relating the internal energy and the temperature or specific enthalpy for a calorically perfect gas, i.e.,

$$\tilde{P} = \gamma^{-1}(\gamma - 1)\tilde{\rho}\tilde{T} \quad \text{and} \quad \tilde{E} = \gamma^{-1}\tilde{T} = (\gamma - 1)^{-1}\tilde{P}/\tilde{\rho}, \quad (2.7)$$

respectively. Here, γ is the specific heat ratio of the fluid (constant pressure to constant volume).

The foregoing equations provide a sufficient set for determining the unknown fluid-dynamic variables. For turbulent flows, these equations describe the behavior of the ensemble- or Reynolds-averaged values of the time-dependent flow variables. The effects of random turbulent fluctuations are accommodated by incorporating the turbulent correlations, $\tilde{\rho}\tilde{\mathbf{v}}' \otimes \tilde{\mathbf{v}}'$ and $\tilde{\rho}\tilde{h}'_T \tilde{\mathbf{v}}'$, into the definition of the viscous stress tensor $\tilde{\boldsymbol{\Pi}}$ and the heat flux vector $\tilde{\mathbf{Q}}$, respectively. To obtain closure of the mean flow equations, the turbulent correlations are usually related to gradients in the ensemble-averaged or mean-flow variables via algebraic eddy viscosity models.

For convenience in developing numerical algorithms the conservation equations are usually written in column vector form as

$$\frac{d}{dt} \int_V \tilde{\mathbf{U}} dV + \int_S [\tilde{\mathbf{F}}_j + \tilde{\mathbf{G}}_j - \tilde{\mathbf{U}} \dot{\mathcal{R}}_{x_j}] n_{x_j} dS = 0. \quad (2.8)$$

Here the state vector $\tilde{\mathbf{U}}$, and the flux vectors $\tilde{\mathbf{F}}_j$ and $\tilde{\mathbf{G}}_j$, $j = 1, 2$, are defined by

$$\tilde{\mathbf{U}} = \begin{bmatrix} \tilde{\rho} \\ \tilde{\rho}\tilde{V}_{x_1} \\ \tilde{\rho}\tilde{V}_{x_2} \\ \tilde{\rho}\tilde{E}_T \end{bmatrix}, \quad \tilde{\mathbf{F}}_j = \begin{bmatrix} \tilde{\rho}\tilde{V}_{x_j} \\ \tilde{\rho}\tilde{V}_{x_1}\tilde{V}_{x_j} + \tilde{P}\delta_{1j} \\ \tilde{\rho}\tilde{V}_{x_2}\tilde{V}_{x_j} + \tilde{P}\delta_{2j} \\ \tilde{\rho}(\tilde{E}_T + \tilde{P}/\tilde{\rho})\tilde{V}_{x_j} \end{bmatrix}, \quad \tilde{\mathbf{G}}_j = \begin{bmatrix} 0 \\ -\tilde{\Pi}_{x_1x_j} \\ -\tilde{\Pi}_{x_2x_j} \\ -\tilde{\Pi}_{x_jx_i}\tilde{V}_{x_i} + \tilde{Q}_{x_j} \end{bmatrix}. \quad (2.9)$$

3. Nonlinear Unsteady Aerodynamic Models

3.1 Viscous Flow — The Reynolds-Averaged Navier-Stokes Equations

Equations that describe the fluid motion at the instantaneous position, $\mathbf{x} = \bar{\mathbf{x}} + \mathcal{R}(\bar{\mathbf{x}}, t)$, of a moving field point are obtained from the integral conservation laws (2.8) by applying Reynolds' transport theorem to interchange the order of time-differentiation and volume integration, Green's theorem to convert surface integrals to volume integrals, and taking the limit of the resulting volume integrals as $\mathcal{V}(t) \rightarrow 0$. After performing the necessary algebra, we find that

$$\frac{\partial \tilde{\mathbf{U}}}{\partial t} \bigg|_{\mathbf{x}} + \frac{\partial}{\partial x_j} (\tilde{\mathbf{F}}_j + \tilde{\mathbf{G}}_j) = 0 , \quad (3.1)$$

where the column vectors $\tilde{\mathbf{U}}$, $\tilde{\mathbf{F}}_j$ and $\tilde{\mathbf{G}}_j$ are defined in (2.9), and a summation over repeated indices is implied.

For application to turbomachinery unsteady flows the field equations (3.1) must be supplemented by near-field conditions at the vibrating blade surfaces and far-field conditions at the cascade inflow and outflow boundaries. Since transient unsteady aerodynamic behavior is usually not considered, a precise knowledge of the initial state of the fluid is not required. The no-slip condition, i.e., $\tilde{\mathbf{V}} = \dot{\mathcal{R}}_{\mathcal{B}_m}$ for $\mathbf{x} \in \mathcal{B}_m$, where $\mathcal{R}_{\mathcal{B}_m}$ is prescribed, applies at blade surfaces. In addition, either the heat flux $\tilde{\mathbf{Q}} \cdot \mathbf{n}$ or the temperature \tilde{T} must be prescribed at such surfaces. The entropy and vorticity (total temperature and total pressure) fluctuations at inlet, and the incident pressure fluctuations at inlet and exit must also be specified. The total pressure and total temperature fluctuations at exit and the unsteady pressure response at inlet and exit must be determined as part of the time-dependent solution.

Computational Coordinates

To enhance the efficiency and accuracy of a numerical solution scheme and to simplify the implementation of boundary conditions, a transformation of the governing equations from physical to computational space is usually performed. In computational space, the solution domain is a rectangular shape, and the computational grid is defined to be uniform, orthogonal and stationary for convenience in defining finite difference approximations.

Thus, we consider an independent variable transformation $(\mathbf{x}, t) \rightarrow (\boldsymbol{\alpha}, \tau)$ from physical Cartesian coordinates $\mathbf{x} = (x_1, x_2)$ and time t to a computational space described by the spatial coordinates $\boldsymbol{\alpha} = (\alpha_1, \alpha_2)$ and the time τ . After performing the necessary algebra, we find that the Navier-Stokes equations (3.1) can be written in strong conservation form as

$$\frac{\partial \tilde{\mathbf{U}}}{\partial \tau} \bigg|_{\boldsymbol{\alpha}} + \frac{\partial}{\partial \alpha_j} (\tilde{\mathbf{F}}_j + \tilde{\mathbf{G}}_j) = 0 , \quad (3.2)$$

where

$$\tilde{\mathbf{U}} = (J^{x\alpha})^{-1} \tilde{\mathbf{U}} , \quad \tilde{\mathbf{F}}_j = (J^{x\alpha})^{-1} \left(\frac{\partial \alpha_j}{\partial t} \tilde{\mathbf{U}} + \frac{\partial \alpha_j}{\partial x_k} \tilde{\mathbf{F}}_k \right) , \quad \text{and} \quad \tilde{\mathbf{G}}_j = (J^{x\alpha})^{-1} \left(\frac{\partial \alpha_j}{\partial x_k} \tilde{\mathbf{G}}_k \right) . \quad (3.3)$$

The viscous shear stresses [cf. (2.4)] and the heat fluxes [cf. (2.5) in the transformed computational space are given by

$$\tilde{\Pi}_{x_i x_j} = \tilde{\mu} Re^{-1} \left[\frac{\partial \alpha_k}{\partial x_j} \frac{\partial \tilde{V}_{x_i}}{\partial \alpha_k} + \frac{\partial \alpha_k}{\partial x_i} \frac{\partial \tilde{V}_{x_j}}{\partial \alpha_k} - 2 \frac{\partial \alpha_m}{\partial x_k} \frac{\partial \tilde{V}_{x_k}}{\partial \alpha_m} \delta_{ij}/3 \right] \quad (3.4)$$

and

$$\tilde{Q}_{x_i} = -\tilde{k} Pr^{-1} Re^{-1} \frac{\partial \alpha_j}{\partial x_i} \frac{\partial \tilde{H}}{\partial \alpha_j}. \quad (3.5)$$

Values of the metrics $J^{x\alpha}$, $\partial \alpha_j / \partial t$ and $\partial \alpha_j / \partial x_k$ must also be provided. In most cases these can be computed numerically using finite-difference approximations for the derivatives $\partial x_k / \partial \alpha_j$, etc. If the metrics appearing in Equation (3.3) can be expressed in terms of these derivatives, the numerical computation of the metrics is completed. In particular, for two-dimensional flows we find that

$$\begin{aligned} \frac{\partial \alpha_1}{\partial x_1} &= J^{x\alpha} \frac{\partial x_2}{\partial \alpha_2}, & \frac{\partial \alpha_2}{\partial x_1} &= -J^{x\alpha} \frac{\partial x_2}{\partial \alpha_1}, & \frac{\partial \alpha_1}{\partial x_2} &= -J^{x\alpha} \frac{\partial x_1}{\partial \alpha_2}, & \frac{\partial \alpha_2}{\partial x_2} &= J^{x\alpha} \frac{\partial x_1}{\partial \alpha_1}, \\ \frac{\partial \alpha_1}{\partial t} &= J^{x\alpha} \left[\frac{\partial x_1}{\partial \alpha_2} \frac{\partial x_2}{\partial \tau} - \frac{\partial x_1}{\partial \tau} \frac{\partial x_2}{\partial \alpha_2} \right], & \frac{\partial \alpha_2}{\partial t} &= -J^{x\alpha} \left[\frac{\partial x_1}{\partial \alpha_1} \frac{\partial x_2}{\partial \tau} - \frac{\partial x_1}{\partial \tau} \frac{\partial x_2}{\partial \alpha_1} \right] \end{aligned} \quad (3.6)$$

and

$$J^{x\alpha} = 1 / \left(\frac{\partial x_1}{\partial \alpha_1} \frac{\partial x_2}{\partial \alpha_2} - \frac{\partial x_1}{\partial \alpha_2} \frac{\partial x_2}{\partial \alpha_1} \right)$$

where the $J^{x\alpha}$ is the Jacobian of the transformation $(x, t) \rightarrow (\alpha, \tau)$, and is referred to as a metric Jacobian. For a numerical formulation based on the integral form of the governing equations the forward metrics are obtained from the geometry of computational cell in physical space. In particular, the cell volume and face areas are computed from the location of the grid points that define the vertices of the cell in physical space.

3.2 High Reynolds Number Flow — The Thin-Layer Navier-Stokes Equations

The Navier-Stokes equations must be considered if viscous effects are expected to be important throughout the fluid domain. However, for many flows of practical interest, the Reynolds number (Re) is usually sufficiently high so that the latter are concentrated in relatively thin layers across which the flow properties vary rapidly but continuously. Provided that large scale flow separations do not occur, these layers generally lie adjacent to the blade surfaces (boundary layers), downstream of the blades (wakes) and in the vicinity of rapid compressions (shocks). If viscous effects are negligible, i.e., if $Re \rightarrow \infty$, it is sufficient to consider only the outer or inviscid flow.

We proceed to consider high Reynolds number flow in which viscous effects are concentrated in thin layers lying adjacent to the blade surfaces and extending downstream from the blade trailing edges. We identify shear layer surfaces \mathcal{S}_m each of which is entirely contained within a viscous layer, and postulate that, within a viscous layer, flow gradients in the direction normal (n) to a shear layer surface will be substantially greater than those in the tangential direction. We can take advantage of this feature to simplify the viscous terms

that appear in the full Reynolds-averaged Navier-Stokes equations. In particular, we neglect the streamwise gradients of the viscous stresses and the heat fluxes, and retain the normal gradients. The resulting equations are known as the thin-layer Navier-Stokes equations.

The thin-layer equations can be determined from the transformed matrix form, i.e., (3.2), of the Reynolds-averaged Navier-Stokes equations. First, we assume that gradients of the viscous flux terms parallel to a body surface (i.e., in the α_1 -direction) are small compared to gradients normal (i.e., in the α_2 -direction) to the surface, and hence that the former can be neglected. Accordingly, we set

$$\frac{\partial \tilde{\mathbf{G}}_1}{\partial \alpha_1} \approx 0 \quad (3.7)$$

In addition, we assume that velocity and temperature or specific enthalpy gradients parallel to a body surface are small compared to velocity and temperature gradients in the normal direction. In this case the Cartesian components of the viscous stress tensor $\tilde{\Pi}$ and the heat flux vector $\tilde{\mathbf{Q}}$ are given approximately by

$$\tilde{\Pi}_{x_i x_j} \approx \tilde{\mu} Re^{-1} \left[\frac{\partial \alpha_2}{\partial x_j} \frac{\partial \tilde{V}_{x_i}}{\partial \alpha_2} + \frac{\partial \alpha_2}{\partial x_i} \frac{\partial \tilde{V}_{x_j}}{\partial \alpha_2} - 2 \frac{\partial \alpha_2}{\partial x_k} \frac{\partial \tilde{V}_{x_k}}{\partial \alpha_2} \delta_{ij}/3 \right] \quad (3.8)$$

and

$$\tilde{Q}_{x_i} \approx -\tilde{k} Pr^{-1} Re^{-1} \frac{\partial \alpha_2}{\partial x_i} \frac{\partial \tilde{H}}{\partial \alpha_2}, \quad (3.9)$$

respectively. Thus, the viscous flux vector, $\tilde{\mathbf{G}}_2$, has the form [cf. (2.9) and (3.3)]

$$\tilde{\mathbf{G}}_2 = -(J^{x\alpha})^{-1} \begin{bmatrix} 0 \\ \frac{\partial \alpha_2}{\partial x_k} \tilde{\Pi}_{x_1 x_k} \\ \frac{\partial \alpha_2}{\partial x_k} \tilde{\Pi}_{x_2 x_k} \\ \frac{\partial \alpha_2}{\partial x_k} [\tilde{\Pi}_{x_k x_j} \tilde{V}_j - \tilde{Q}_k] \end{bmatrix} = (J^{x\alpha})^{-1} \frac{\partial \alpha_2}{\partial x_k} \tilde{\mathbf{G}}_k, \quad (3.10)$$

and it can be approximated by

$$\tilde{\mathbf{G}}_2 \approx \tilde{\tilde{\mathbf{G}}}^{TL} = -(J^{x\alpha})^{-1} Re^{-1} \begin{bmatrix} 0 \\ \tilde{\tilde{\mu}} \left(K_1 \frac{\partial \tilde{V}_{x_1}}{\partial \alpha_2} + K_2 \frac{\partial \alpha_2}{\partial x_1} \right) \\ \tilde{\tilde{\mu}} \left(K_1 \frac{\partial \tilde{V}_{x_2}}{\partial \alpha_2} + K_2 \frac{\partial \alpha_2}{\partial x_2} \right) \\ K_1 \left[\tilde{\tilde{\mu}} \frac{\partial (\tilde{V}^2/2)}{\partial \alpha_2} + \tilde{k} Pr^{-1} \frac{\partial \tilde{H}}{\partial \alpha_2} \right] + K_2 K_3 \end{bmatrix}, \quad (3.11)$$

where

$$\begin{aligned} K_1 &= \left(\frac{\partial \alpha_2}{\partial x_1} \right)^2 + \left(\frac{\partial \alpha_2}{\partial x_2} \right)^2 \\ K_2 &= (1/3) \left(\frac{\partial \alpha_2}{\partial x_1} \frac{\partial \tilde{V}_{x_1}}{\partial \alpha_2} + \frac{\partial \alpha_2}{\partial x_2} \frac{\partial \tilde{V}_{x_2}}{\partial \alpha_2} \right) \end{aligned} \quad (3.12)$$

and

$$K_3 = \tilde{V}_{x_1} \frac{\partial \alpha_2}{\partial x_1} + \tilde{V}_{x_2} \frac{\partial \alpha_2}{\partial x_2}$$

The field equations resulting from the approximations (3.7) and (3.11); i.e., the thin-layer, Reynolds-averaged, Navier-Stokes equations, then have the form

$$\frac{\partial \tilde{\mathbf{U}}}{\partial \tau} \bigg|_{\alpha} + \frac{\partial}{\partial \alpha_j} \tilde{\mathbf{F}}_j + \frac{\partial}{\partial \alpha_2} \tilde{\mathbf{G}}^{TL} = 0. \quad (3.13)$$

The assumptions introduced to arrive at equation (3.13) lead to a substantial reduction in the computer storage and time requirements needed to determine viscous solutions.

An eddy viscosity formulation can be used in conjunction with (3.11) to model turbulent phenomena. Thus, an effective viscosity, $\tilde{\mu}_{\text{eff}}$, and an effective thermal conductivity, \tilde{k}_{eff} , i.e.,

$$\tilde{\mu}_{\text{eff}} = \tilde{\mu} + \tilde{\epsilon} \quad \text{and} \quad \tilde{k}_{\text{eff}} = \tilde{k} + (P_r) \tilde{\epsilon}_H = \tilde{\mu} + (Pr/Pr_T) \tilde{\epsilon}, \quad (3.14)$$

are used in lieu of $\tilde{\mu}$ and \tilde{k} in equation (3.11). Here $\tilde{\epsilon}$ and $\tilde{\epsilon}_H = \tilde{\epsilon}/Pr_T$ are the turbulent eddy viscosity and eddy diffusivity, respectively, and Pr_T is the turbulent Prandtl number. The eddy viscosity, $\tilde{\epsilon}$, and hence, the diffusivity ϵ_H , can be determined using an algebraic turbulence model, e.g., the two-layer, Cebeci-Smith [CS74] or Baldwin-Lomax [BL78] model.

3.3 Inviscid Flow — The Euler Equations

In the inviscid limit ($Re \rightarrow \infty$) the thicknesses of the viscous layers become zero, and they can be modeled as surfaces across which the flow variables are discontinuous. In particular, boundary layers and wakes become vortex sheets that support a discontinuity in tangential velocity, and shocks become surfaces that support a discontinuity in normal velocity. It is usually assumed that the boundary layers remain attached to the blade surfaces and support jumps in velocity from zero at the “walls” to inviscid values at their “edges.” Furthermore, the vortex-sheet unsteady wakes emanate from the blade trailing edges and extend infinitely far downstream. The integral forms of the conservation laws are required to describe the flow over the entire domain of interest. These provide differential equations in regions where the flow variables are continuously differentiable and “jump” conditions at the surfaces across which the flow variables are discontinuous.

The field equations that govern continuous, inviscid, fluid motion (i.e., the Euler equations) are obtained from equations (2.1)–(2.3) by setting $\tilde{\mathbf{T}} = -\tilde{P}\mathbf{I}$ and $\tilde{\mathbf{Q}} = 0$, or from equations (3.2) and (3.13) by setting $\tilde{\mathbf{G}}$ and $\tilde{\mathbf{G}}^{TL} = 0$, respectively. In principle, the inviscid field equations must be supplemented by jump conditions that apply across moving

boundary layers, \mathcal{B}_m , wakes, \mathcal{W}_m , and shocks, $\mathcal{S}h_m$. However, the usual practice in numerical computations is to solve the field equations over the entire fluid domain, thereby “capturing” wake and shock phenomena. The inviscid flow is then determined subject to flow tangency conditions, i.e.,

$$(\tilde{\mathbf{V}} - \dot{\mathcal{R}}_{\mathcal{B}_m}) \cdot \mathbf{n} = 0 \quad \text{for } \mathbf{x} \in \mathcal{B}_m . \quad (3.15)$$

at the moving blade surfaces, and far-field conditions at the inflow and outflow boundaries of the computational domain. The far-field conditions used in the inviscid approximation are the same as those indicated previously for Navier-Stokes simulations.

4. The NPHASE Analysis

A numerical model, based on Roe's [Roe81] approximate Riemann solver, for solving nonlinear unsteady flow problems was developed by Whitfield, Janus and Simpson [WJS88]. This model was subsequently extended for turbomachinery applications and implemented into an unsteady flow code, called NPHASE, by Huff, Swafford and Reddy [HSR91]. NPHASE is an implicit, multi-block, cell-centered, finite-volume code, that can be used for predicting two-dimensional, nonlinear, viscous (at high Reynolds number) and inviscid unsteady flows through vibrating cascades. A detailed description of the current version, i.e. version 2.0, of the NPHASE analysis can be found in [SLH⁺94] and the references cited therein.

The computational mesh used in NPHASE is a sheared H-mesh, typically generated using the IGB grid generation package of [BH92]. This structured mesh defines a curvilinear coordinate system, in which coordinate curves lie along the boundaries of the physical domain. A time-dependent coordinate transformation, $(\mathbf{x}, t) \rightarrow (\boldsymbol{\alpha}, \tau)$, from the physical domain, in which the grid deforms with the blade motion, to a computational domain, in which the grid is stationary, uniform, and orthogonal, is applied to simplify the implementation of numerical differencing and flow boundary conditions. Recall that $\mathbf{x} = \bar{\mathbf{x}} + \mathcal{R}(\bar{\mathbf{x}}, t)$, where \mathcal{R} defines the displacement of the moving field points from their reference or mean positions.

The time-dependent displacement field, $\mathcal{R}(\bar{\mathbf{x}}, t)$, is prescribed in a manner that facilitates implementation of the flow boundary conditions. It is determined here as a solution of Laplace's equation, $\nabla_{\bar{\mathbf{x}}}^2 \mathcal{R} = 0$; subject to Dirichlet boundary conditions at the blade surfaces, i.e., $\mathcal{R} = \mathcal{R}_{B_m}$ for $\bar{\mathbf{x}} \in B_m$, and in the far field, $\mathcal{R} = 0$ for $\xi \lesssim \xi_{\mp}$; and, for the blade motions considered herein [cf. (5.1)–(5.3)], phase-lagged, blade-to-blade, periodicity conditions; i.e., $\mathcal{R}(\bar{\mathbf{x}} + m\mathbf{G}, t - m\sigma/\omega) = \mathcal{R}(\bar{\mathbf{x}}, t)$, upstream and downstream of the blade row.

4.1 Finite Volume Approximation

For a finite volume discretization, based on the integral forms of the governing field equations, the time-dependent geometric properties of the mesh cells in physical space are required. These include the cell volume, ϑ , the volume swept out per unit time by the constant α_j face as the cell interface moves, $\dot{\vartheta}_j$, and the area of the constant α_j face projected in the x_k direction, A_{jk} . These geometric properties of a cell are determined from the instantaneous locations of the cell vertices in physical space.

We can write the finite volume spatial discretization of equation (3.13) as

$$\left. \frac{\partial \tilde{\mathbf{U}}}{\partial \tau} \right|_{\boldsymbol{\alpha}} = -\delta_j \tilde{\mathbf{F}}_j - \delta_2 \tilde{\mathbf{G}}^{TL} = -\tilde{\mathbf{R}} \quad (4.1)$$

where

$$\tilde{\mathbf{U}} = \vartheta \tilde{\mathbf{U}} , \quad \tilde{\mathbf{F}}_j = -\dot{\vartheta}_j \tilde{\mathbf{U}} + A_{jk} \tilde{\mathbf{F}}_k , \quad \text{and} \quad \tilde{\mathbf{G}}^{TL} = (J^{x\alpha})^{-1} A_{2k} \tilde{\mathbf{G}}_k . \quad (4.2)$$

Here, the vector $\tilde{\mathbf{U}}$ represents an average over the cell volume; the vector $\tilde{\mathbf{F}}_j$ is the inviscid flux across a constant α_j cell face; $\tilde{\mathbf{G}}^{TL}$ is the viscous flux across a constant α_2 cell face; the symbol δ_j denotes the difference across adjacent cell interfaces, i.e. $\delta_j(\) = (\)_{j+1/2} - (\)_{j-1/2}$;

and $\tilde{\mathbf{R}}$ is referred to as the residual. The repeated j index in (4.1) implies summation over all computational coordinate directions, so that the term $\delta_j \tilde{\mathbf{F}}_j$ is the net inviscid flux through the cell. The grid deforms in physical space as the blades move. Therefore, the cell geometry terms, ϑ , $\dot{\vartheta}_j$ and A_{jk} , are time dependent. A comparison of equations (3.3) and (4.2) indicates that these geometric terms can be interpreted in terms of the metrics of the $(x, t) \rightarrow (\alpha, \tau)$ coordinate transformation. In particular, $\vartheta = (J^{x\alpha})^{-1}$, $\dot{\vartheta} = (J^{x\alpha})^{-1} \partial \alpha_j / \partial t$ and $A_{jk} = (J^{x\alpha})^{-1} \partial \alpha_j / \partial x_k$.

In the NPHASE analysis, the fluxes at the cell interfaces are computed from the values of the state vector on either side of the interface using the approximate one-dimensional Riemann solver developed by Roe [Roe81]. The interfacial flux is computed by multiplying the difference in the state vector across the interface by a flux Jacobian matrix representing the local interface conditions. The eigenvalues of this flux Jacobian matrix are used to determine which characteristic modes are included, thus controlling the direction of spatial differencing. This technique is known as flux difference splitting and results in a first-order accurate spatial differencing scheme. Higher order accuracy is obtained by using a corrective flux, which is limited by a TVD scheme to control dispersive errors.

The NPHASE time differencing is based on a second-order, implicit, three-point, backward, difference approximation of the time derivative. Thus, if the superscript n refers to the current or n th time level, we can write

$$\frac{3\Delta \tilde{\mathbf{U}}^n - \Delta \tilde{\mathbf{U}}^{n-1}}{2\Delta\tau} = -\tilde{\mathbf{R}}^{n+1}, \quad (4.3)$$

where $\Delta \tilde{\mathbf{U}}^n = \tilde{\mathbf{U}}^{n+1} - \tilde{\mathbf{U}}^n$, and the differences on the left-hand side involve both the state vector and the cell volume. Separating the time dependence of the state vector and the cell volume results in

$$\tilde{\Theta} \Delta \tilde{\mathbf{U}}^n + \tilde{\mathbf{R}}^{n+1} = \vartheta^{n-1} \Delta \tilde{\mathbf{U}}^{n-1} / 2\Delta\tau - \tilde{\mathbf{U}}^n (3\vartheta^{n+1} - 4\vartheta^n + \vartheta^{n-1}) / 2\Delta\tau = \mathcal{G}^{n+1}, \quad (4.4)$$

where $\tilde{\Theta} = 3\vartheta^{n+1} / 2\Delta\tau$.

The nonlinear equation (4.4) is solved at each time step using a Newton iteration procedure in which the iteration formula is given by

$$\left(\tilde{\Theta} \mathbf{I} + \frac{\partial \tilde{\mathbf{R}}}{\partial \tilde{\mathbf{U}}} \bigg|_{\tilde{\mathbf{U}}^{p-1}} \right) \Delta \tilde{\mathbf{U}}^p = \tilde{\Theta} (\tilde{\mathbf{U}}^{p-1} - \tilde{\mathbf{U}}^n) - \tilde{\mathbf{R}}^{p-1} + \mathcal{G}^{n+1}. \quad (4.5)$$

Here $p = 1, 2, \dots$ is the Newton iteration index, $\tilde{\mathbf{U}}^0 = \tilde{\mathbf{U}}^n$, $\Delta \tilde{\mathbf{U}}^p = \tilde{\mathbf{U}}^p - \tilde{\mathbf{U}}^{p-1}$, $\tilde{\mathbf{U}}^p$ is the Newton update to the state vector, and

$$\frac{\partial \tilde{\mathbf{R}}}{\partial \tilde{\mathbf{U}}} \bigg|_{\tilde{\mathbf{U}}^{p-1}} \Delta \tilde{\mathbf{U}}^p = \delta_j \left(\frac{\partial \tilde{\mathbf{F}}_j}{\partial \tilde{\mathbf{U}}} \bigg|_{\tilde{\mathbf{U}}^{p-1}} \Delta \tilde{\mathbf{U}}^p \right). \quad (4.6)$$

Once the Newton iteration converges $\Delta \tilde{\mathbf{U}}^p \equiv 0$, $\tilde{\mathbf{U}}^p \equiv \tilde{\mathbf{U}}^{n+1}$ and (4.4) is satisfied. Note that in the current version of NPHASE [SLH⁹⁴] the viscous flux term is included in the right-hand side residual $\tilde{\mathbf{R}}^{p-1}$ of equation (4.5), but ignored in constructing the left-hand

side, implicit, operator $\partial \tilde{\mathbf{R}} / \partial \tilde{\mathbf{U}} \Big|_{\tilde{\mathbf{U}}_{p-1}}$. This approach introduces errors into the left-hand side operator, but these become negligible as the Newton iterations converge.

The inviscid flux terms on the right-hand side of (4.5) are evaluated using flux difference splitting corrected for higher order spatial accuracy. Those on the left-hand side [cf. (4.6)] are evaluated using flux vector splitting for convenience in defining the approximate factorization, used to facilitate the solution. The coupling between adjacent cells introduced by the flux terms on the left-hand side of (4.5) makes it expensive to solve this equation. So the flux evaluation is approximately factored into the product of positive and negative operators. To reduce the error introduced by this approximate factorization, symmetric, Gauss-Seidel, subiterations [WT91] are used as part of the time stepping procedure. The subiteration procedure employs an *LU* decomposition of the Newton iteration matrix, with forward and backward substitution.

The field equation (4.1) must be solved subject to the appropriate surface conditions at the blade boundaries, and far-field conditions at the inflow and outflow boundaries of the computational domain. The far-field conditions should permit the prescription of external unsteady aerodynamic excitations, and allow unsteady disturbance waves coming from within the solution domain to pass through the inflow and outflow boundaries without reflection. The flow tangency condition used in the inviscid version of the NPHASE analysis is based on a two phantom-cell, pressure-symmetry, implementation to lower the generation of spurious numerical entropy and vorticity at a blade surface. In an earlier version [HSR91] of the NPHASE analysis, the computational mesh was stretched in the axial direction to dissipate outgoing waves. Recently, however, far-field conditions based on one-dimensional characteristic theory and on approximate two-dimensional characteristic theory [Gil90], have been implemented. Although, these conditions allow for the prescription of incoming unsteady excitations, they result in reflections of outgoing disturbances, if the latter have significant variation in the circumferential direction. As a result, the stretched mesh capability was applied in the NPHASE, blade vibration, calculations reported herein.

4.2 Flux Evaluations and Approximate Factorization

The flux splitting used in the NPHASE analysis is based on a similarity transformation and an eigenvalue decomposition, i.e.,

$$\frac{\partial \tilde{\mathbf{F}}}{\partial \tilde{\mathbf{U}}} = \left(\frac{\partial \tilde{\mathbf{F}}}{\partial \tilde{\mathbf{U}}} \right)^+ + \left(\frac{\partial \tilde{\mathbf{F}}}{\partial \tilde{\mathbf{U}}} \right)^- = \tilde{\mathbf{T}} (\tilde{\mathbf{A}}^+ + \tilde{\mathbf{A}}^-) \tilde{\mathbf{T}}^{-1}, \quad (4.7)$$

of the flux Jacobian matrix, $\partial \tilde{\mathbf{F}} / \partial \tilde{\mathbf{U}}$, into matrices that account for right (+) and left (-) traveling disturbances. The matrices $\tilde{\mathbf{T}}$ and $\tilde{\mathbf{T}}^{-1}$ contain the right and left eigenvectors, respectively, of $\partial \tilde{\mathbf{F}} / \partial \tilde{\mathbf{U}}$, and $\tilde{\mathbf{A}}^+$ and $\tilde{\mathbf{A}}^-$ are diagonal matrices containing the positive and negative eigenvalues.

Flux vector splitting is used to approximately factor the left-hand side of (4.5). This approximation has the form [SW81]

$$\left(\frac{\partial \tilde{\mathbf{F}}}{\partial \tilde{\mathbf{U}}} \Delta \tilde{\mathbf{U}} \right)_I = \left. \frac{\partial \tilde{\mathbf{F}}}{\partial \tilde{\mathbf{U}}} \right|_{\tilde{\mathbf{U}}_L}^+ \Delta \tilde{\mathbf{U}}_L + \left. \frac{\partial \tilde{\mathbf{F}}}{\partial \tilde{\mathbf{U}}} \right|_{\tilde{\mathbf{U}}_R}^- \Delta \tilde{\mathbf{U}}_R, \quad (4.8)$$

where the subscripts, I , L , and R refer to a cell interface and the cell volumes to the “left” and “right” of this interface, respectively. It results in first order spatial accuracy, but is only used in the approximate factorization, and therefore, does not appear in the converged final solution.

It follows from (4.8) that

$$\begin{aligned} \delta_j \left(\frac{\partial \tilde{\mathbf{F}}_j}{\partial \tilde{\mathbf{U}}} \Big|_{\tilde{\mathbf{U}}^{p-1}} \Delta \tilde{\mathbf{U}}^p \right) &= \left(\frac{\partial \tilde{\mathbf{F}}_j}{\partial \tilde{\mathbf{U}}} \Big|_{\tilde{\mathbf{U}}^{p-1}}^+ \Delta \tilde{\mathbf{U}}^p \right)_j + \left(\frac{\partial \tilde{\mathbf{F}}_j}{\partial \tilde{\mathbf{U}}} \Big|_{\tilde{\mathbf{U}}^{p-1}}^- \Delta \tilde{\mathbf{U}}^p \right)_{j+1} \\ &\quad - \left(\frac{\partial \tilde{\mathbf{F}}_j}{\partial \tilde{\mathbf{U}}} \Big|_{\tilde{\mathbf{U}}^{p-1}}^+ \Delta \tilde{\mathbf{U}}^p \right)_{j-1} - \left(\frac{\partial \tilde{\mathbf{F}}_j}{\partial \tilde{\mathbf{U}}} \Big|_{\tilde{\mathbf{U}}^{p-1}}^- \Delta \tilde{\mathbf{U}}^p \right)_j . \end{aligned} \quad (4.9)$$

The approximate factorization equation for the Newton iteration procedure is therefore

$$\tilde{\mathbf{D}} \Delta \tilde{\mathbf{U}}^p - \tilde{\mathbf{M}}_{j-1}^+ \Delta \tilde{\mathbf{U}}_{j-1}^p + \tilde{\mathbf{M}}_{j+1}^- \Delta \tilde{\mathbf{U}}_{j+1}^p = -\tilde{\Theta}(\tilde{\mathbf{U}}^{p-1} - \tilde{\mathbf{U}}^n) - \tilde{\mathbf{R}}^{p-1} + \mathcal{G}^{n+1}, \quad (4.10)$$

where j is a grid point index corresponding to the j th computational coordinate direction and p is the Newton iteration index. The \mathbf{D} and \mathbf{M} matrices are evaluated based on the state vector $\tilde{\mathbf{U}}^{p-1}$ at the previous Newton iteration. The \mathbf{D} matrix contains the diagonal elements of the iteration matrix, and the \mathbf{M}^+ and \mathbf{M}^- matrices contain the off-diagonal elements in the negative and positive computational coordinate directions, respectively. These matrices are given by

$$\begin{aligned} \tilde{\mathbf{D}} &= \tilde{\Theta} \mathbf{I} + \sum_{j=1}^3 \left(\frac{\partial \tilde{\mathbf{F}}_j}{\partial \tilde{\mathbf{U}}} \Big|_{\tilde{\mathbf{U}}^{p-1}}^+ + \frac{\partial \tilde{\mathbf{F}}_j}{\partial \tilde{\mathbf{U}}} \Big|_{\tilde{\mathbf{U}}^{p-1}}^- \right), \\ \tilde{\mathbf{M}}_{j-1}^+ &= \frac{\partial \tilde{\mathbf{F}}_j}{\partial \tilde{\mathbf{U}}} \Big|_{\tilde{\mathbf{U}}^{p-1}}^+ \quad \text{and} \quad \tilde{\mathbf{M}}_{j+1}^- = \frac{\partial \tilde{\mathbf{F}}_j}{\partial \tilde{\mathbf{U}}} \Big|_{\tilde{\mathbf{U}}^{p-1}}^- . \end{aligned} \quad (4.11)$$

Equation (4.10) is solved for $\Delta \mathbf{U}^p$ using a symmetric Gauss-Seidel subiteration procedure. After introducing l as the Gauss-Seidel iteration index, we find that the subiteration formula is given by

$$\begin{aligned} \tilde{\mathbf{D}} \Delta \tilde{\mathbf{U}}^{p,*} - \tilde{\mathbf{M}}_{j-1}^+ \Delta \tilde{\mathbf{U}}_{j-1}^{p,*} + \tilde{\mathbf{M}}_{j+1}^- \Delta \tilde{\mathbf{U}}_{j+1}^{p,l-1} &= -\tilde{\Theta}(\tilde{\mathbf{U}}^{p-1} - \tilde{\mathbf{U}}^n) - \tilde{\mathbf{R}}^{p-1} + \mathcal{G}^{n+1} \\ \tilde{\mathbf{D}} \Delta \tilde{\mathbf{U}}^{p,l} + \tilde{\mathbf{M}}_{j+1}^- \Delta \tilde{\mathbf{U}}_{j+1}^{p,l} - \tilde{\mathbf{M}}_{j-1}^+ \Delta \tilde{\mathbf{U}}_{j-1}^{p,*} &= -\tilde{\Theta}(\tilde{\mathbf{U}}^{p-1} - \tilde{\mathbf{U}}^n) - \tilde{\mathbf{R}}^{p-1} + \mathcal{G}^{n+1} \end{aligned} \quad (4.12)$$

The first subiteration is over positive grid indices; the second, over negative grid indices. The subiteration procedure is thus an LU decomposition of the Newton iteration matrix, with forward and backward substitution. Once the Gauss-Seidel subiteration procedure converges, equation (4.5) is satisfied.

As the solutions converge, any errors introduced by the Newton iteration or the approximate factorization vanish. Only the errors in the residual calculation of equation (4.1) remain. The inviscid flux terms in the residual are calculated using flux difference splitting

with a corrective flux, as given by (4.16), added to obtain higher order spatial accuracy. The flux-difference splitting approximation for the inviscid flux terms has the form [Roe81]

$$\tilde{\mathbf{F}}_I = \tilde{\mathbf{F}}(\tilde{\mathbf{U}}_L) + \frac{\partial \tilde{\mathbf{F}}}{\partial \tilde{\mathbf{U}}} \bigg|_{\tilde{\mathbf{U}}_{\text{Roe}}}^- (\tilde{\mathbf{U}}_R - \tilde{\mathbf{U}}_L) , \quad (4.13)$$

where the intermediate state vector, $\tilde{\mathbf{U}}_{\text{Roe}}$, is defined using the relations

$$\tilde{\rho}_{\text{Roe}} = \sqrt{\tilde{\rho}_L \tilde{\rho}_R} , \quad \tilde{\mathbf{V}}_{\text{Roe}} = \frac{\sqrt{\tilde{\rho}_L} \tilde{\mathbf{V}}_L + \sqrt{\tilde{\rho}_R} \tilde{\mathbf{V}}_R}{\sqrt{\tilde{\rho}_L} + \sqrt{\tilde{\rho}_R}} , \quad \text{and } E_{T,\text{Roe}} = \frac{\sqrt{\tilde{\rho}_L} \tilde{E}_{T,L} + \sqrt{\tilde{\rho}_R} \tilde{E}_{T,R}}{\sqrt{\tilde{\rho}_L} + \sqrt{\tilde{\rho}_R}} . \quad (4.14)$$

Once the inviscid fluxes have been computed, they are spatially differenced to compute the net flux through the control volume. The difference expression is

$$\delta_j \tilde{\mathbf{F}}_j = \left[\tilde{\mathbf{F}}_j \Big|_{j+\frac{1}{2}} - \tilde{\mathbf{F}}_j \Big|_{j-\frac{1}{2}} \right] , \quad (4.15)$$

where j corresponds to the computational coordinate direction, and the fractional grid indices indicate cell interfaces. The difference approximation (4.15) is first-order accurate if the flux is based only on information from adjacent cells, but higher order spatial accuracy can be achieved by adding a corrective flux. The corrective flux brings in information from additional neighboring cells, but requires the use of a flux limiter to control dispersive errors. Various flux limiting schemes exist, and the choice between them is not clear. The NPHASE code currently supports min-mod [OC84], Superbee [Roe85], and Van Leer flux limiters [VL74], with Van Leer being preferred. The limiters are activated by changes of sign in the jumps in characteristic variables at adjacent interfaces, such as occur at shocks and at stagnation points.

With the addition of a corrective flux, the flux vector has the form

$$\tilde{\mathbf{F}}_I = \tilde{\mathbf{F}}(\tilde{\mathbf{U}}_L) + \frac{\partial \tilde{\mathbf{F}}}{\partial \tilde{\mathbf{U}}} \bigg|_{\tilde{\mathbf{U}}_{\text{Roe}}}^- (\tilde{\mathbf{U}}_R - \tilde{\mathbf{U}}_L) + \frac{1}{2} \tilde{\mathbf{T}}(\tilde{\mathbf{U}}_{\text{Roe}}) [\tilde{\boldsymbol{\sigma}}^+ - \tilde{\boldsymbol{\sigma}}^-] , \quad (4.16)$$

where the limited jumps in the characteristic variables are given by

$$\tilde{\boldsymbol{\sigma}}^+ = \tilde{\mathbf{L}}(\tilde{\boldsymbol{\sigma}}_{I-1}^+, \tilde{\boldsymbol{\sigma}}_I^+) \quad \text{and} \quad \tilde{\boldsymbol{\sigma}}^- = \tilde{\mathbf{L}}(\tilde{\boldsymbol{\sigma}}_I^-, \tilde{\boldsymbol{\sigma}}_{I+1}^-) . \quad (4.17)$$

Here $I - 1$ and $I + 1$ refer to the cell interfaces to the “left” and “right” respectively, of the interface, i.e., I , under consideration. The jumps in the characteristic variables at the $I + M, M = -1, 0, 1$, cell interface are given by

$$\tilde{\boldsymbol{\sigma}}_{I+M}^\pm = \tilde{\boldsymbol{\Lambda}}^\pm(\tilde{\mathbf{U}}_{\text{Roe}}) \tilde{\mathbf{T}}^{-1}(\tilde{\mathbf{U}}_{\text{Roe}}) (\tilde{\mathbf{U}}_{R+M} - \tilde{\mathbf{U}}_{L+M}) \quad (4.18)$$

where $R + M$ and $L + M$ are the cell centers to the right and left, respectively of the interface $I + M$. The matrices $\tilde{\mathbf{T}}$ and $\tilde{\boldsymbol{\Lambda}}$ in (4.18) are computed based on Roe averaged variables, and the function \mathbf{L} in (4.17) is a generic limiting function. For example, the Van Leer limiter is defined by

$$\tilde{L}_n(\tilde{\boldsymbol{\sigma}}^1, \tilde{\boldsymbol{\sigma}}^2) = \frac{\tilde{\sigma}_n^1 \tilde{\sigma}_n^2 + |\tilde{\sigma}_n^1 \tilde{\sigma}_n^2|}{\tilde{\sigma}_n^1 + \tilde{\sigma}_n^2} , \quad (4.19)$$

where the subscript n refers to the n th component of the column vector.

4.3 Viscous Terms

The viscous flux terms appearing in equation (4.5) are evaluated at the cell interfaces, I , at each step of the Newton iteration procedure. The viscous fluxes are based on the values of state vector, $\tilde{\mathbf{U}}^{p-1}$, which are known from the previous Newton iteration, in the cell volumes to the left, L , and right, R , of the interface, i.e.,

$$\tilde{\mathbf{G}}^{TL} \Big|_I = \tilde{\mathbf{G}}^{TL}(\tilde{\mathbf{U}}_R^{p-1}, \tilde{\mathbf{U}}_L^{p-1}) . \quad (4.20)$$

The individual terms in the viscous flux vector [cf. (3.11)] are considered separately. The grid metrics, $\partial\alpha_2/\partial x_j$, are known at the current time level, and the velocity derivatives $\partial\tilde{V}_{x_j}/\partial\alpha_2$ are evaluated at the cell interface using a central difference approximation, i.e.,

$$\frac{\partial\tilde{V}_{x_j}}{\partial\alpha_2} \Big|_I = \tilde{V}_{x_j} \Big|_R - \tilde{V}_{x_j} \Big|_L . \quad (4.21)$$

The velocity components, \tilde{V}_{x_j} , and the metric Jacobian, $J^{x\alpha}$, must also be evaluated at cell interfaces. These quantities are determined by averaging their values at the adjacent cell volumes and are given by

$$\tilde{V}_{x_j} \Big|_I = \frac{1}{2} (\tilde{V}_{x_j} \Big|_R + \tilde{V}_{x_j} \Big|_L) \quad \text{and} \quad J^{x\alpha} \Big|_I = \frac{1}{2} (J^{x\alpha} \Big|_R + J^{x\alpha} \Big|_L) . \quad (4.22)$$

Once the viscous fluxes have been computed, they are spatially differenced according to

$$\delta_2 \tilde{\mathbf{G}}^{TL} = \tilde{\mathbf{G}}^{TL}_{j+\frac{1}{2}} - \tilde{\mathbf{G}}^{TL}_{j-\frac{1}{2}} \quad (4.23)$$

to compute the net flux through the control volume.

Turbulence Model

An eddy viscosity formulation has been incorporated into the NPHASE analysis to model turbulent phenomena. The eddy viscosity, $\tilde{\epsilon}$, and hence, the diffusivity, $\tilde{\epsilon}_{H_T} = \epsilon/Pr_T$, is determined using the Baldwin Lomax model [BL78] for blade boundary layers and the Thomas model [Tho79] for wakes. Thus, at blade surfaces we set

$$\tilde{\epsilon} = \begin{cases} \tilde{\epsilon}_{\text{inner}} & Y \leq Y_{\text{crossover}} \\ \tilde{\epsilon}_{\text{outer}} & Y > Y_{\text{crossover}} \end{cases} \quad (4.24)$$

where the subscripts refer to the inner and outer turbulent regions and to the interface between these regions, and Y and $Y_{\text{crossover}}$ are normal distances from a blade surface. Y is the normal distance to a cell center and $Y_{\text{crossover}}$ is the smallest normal distance at which the inner and outer values of the turbulent eddy viscosity are equal.

The turbulent eddy viscosity in the inner region of a boundary layer is determined using the Prandtl-Van Driest formulation and is given by

$$\tilde{\epsilon}_{\text{inner}} = \tilde{\rho} \ell^2 |\tilde{\omega}| , \quad (4.25)$$

where

$$\ell = \hat{X}Y \left[1 - \exp \left(-Y^+/A^+ \right) \right] \quad (4.26)$$

is a characteristic length scale and

$$|\tilde{\omega}| = \left| \frac{\partial \tilde{V}_{x_1}}{\partial x_2} - \frac{\partial \tilde{V}_{x_2}}{\partial x_1} \right| \quad (4.27)$$

is the magnitude of the vorticity. In (4.26), $\hat{X} = 0.4$ is von Karman's constant, $A^+ = 26$, and $Y^+ = (\tilde{\rho}_w \tilde{\tau}_w)^{1/2} Y / \tilde{\mu}_w$, where the subscript, w , indicates that the quantities are evaluated at the wall or blade surface. The wall shear stress, $\tilde{\tau}_w$, is given by

$$\tilde{\tau}_w = \left(\tilde{\mu} \frac{\partial \tilde{V}_{\alpha_1}}{\partial \alpha_2} \right)_w, \quad (4.28)$$

where \tilde{V}_{α_1} is the velocity component tangential to a blade surface, i.e., in the α_1 -coordinate direction, and the partial derivative is taken normal to the blade surface.

The eddy viscosity in the outer region of a boundary layer is given by

$$\tilde{\epsilon}_{\text{outer}} = K C_{cp} \tilde{\rho} F_{\text{wake}} F_{\text{Kleb}}, \quad (4.29)$$

where the Clauser constant, K , and the constant C_{cp} are set equal to 0.0168 and 1.6, respectively,

$$F_{\text{wake}} = \min \left[Y_{\text{max}} F_{\text{max}}, \frac{C_{wk} Y_{\text{max}}}{F_{\text{max}}} (\tilde{V}_{\text{max}} - \tilde{V}_{\text{min}})^2 \right], \quad (4.30)$$

the Klebanoff intermittency factor, F_{Kleb} , is given by

$$F_{\text{Kleb}} = \left[1 + 5.5 \left(\frac{C_{\text{Kleb}} Y}{Y_{\text{max}}} \right)^6 \right]^{-1}, \quad (4.31)$$

and the constant C_{Kleb} is set equal to 0.3. In equation (4.30) F_{max} and Y_{max} are determined by the function

$$F(Y) = Y |\tilde{\omega}| [1 - \exp(-Y^+/A^+)]. \quad (4.32)$$

where $F_{\text{max}} = F(Y_{\text{max}})$ is the maximum value of F at the streamwise station ($\alpha_1 = \text{constant}$) under consideration, and the constant C_{wk} is set equal to 0.25.

The wake eddy viscosity is governed by the Thomas model [Tho79], in which the eddy viscosity is defined as in (4.25), but the characteristic length scale, ℓ , is given by

$$\ell = \ell_0 (\tilde{V}_{\text{max}} - \tilde{V}_{\text{min}}) / |\tilde{\omega}|_{\text{max}}. \quad (4.33)$$

The constant ℓ_0 in (4.33) is set equal to 0.09, \tilde{V}_{max} and \tilde{V}_{min} are the maximum and minimum values, respectively, of the flow speed, and $|\tilde{\omega}|_{\text{max}}$ is the maximum value of the vorticity, at the streamwise ($\alpha_1 = \text{constant}$) station under consideration.

5. Unsteady Excitation and Aerodynamic Response

5.1 Blade Motion

We will restrict our consideration to unsteady flows in which each two-dimensional blade undergoes a rigid-body motion of the form

$$\mathcal{R}_{B_m} = \tilde{\mathbf{h}}_m(t) + [\boldsymbol{\Omega}_m(t) - \mathbf{I}] \cdot \mathbf{R}_P = \tilde{\mathbf{h}}_m(t) + (\mathbf{e}_z \times \mathbf{R}_P) \sin \tilde{\alpha}_m(t) - \mathbf{R}_P [1 - \cos \tilde{\alpha}_m(t)], \quad (5.1)$$

where

$$\boldsymbol{\Omega}_m(t) = \begin{bmatrix} \cos \tilde{\alpha}_m(t) & -\sin \tilde{\alpha}_m(t) \\ \sin \tilde{\alpha}_m(t) & \cos \tilde{\alpha}_m(t) \end{bmatrix}, \quad (5.2)$$

$\tilde{\mathbf{h}}_m(t)$ and $\tilde{\alpha}_m(t) = \tilde{\alpha}_m(t)\mathbf{e}_z$ are the translational and rotational displacement vectors, respectively, for the m th blade, \mathbf{R}_P is the distance from the steady-state position of the m th blade pitching axis at $\bar{\mathbf{x}}_{P_m} = \bar{\mathbf{x}}_P + m\mathbf{G}$ to the point $\bar{\mathbf{x}}_{B_m} = \bar{\mathbf{x}}_B + m\mathbf{G}$, and \mathbf{e}_z is a unit vector that points out from the page.

In addition, we assume that the translational and rotational displacement vectors are of the form

$$\tilde{\mathbf{h}}_m = \text{Re}\{\mathbf{h} \exp[i(\omega t + m\sigma)]\} \quad \text{and} \quad \tilde{\alpha}_m = \text{Re}\{\boldsymbol{\alpha} \exp[i(\omega t + m\sigma)]\}, \quad (5.3)$$

where \mathbf{h} and $\boldsymbol{\alpha}$ are the complex amplitudes of the reference ($m = 0$) blade translational and rotational displacements, respectively, ω is the frequency of the blade motion, σ is the phase angle between the motions of adjacent blades, and $\text{Re}\{\}$ denotes the real part of $\{\}$. In general, the components of the displacement-amplitude vectors \mathbf{h} and $\boldsymbol{\alpha}$ are complex to permit phase differences between the translational and the rotational modes of blade motion.

After expanding the trigonometric functions in (5.1) into power series in $\tilde{\alpha}_m$, we find that the rigid body motion of the m th blade can be expressed in the form

$$\mathcal{R}_{B_m}(\bar{\mathbf{x}}_{B_m}, t) = \tilde{\mathbf{r}}_{B_m} + \tilde{\boldsymbol{\alpha}}_m \times \mathbf{R}_P \sum_{n=1}^{\infty} \frac{(-1)^n \tilde{\alpha}_m^{2n}}{(2n+1)!} + \mathbf{R}_P \sum_{n=1}^{\infty} \frac{(-1)^n \tilde{\alpha}_m^{2n}}{(2n)!}. \quad (5.4)$$

Here

$$\tilde{\mathbf{r}}_{B_m} = \tilde{\mathbf{h}}_m + \tilde{\boldsymbol{\alpha}}_m \times \mathbf{R}_P = \text{Re}\{(\mathbf{h} + \boldsymbol{\alpha} \times \mathbf{R}_P) \exp[i(\omega t + m\sigma)]\} \quad (5.5)$$

is the approximate representation of a rigid-body blade motion that is used in linearized unsteady aerodynamic analyses.

5.2 Unsteady Aerodynamic Response at a Moving Blade Surface

A fluid-dynamic boundary value problem, e.g., one of those posed in § 3, must be solved numerically to determine the unsteady aerodynamic response information needed for blade row aeroelastic and aeroacoustic applications. In particular, for aeroelastic applications, information at the moving blade surfaces, e.g., surface pressures and global unsteady airloads,

is required. The pressure acting at the moving reference blade surface \mathcal{B} can be expressed in terms of the independent variables $\mathbf{x}_{\mathcal{B}}$ and t , or $\bar{\mathbf{x}}_{\mathcal{B}}$ and t , i.e.,

$$P_{\mathcal{B}} = P_{\mathcal{B}}(\mathbf{x}_{\mathcal{B}}, t) = P_{\mathcal{B}}[\bar{\mathbf{x}}_{\mathcal{B}} + \mathcal{R}_{\mathcal{B}}(\bar{\mathbf{x}}_{\mathcal{B}}, t), t] = P_{\mathcal{B}}(\bar{\mathbf{x}}_{\mathcal{B}}, t) . \quad (5.6)$$

It is usually assumed that a periodic unsteady excitation with temporal period $2\pi/\omega$ will produce an unsteady pressure response at the moving blade surface \mathcal{B} that is also periodic in time, with period $2\pi/\omega$. In this case we can write

$$\tilde{P}_{\mathcal{B}}(\bar{\mathbf{x}}_{\mathcal{B}}, t) = \sum_{n=-\infty}^{\infty} P_n(\bar{\mathbf{x}}_{\mathcal{B}}) \exp(in\omega t) = P_0(\bar{\mathbf{x}}_{\mathcal{B}}) + \sum_{n=1}^{\infty} \operatorname{Re}\{p_n(\bar{\mathbf{x}}_{\mathcal{B}}) \exp(i\omega t)\} , \quad (5.7)$$

where the Fourier coefficients, P_n , are given by

$$P_n(\bar{\mathbf{x}}_{\mathcal{B}}) = (2\pi)^{-1} \int_{\phi}^{\phi+2\pi} P_{\mathcal{B}}(\bar{\mathbf{x}}_{\mathcal{B}}, t) \exp(-in\omega t) d(\omega t), \quad n = 0, \pm 1, \pm 2, \dots . \quad (5.8)$$

Here, P_0 is the temporal mean value of the unsteady pressure and $p_n = 2P_n, n = 1, 2, \dots$ is the complex amplitude of the n th-harmonic ($n \geq 1$) component of the unsteady pressure.

The global unsteady air loads are determined by performing the appropriate integrations, involving the unsteady pressure, over a moving blade surface. For example the time-dependent force and moment acting on the reference blade are given by

$$\tilde{\mathbf{F}} = - \oint_{\mathcal{B}} \tilde{P}_{\mathcal{B}} \mathbf{n}_{\mathcal{B}} d\tau_{\mathcal{B}} \quad (5.9)$$

and

$$\tilde{M}_{\mathcal{P}} = \oint_{\mathcal{B}} \tilde{P}_{\mathcal{B}} \mathbf{n}_{\mathcal{B}} \times \mathbf{R}_{\mathcal{P}} \cdot \mathbf{e}_z d\tau_{\mathcal{B}} = - \oint_{\mathcal{B}} \tilde{P}_{\mathcal{B}} \mathbf{e}_z \times \mathbf{R}_{\mathcal{P}} \cdot \mathbf{n}_{\mathcal{B}} d\tau_{\mathcal{B}} , \quad (5.10)$$

where $\mathbf{n}_{\mathcal{B}}$ is a unit normal vector pointing out from the moving blade surface, \mathcal{B} , and $d\tau_{\mathcal{B}}$ is a differential distance along this surface, taken as positive in the counterclockwise direction. In equation (5.10) the moment is taken about the moving pitching axis located at $\mathbf{x} = \mathbf{x}_{\mathcal{P}} = \mathbf{x}_{\mathcal{P}} + \tilde{\mathbf{h}}$ and $\mathbf{R}_{\mathcal{P}} = \mathbf{x}_{\mathcal{B}} - \mathbf{x}_{\mathcal{P}}$.

Aerodynamic Work per Cycle

Two other surface response parameters, that are useful in blade aeroelastic investigations, are the aerodynamic work per cycle, W_C , and the local work per cycle or pressure-displacement function, $w_C(\bar{\mathbf{x}}_{\mathcal{B}})$ [Ver89a]. The aerodynamic work per cycle, W_C , represents the work done by the fluid on a given blade over one cycle of its motion. In particular, a prescribed, blade motion can be classified as stable, neutrally stable or unstable depending upon whether the aerodynamic work per cycle is less than, equal to, or greater than zero, respectively. The pressure-displacement function describes the distribution of the work per cycle over a blade surface. By definition

$$W_C = \oint \frac{d\tilde{W}}{dt} dt = \omega^{-1} \int_{\phi}^{\phi+2\pi} \frac{d\tilde{W}}{dt} d(\omega t) = -\omega^{-1} \int_{\phi}^{\phi+2\pi} \oint_{\mathcal{B}} \tilde{P}_{\mathcal{B}} \frac{\partial \mathcal{R}_{\mathcal{B}}}{\partial t} \cdot \mathbf{n}_{\mathcal{B}} d\tau_{\mathcal{B}} d(\omega t) \quad (5.11)$$

where \tilde{W} is the instantaneous work done by the airstream on the reference blade, and $d\tilde{W}/dt$ is the rate at which this work is done.

If the reference blade displacement, \mathcal{R}_B , and surface pressure, P_B , are expressed as functions of the independent variables \bar{x}_B and t , as in (5.4) and (5.6), then an integral over the moving blade surface \mathcal{B} can be referred to the mean or steady-state position, B , of this surface. In this case, the order of the integrations used to determine the work per cycle can be interchanged. For a rigid blade motion $d\tau_B = d\bar{\tau}_B$, and

$$W_C = -\omega^{-1} \oint_B \int_{\phi}^{\phi+2\pi} \tilde{P}_B \frac{\partial \mathcal{R}_B}{\partial t} \cdot \mathbf{n}_B d(\omega t) d\bar{\tau}_B = \oint_B w_C(\tau_B) d\bar{\tau}_B. \quad (5.12)$$

The function

$$w_C(\bar{\tau}_B) = -\omega^{-1} \int_{\phi}^{\phi+2\pi} \tilde{P}_B \frac{\partial \mathcal{R}_B}{\partial t} \cdot \mathbf{n}_B d(\omega t) \quad (5.13)$$

is the local work per cycle or pressure-displacement function. The unit normals \mathbf{n}_B and $\bar{\mathbf{n}}_B$ at the moving (\mathcal{B}) and steady-state (B) positions, respectively, of the reference blade surface, are related by

$$\mathbf{n}_B = \left| \bar{\tau}_B + \frac{\partial \mathcal{R}_B}{\partial \bar{\tau}_B} \right|^{-1} \left(\bar{\mathbf{n}}_B + \frac{\partial \mathcal{R}_B}{\partial \bar{\tau}_B} \times \mathbf{e}_z \right). \quad (5.14)$$

Here \mathbf{n}_B and $\bar{\mathbf{n}}_B$ point outward from the blade surface and the unit tangent vector, $\bar{\tau}_B$, points in the counterclockwise direction.

Small-Amplitude Blade Motions

If we restrict our consideration to rigid-body blade displacements of small-amplitude, we can set

$$\mathcal{R}_B = \tilde{\mathbf{r}}_B - \tilde{\alpha}^2 \mathbf{R}_P / 2 + \dots, \quad (5.15)$$

$$\mathbf{n}_B = \bar{\mathbf{n}}_B (1 - \tilde{\alpha}^2 / 2) + \tilde{\alpha} \bar{\tau}_B + \dots, \quad (5.16)$$

and

$$\frac{\partial \mathcal{R}_B}{\partial t} \cdot \mathbf{n}_B = \tilde{\alpha} \dot{\mathbf{r}}_B \cdot \bar{\tau}_B + (\dot{\mathbf{r}}_B \cdot \tilde{\alpha} \dot{\mathbf{R}}_P) \cdot \bar{\mathbf{n}}_B + \dots, \quad (5.17)$$

where the dots refer to terms that are of $\mathcal{O}(|\mathcal{R}_B|^3)$ or higher. If $\tilde{\mathbf{h}}$ and $\tilde{\alpha}$ are harmonic in time with frequency ω as in equation (5.3), then

$$\frac{\partial \mathcal{R}_B}{\partial \tau} \cdot \mathbf{n}_B = \frac{i\omega}{2} \sum_{m=0}^2 [R_m \exp(im\omega t) - R_m^* \exp(-im\omega t)] + \dots, \quad (5.18)$$

where $R_0 = \alpha^* \mathbf{r}_B \cdot \bar{\tau}_B / 2$, $R_1 = \mathbf{r}_B \cdot \bar{\mathbf{n}}_B$, and $R_2 = (\alpha \mathbf{r}_B \cdot \bar{\tau}_B - \alpha^2 \mathbf{R}_P \cdot \bar{\mathbf{n}}_B) / 2$. After substituting (5.18) and the Fourier series expansion for the surface pressure, equation (5.7), into equation (5.13) and carrying out the integrations with respect to ωt , we find that

$$w_C = -\pi \operatorname{Im} [P_0 \alpha \mathbf{r}_B^* \cdot \bar{\tau}_B + p_1 \mathbf{r}_B^* \cdot \bar{\mathbf{n}}_B + p_2 (\alpha^* \mathbf{r}_B^* \cdot \bar{\tau}_B - \alpha^{*2} \mathbf{R}_P \cdot \bar{\mathbf{n}}_B) / 2] + \dots. \quad (5.19)$$

If, as in linearized unsteady aerodynamic calculations, we assume that the steady pressure is of $\mathcal{O}(1)$ and the n th harmonic of the unsteady pressure is of $\mathcal{O}(|\mathcal{R}_B|^n)$, then

$$w_C = -\pi \operatorname{Im} \{P_0 \alpha \mathbf{r}_B^* \cdot \bar{\tau}_B + p_1 \mathbf{r}_B^* \cdot \bar{\mathbf{n}}_B\} + \mathcal{O}(|\mathcal{R}_B|^4). \quad (5.20)$$

Thus, the higher harmonic content ($n \geq 2$) of the unsteady flow would have a negligible impact on the energy transfer from the airstream to the rigid-body blade motion. Even if the unsteady components, p_n , $n = 1, 2, 3 \dots$ of the fluid pressure are all of the same order, i.e., $\mathcal{O}(|\mathcal{R}_B|)$, then to leading order, i.e., $\mathcal{O}(|\mathcal{R}_B|^2)$, the pressure-displacement function would depend only upon the steady and the first harmonic components of the fluid pressure. Thus, for harmonic, rigid body, blade motions of sufficiently small amplitude, the higher harmonic content of the unsteady pressure response should have a negligible impact on the transfer of energy from the fluid to the structural motion. This analytical result can be used to guide the interpretation and validation of the unsteady aerodynamic response predictions that are determined using the time-accurate, nonlinear, analysis NPHASE.

6. Numerical Results

Unsteady aerodynamic response predictions will be presented for two-dimensional, inviscid and viscous (at $Re = 10^6$), flows through a compressor-type ($M_{+\infty} < M_{-\infty}$) cascade to demonstrate and validate the current capabilities of the NPHASE analysis and code. The cascade, known as the Tenth (10th) Standard Configuration [FS83, FV93], consists of modified NACA 5506 airfoils, i.e., the airfoil thickness distribution has been modified so that the blades close in wedge-shaped trailing edges. It has a stagger angle, Θ , of 45 deg and a gap/chord ratio, G , of unity, and operates at uniform subsonic inflow conditions. We will consider unsteady flows through the 10th Standard Cascade operating at an inlet freestream Mach number $M_{-\infty}$ and flow angle, $\Omega_{-\infty}$, of 0.7 and 55 deg respectively, and at an inlet freestream Mach number and flow angle of 0.8 and 58 deg. In the first case the steady background flow is entirely subsonic; in the second, it is transonic with a normal shock emanating from the suction surface of each blade.

In particular, we will consider unsteady flows excited by prescribed single-degree-of-freedom (SDOF), harmonic, blade motions. The latter occur at unit frequency and with constant phase angle σ between the motions of adjacent blades. The motions considered are pure translations normal to the blade chords (bending) and pure rotations (torsion) about axes at the blade midchords. The blade motions are termed subresonant if all acoustic response disturbances attenuate with increasing axial distance from the blade row, superresonant (m, n) if m and n such disturbances persist in the far upstream and far downstream regions, respectively, and carry energy away from the blade row, and resonant if at least one acoustic response disturbance persists in either the far upstream or far downstream regions of the flow and carries energy along the blade row [Ver89b].

In addition to the NPHASE results, for purposes of comparison, we will also present linear response predictions as determined using the LINFLO analysis. In the latter, the unsteady flow is regarded as a small inviscid perturbation of a potential steady background flow. The full-potential analysis CASPOF [Cas83] is used to provide steady background flow information needed for the LINFLO calculations.

6.1 Computational Data, Steady Background Flows

Nonlinear steady and unsteady solutions have been determined for subsonic and transonic flows, by applying the NPHASE analysis on H-type meshes. An H-mesh consisting of 141 axial and 41 tangential lines is used for the inviscid subsonic calculations. For inviscid transonic flows, the 161×41 H-mesh, shown in Figure 4, is applied, and 141×81 and 161×81 meshes are used for the viscous subsonic and transonic calculations, respectively. These meshes extend 5 axial chords upstream and 9 axial chords downstream from the blade row. For the inviscid subsonic calculations, the average normal grid spacing adjacent to a blade is 0.1% of chord and 55 points are placed along the blade surfaces. For the inviscid transonic calculations the average normal grid spacing adjacent to a blade is 0.05% of chord, and 75 points are placed on the blades. The mesh spacings for the viscous calculations are defined such that the law-of-the-wall coordinate, Y^+ , has an average value of approximately 2.0 over a blade surface. This requires decreasing the average normal grid spacing adjacent to the blade surface to 0.005% of chord for the viscous subsonic and transonic calculations.

The full potential steady (CASPOF) and the linearized inviscid unsteady (LINFLO) solutions are determined on composite meshes consisting of local C-meshes embedded in global H-meshes [Cas83, UV91]. The C-meshes are used to accurately resolve the steady and unsteady flows around blade leading edges and through normal shocks, and to permit shock fitting in the LINFLO calculation. The H- and C-meshes used in the LINFLO calculations consist of 155 axial and 41 tangential lines and 101 radial and 11 circumferential lines, respectively. Radial mesh lines are concentrated near shocks in the transonic calculations. A typical transonic mesh is shown in Figure 5. Since analytic far-field conditions are applied in LINFLO, the H-mesh extends only one axial chord upstream and downstream from the blade row.

The numerical solutions, reported herein, were determined on an IBM-370 Workstation. Converged, NPHASE, steady solutions were obtained after 1,000 iterations for an inviscid calculation and 2,000 iterations for a viscous calculation. The steady subsonic inviscid and viscous solutions required 21 and 52 CPU minutes, respectively, to converge; the corresponding steady transonic solutions, 25 and 61 CPU minutes. The NPHASE unsteady calculations were started from the appropriate steady solution, and performed with 1,000 time-steps per cycle of blade motion with 3 Newton iterations per time step and 3 symmetric Gauss-Siedel iterations per Newton iteration. Four cycles of motion were used to converge the nonlinear inviscid and viscous solutions to a periodic state. The subsonic inviscid calculations required about 48 CPU min per blade passage, and the subsonic viscous calculations required 128 CPU min per blade passage. For the transonic inviscid and viscous solutions, 57 and 153 CPU min per blade passage, respectively, were required for convergence. The number of blade passages required for a nonlinear unsteady calculation depends upon the interblade phase angle. For example, if $\sigma = 60$ deg, six passages are needed. Steady full potential solutions were obtained, using CASPOF, within 10 CPU seconds, and LINFLO, linearized, inviscid solutions required about 90 CPU seconds per unsteady case.

Steady Background Flows

Predicted steady surface pressure, P , and skin-friction, $\bar{\tau}_w$, distributions for the steady subsonic ($M_{-\infty} = 0.7, \Omega_{-\infty} = 55$ deg) and transonic ($M_{-\infty} = 0.8, \Omega_{-\infty} = 58$ deg) flows are shown in Figures 6 and 7, respectively. The inviscid (full-potential and Euler) subsonic predictions for the blade surface pressures (Figure 6a) are in very close agreement. These results along with the viscous (thin-layer Navier-Stokes) predictions indicate that viscous-displacement effects cause a slight reduction in the steady blade pressure loading, i.e., $P(\bar{x}, 0^-) - P(\bar{x}, 0^+)$, where the superscripts $-$ and $+$ refer to the lower (pressure) and upper (suction) surfaces of the blade, over the rear half of the blade. The surface skin-friction distributions (Figure 6b) indicate that the viscous flow at $Re = 10^6$ separates (i.e., $\bar{\tau}_w < 0$) from the suction surface of each blade and reattaches just upstream of the trailing edge. The exit conditions, i.e., the exit freestream (isentropic) Mach number, $M_{+\infty}$, and flow angle, $\Omega_{+\infty}$, and the mean lift force acting on each blade, $F_y = \mathbf{F} \cdot \mathbf{e}_y$, as predicted by the three analyses are as follows: the full-potential indicates that $M_{+\infty} = 0.446$, $\Omega_{+\infty} = 40.2$ deg, and $F_y = 0.348$; the Euler analysis, that $M_{+\infty} = 0.446$, $\Omega_{+\infty} = 39.8$ deg, and $F_y = 0.348$; and the Navier-Stokes analysis yields $M_{+\infty} = 0.461$, $\Omega_{+\infty} = 41.2$ deg and $F_y = 0.324$. According to these results, viscous-displacement effects cause a 7% reduction in the steady lift force that acts on each blade.

For the subsonic cascade configuration operating at $M_{-\infty} = 0.7$ and $\Omega_{-\infty} = 55$ deg, if we set $M_{+\infty} = 0.446$ and $\Omega_{+\infty} = 40.2$ deg, the resonant interblade phase angles (in degrees) for harmonic unsteady excitations at constant interblade phase angle are $\sigma_{-\infty}^- = -26.93\omega$, $\sigma_{-\infty}^+ = 117.12\omega$, $\sigma_{+\infty}^- = -31.80\omega$ and $\sigma_{+\infty}^+ = 59.79\omega$. Here the subscripts refer to the far upstream ($-\infty$) or far downstream ($+\infty$) regions, and the superscripts indicate that there are two resonant interblade phase angles associated with each of these regions. The blade motions at interblade phase angles lying between the lowest ($\sigma_{+\infty}^-$) and highest ($\sigma_{-\infty}^+$) resonant interblade phase angles are superresonant.

The inviscid surface pressure distributions (Figure 7a) for the steady transonic flow at $M_{-\infty} = 0.8$ and $\Omega_{-\infty} = 58$ deg are in good agreement, but differences occur in the vicinity of the shock and in the supersonic region lying adjacent to a blade suction surface and upstream of the shock. Viscous effects reduce the pressure loading over most of the blade and smear the pressure change across the shock. The transonic flow separates downstream of the shock and is more or less separated from the suction surface from just aft of the shock to a point just upstream of the trailing edge. For the transonic flow at $M_{-\infty} = 0.8$, $\Omega_{-\infty} = 58$ deg the potential analysis indicates that $M_{+\infty} = 0.432$, $\Omega_{+\infty} = 40.3$ deg, $F_y = 0.412$, and the isentropic Mach numbers at the base of each shock are 1.292 on the upstream side and 0.794 on the downstream side. The Euler analysis yields $M_{+\infty} = 0.432$, $\Omega_{+\infty} = 40.0$ deg, $F_y = 0.408$, and Mach numbers at the base of a shock of 1.22 and 0.871. The Navier-Stokes results are $M_{+\infty} = 0.461$, $\Omega_{+\infty} = 42.6$ deg and $F_y = 0.372$, and the Mach number is continuous, but rapidly varying through the shock. The lift, F_y , predictions indicate that viscous effects lead to a reduction of approximately 9% in the lift force acting on each blade. For the transonic configuration operating at $M_{-\infty} = 0.8$ and $\Omega_{-\infty} = 58$ deg, if $M_{+\infty} = 0.432$ and $\Omega_{-\infty} = 40.3$ deg, the resonant interblade phase angles are: $\sigma_{-\infty}^- = -28.94\omega$, $\sigma_{-\infty}^+ = 201.7\omega$, $\sigma_{+\infty}^- = -35.92\omega$ and $\sigma_{+\infty}^+ = 66.22\omega$.

6.2 Unsteady Subsonic Flows

We proceed to consider unsteady flows through the subsonic ($M_{-\infty} = 0.7$, $\Omega_{-\infty} = 55$ deg) 10th Standard Configuration that are excited by a unit frequency ($\omega = 1$) in-phase ($\sigma = 0$ deg) torsional blade motion with amplitude $|\alpha| = 2$ deg, and by a unit frequency, out-of phase ($\sigma = 180$ deg), bending vibration with $|h_y| = 0.01$. In particular, we set $\alpha = \alpha \mathbf{e}_z = (2 \text{ deg}, 0) \mathbf{e}_z$ and $\mathbf{h} = h_y \mathbf{e}_y = (0.01, 0) \mathbf{e}_y$ to define the torsional and bending vibrations [cf. (5.3)]. The in- and out-of-phase blade motions are superresonant (1,1) and subresonant, respectively. The instantaneous surface pressure distributions for $\omega t = 90, 180, 270$ and 360 deg, as predicted using the nonlinear inviscid and viscous ($Re = 10^6$) analyses, are shown in Figures 8 and 9, respectively. The inviscid and viscous unsteady pressure predictions are very similar. They indicate that viscous effects cause a small reduction in the time-averaged or mean pressure loading over the latter half of a blade, but these effects have a negligible impact on the unsteady surface pressure fluctuations.

We have post-processed the NPHASE subsonic, inviscid and viscous, unsteady solutions to provide information on the local (ω_C) and global (W_C) works per cycle in Figures 10 and 13, and on the harmonic components, p_n , of the unsteady surface pressures in Figures 11, 12, 14 and 15. The unsteady response information determined from the inviscid and viscous solutions is nearly identical. Therefore, we include only the results of the nonlinear inviscid

calculations in Figures 10 through 15, along with the linearized inviscid results, determined using LINFL0.

The predicted local work-per-cycle or pressure-displacement function distributions and the corresponding global works per cycle for the in-phase torsional vibration are given in Figure 10. The NPHASE results in Figure 10a are based on the inviscid or Euler predictions for the nonlinear unsteady pressure; those in Figure 10b, on the Euler predictions for the first-harmonic component of the unsteady pressure. The agreement between the NPHASE nonlinear, the NPHASE first-harmonic, and the LINFL0 predictions for ω_C and W_C is excellent, indicating that the unsteady fluctuations in this subsonic flow are essentially linear perturbations of the underlying steady background flow. The Navier Stokes solutions for the unsteady viscous flow at $Re = 10^6$ provide local work per cycle distributions that are quite similar to those given in Figure 10, but the viscous nonlinear and first-harmonic predictions for $|\alpha^{-2}|W_C$ are -0.61 and -0.60 , respectively. Thus, the viscous-displacement effect on the unsteady local and global work per cycle responses is small, and it is captured essentially by the first-harmonic component of the unsteady viscous solution.

The real and imaginary components of the first two harmonics of the unsteady pressure are shown in Figures 11 and 12, respectively. These components describe unsteady pressures that are in-(real) and out-of-(imaginary) phase with the blade displacement. The NPHASE first-harmonic inviscid results, shown in Figures 11 and 12, as well as the corresponding viscous results (not shown), are in very good agreement with the LINFL0 predictions. However, differences between the NPHASE and LINFL0 predictions for $Re\{p_1\}$ occur on both the suction and pressure surfaces near the blade leading edge. These differences could be due to the use of a stretched mesh in the nonlinear calculation or, possibly, to a breakdown in the linearized inviscid approximation at blunt blade leading edges. Such differences do not occur in the results for $Im\{|\alpha|^{-1}p_1\}$, nor therefore, in the local work per cycle predictions. The second (and higher) harmonics of both the inviscid and viscous unsteady surface pressure response are quite small, and therefore, these have a negligible impact on the energy transferred from the airstream to the blade (W_C) over a cycle of blade motion.

Similar results for the out-of-phase bending vibration are shown in Figures 13 through 15. Again the NPHASE nonlinear and first-harmonic inviscid predictions for the local and global works per cycle are in very good agreement with the LINFL0 predictions (Figure 13). The corresponding NPHASE viscous predictions for $|\alpha^{-2}|\omega_C$ are closely aligned with the curves in Figure 13, but, for the viscous flow at $Re = 10^6$, the NPHASE nonlinear and first-harmonic predictions for $|\alpha^{-2}|W_C$ are both equal to -8.06 . The inviscid unsteady pressure predictions in Figures 14 and 15, as well as the corresponding viscous predictions, indicate an excellent agreement between the NPHASE, first-harmonic and the LINFL0 predictions for the unsteady pressure, except near a blade leading edge, where the two predictions for the in-phase component of the first-harmonic unsteady pressure differ significantly. Also, the second and higher harmonics of the unsteady pressure are negligible. Thus, for this essentially attached, unsteady subsonic flow, the effects of viscous displacement on the unsteady pressure response are small, and this response is essentially captured by the first-harmonic component of the nonlinear unsteady pressure.

The behavior of the global work-per-cycle vs. interblade phase angle is indicated in Figure 16 for pure bending and pure torsional vibrations, at unit frequency, of the subsonic 10th Standard Cascade. The vertical lines at the top of the figure indicate the resonant

interblade phase angles for a unit frequency excitation. The curves in Figure 16 indicate that SDOF torsional and bending motions at unit frequency are stable ($W_C < 0$) and that the torsional vibrations generally have the lower stability margin. The NPHASE results in Figure 16 are based upon the nonlinear viscous and inviscid solutions for the unsteady pressure. The corresponding predictions, based on the first-harmonic component of the unsteady pressure, are almost identical to the results given in Figure 16. Also, the NPHASE and LINFL0 global response predictions are in very good agreement. The greatest deviation occurs at $\sigma = 120$ deg, which is near the upstream resonance condition, $\sigma = \sigma_{-\infty}^+$. The result agreement indicated in Figure 16 demonstrates the accuracy of both analyses, NPHASE and LINFL0, over the entire range of interblade phase angles. The relatively small differences between the LINFL0 and the NPHASE inviscid and viscous solutions indicate that nonlinear and viscous effects have a negligible impact on the aeroelastic stability margins for pure torsional and bending vibrations of the 10th Standard Cascade.

The foregoing parametric study on high Mach number, subsonic, essentially attached, unsteady flows, excited by small-amplitude blade motions, reveals an excellent agreement between the results of a nonlinear Euler, a thin-layer Navier-Stokes and a linearized inviscid analysis. For the flows considered, the essential response information needed for aeroelastic studies, is contained in the first-harmonic component of the unsteady surface pressure response, and this component can be determined using a linearized inviscid analysis. Viscous-displacement effects have very little impact on unsteady surface pressure responses, and therefore, on the aeroelastic stability margin for a given blade motion.

6.3 Unsteady Transonic Flows

Next, we consider unsteady transonic ($M_{\infty} = 0.8, \Omega_{\infty} = 58$ deg) flows through the 10th Standard Cascade. Again we consider blade motions at $\omega = 1$ and examine, in some detail, the unsteady responses to in-phase torsional (at $|\alpha| = 1$ deg) and out-of-phase bending ($|h_y| = 0.01$) vibrations. The torsional amplitude is set at 1 deg so that the shocks remain present throughout the unsteady motion. Our calculations have shown that for $|\alpha| = 2$ deg, the shocks disappear when the blades are in their mean positions ($\tilde{\alpha} = 0$) and rotating clockwise at $\dot{\tilde{\alpha}} = -\omega\alpha$, i.e., at $\omega t = (90 + 360n)$ deg, $n + 0, \pm 1, \pm 2, \dots$. For the transonic operating condition the in-phase blade motions are superresonant (1,1) and the out-of-phase motions are superresonant (1,0).

Instantaneous surface pressure distributions at $\omega t = 90, 180, 270$ and 360 deg as predicted by the inviscid and viscous (for $Re = 10^6$) versions of the NPHASE analysis are shown in Figures 17 and 18, respectively. These results indicate that the unsteady pressure fluctuations on the suction surface are considerably stronger than those on the pressure surface, particularly in the vicinity of the shock. Also, an observer stationed between the extreme shock positions would experience large changes in pressure as the shock passes by. Finally, viscous effects tend to smear the shock, reduce unsteady pressure fluctuations in the vicinity of the shock, and reduce the impulsive loads associated with shock displacement.

The pressure-displacement function distributions and global work per cycle predictions determined using the NPHASE, thin-layer Navier-Stokes and Euler analyses and the LINFL0 linear inviscid analysis are shown in Figure 19 for the in-phase torsional blade motion. The NPHASE results in Figure 19a are based on the time-dependent, nonlinear, unsteady

pressure; those in Figure 19b, on the first-harmonic component of the unsteady pressure. Shock phenomena are captured in NPHASE and, although shocks are resolved accurately and sharply at each instant of time, the integrations used to determine the harmonic content of the unsteady pressure [cf. (5.8)] and the local work per cycle [cf. (5.13)] tend to smear the unsteady loads in the vicinity of the shock. In contrast, LINFLO is a frequency domain analysis in which shocks are “fitted” by imposing shock-jump conditions at the mean or steady state shock positions. This leads to the prediction of concentrated shock loads, represented by the δ functions in Figure 19, that depend on the product of the steady pressure jump across the shock and the shock displacement, and first-harmonic unsteady surface pressures that are discontinuous at the shock, but continuous elsewhere.

The results in Figure 19 indicate that the nonlinear viscous and inviscid solutions are in close agreement except in the vicinity of the shock. Viscous displacement effects tend to shift the mean shock position slightly upstream and to weaken the impulsive shock load. Also, local and global work per cycle predictions, based on the first-harmonic component of the nonlinear solutions for the pressure, are in excellent agreement with the predictions based on the full nonlinear pressure. Thus, viscous-displacement effects have only a small impact, and the higher harmonics of the unsteady pressure response have a negligible impact, on the stability of the blade motion. The NPHASE and LINFLO results differ substantially in the vicinity of the shock and in the supersonic region upstream of the shock, but they are in close agreement on the blade suction surface downstream of the shock and over the entire blade pressure surface. Differences at the shock are to be expected because of the different methods used to determine the unsteady aerodynamic response information. The differences in the supersonic region upstream of the shock are unexpected and at this point not well understood. They could be associated with the use of a stretched grid for the NPHASE calculations.

The real and imaginary parts of the first two harmonics of the unsteady surface pressure for the in-phase torsional blade motion, as determined from the NPHASE viscous and inviscid solutions, are shown in Figures 20 and 21. Similar results of the NPHASE, nonlinear, and the LINFLO, linearized, inviscid analyses are shown in Figures 22 and 23. The nonlinear viscous and inviscid results are in close agreement (Figures 20 and 21), except in the vicinity of the shock. Also, the second and higher harmonic components of the unsteady pressure are quite small, except in the region traversed by the shock. The NPHASE predictions for the first-harmonic pressure differ substantially from the corresponding linearized inviscid solutions (Figures 22 and 23) near the blade leading edge, in the vicinity of the shock, and in the supersonic region upstream of the shock. The nonlinear and the linearized inviscid solutions for the first-harmonic pressure response are in good agreement in subsonic regions of the flow, i.e., on the suction surface downstream of the shock and over most of the pressure surface. It should be noted that the LINFLO predictions shown in Figures 22 and 23 only describe the first-harmonic unsteady pressure and not the anharmonic unsteady pressure loading caused by shock motion.

Local and global work per cycle predictions for the out-of-phase bending vibration of the transonic cascade are shown in Figure 24. Again, with the exception of the shock loads, the nonlinear viscous (at $Re = 10^6$) and inviscid solutions are in good agreement. The viscous displacement effect shifts the mean shock location slightly upstream and weakens the unsteady shock loads. The results for $\omega_C(x)$ and W_C , based on the nonlinear and the

first-harmonic unsteady pressure, are in very close agreement indicating that the energy transfer between the fluid and the blade motion is almost entirely due to the first-harmonic response characteristics of the fluid. The linearized inviscid analysis, LINFLO, predicts very high and very low values of the local work per cycle just upstream and just downstream of the shock, respectively. These are caused by the first-harmonic unsteady pressure response. The LINFLO analysis also predicts a large anharmonic local unsteady response due to shock motion, which is represented by the delta functions in Figure 24. The NPHASE and LINFLO results on the suction surface, away from the shock, and on the pressure surface are in good agreement, but the two analyses predict very different shock loads.

The NPHASE viscous and inviscid predictions for the real and imaginary components of the first and second harmonics of the unsteady surface pressure, for the out-of-phase bending vibration are shown in Figures 25 and 26. The corresponding NPHASE nonlinear inviscid and LINFLO linearized inviscid results are given in Figures 27 and 28. Again, the results of the nonlinear viscous and inviscid analyses are in close agreement, except in the region traversed by the shock, where a relatively large second and higher (not shown) harmonic components of the unsteady pressure persist. The NPHASE inviscid predictions for the real and imaginary components of the first-harmonic unsteady pressure differ substantially from the LINFLO predictions at the blade leading edge, in the supersonic region upstream of the shock, and in the vicinity of the shock.

Global work-per-cycle predictions, based on the NPHASE Navier-Stokes and Euler analyses and on the LINFLO linearized inviscid analysis, are shown in Figure 29 for unit-frequency torsional and bending vibrations of the 10th Standard Cascade. The NPHASE viscous and inviscid results are in fairly close agreement, indicating that for the unsteady flows considered viscous-displacement effects are of limited importance, but they do tend to reduce the stability margins for the torsional blade vibrations. The results of the NPHASE analyses and the LINFLO analysis show similar trends, but significant quantitative differences, particularly for the bending vibrations. These differences are due to the relatively large discrepancies between the local response predictions of the two analyses at shocks and in supersonic regions. Work per cycle predictions, based on the NPHASE viscous and inviscid predictions for the first-harmonic unsteady pressure, agree very closely with the nonlinear results shown in Figure 29, again indicating that, even in transonic flows, the stability margin for a given blade motion is essentially determined by the first-harmonic component of the unsteady pressure response.

The results of the foregoing parametric study for transonic flows are not as comforting or convenient as those determined previously for subsonic flows. The most important concerns are the discrepancies between the nonlinear predictions and the linearized inviscid predictions in supersonic regions and in the vicinity of shocks. The discrepancies in supersonic regions could, perhaps, be eliminated by incorporating accurate, unsteady, far-field conditions into the NPHASE analysis, to avoid the use of stretched H-meshes (see Figure 4). The ways in which shocks and their motions are modeled in nonlinear and linearized unsteady codes must be understood more clearly to resolve the differences between the NPHASE and LINFLO predictions in the vicinity of shocks. Finally, although viscous-displacement effects are generally small for unsteady transonic flows with small-scale boundary layer separations, such effects can be important shock regions. Therefore, viscous effects should be incorporated into the approximate unsteady aerodynamic analyses intended for transonic aeroelastic design ap-

plications. An encouraging result of the transonic parametric studies is the close agreement obtained between the local and global work per cycle predictions that were based on the NPHASE nonlinear and first-harmonic pressure responses. This suggests that a linearized analysis that accounts for viscous-displacement effects would be useful for predicting the flutter characteristics of turbomachinery blading over a wide range of operating conditions.

7. Concluding Remarks

A modern implicit, time-marching, Euler/Navier-Stokes analysis (NPHASE) has been applied to simulate two-dimensional subsonic and transonic unsteady flows through a vibrating cascade, in particular, the Tenth (10th) Standard Cascade of Ref. [FV93]. The vibrations considered are pure translations normal to the blade chords (bending) and pure rotations about axes at blade midchords (torsion). Linearized inviscid response predictions, as determined using the LINFL0 code, have also been determined to help validate and illustrate the Euler/Navier-Stokes capabilities for unsteady cascade flows. The NPHASE numerical results have also been interrogated to assess the importance of nonlinear and viscous effects on the unsteady aerodynamic response of blades vibrating at a frequency representative of those at which flutter occurs in modern fans and compressors.

The numerical simulations for the steady and unsteady subsonic flows indicate that viscous effects tend to have a small impact on steady blade loading and a negligible impact on the unsteady loading. In addition, the unsteady surface pressure fluctuations are essentially linear. The results of the NPHASE Euler analysis and a full potential analysis for steady flow are in excellent agreement. The steady viscous flow predictions, for $Re = 10^6$, exhibit a small decrease in the blade pressure loading on the pressure surface over the rear half of the blade and a small region of separated flow on the suction surface extending from 88 to 98% of the blade chord. The unsteady simulations show that the viscous and inviscid response predictions, i.e., the local and global works per cycle and the unsteady surface pressures are in close agreement. The stability of the blade motion is essentially determined by the first-harmonic component of the unsteady pressure, as the second- and higher-harmonic components are quite small. The LINFL0 linearized inviscid predictions for the unsteady response quantities are in excellent agreement with both the NPHASE Euler and Navier-Stokes predictions.

For the steady and unsteady transonic flows, the numerical simulations indicate that accurate predictions of steady and unsteady surface pressures depend significantly upon an adequate resolution of shock strength and the positions at which shocks impinge on blade surfaces. For the steady flow, the Euler and Full Potential results for the surface pressure are in excellent agreement at points along the blade surface at which the flow is subsonic, but differ somewhat in the supersonic region upstream of the suction-surface shock and in the vicinity of this shock. Navier-Stokes predictions for the corresponding viscous flow at $Re = 10^6$ indicate that viscous displacement effects tend to weaken and smear the shocks, increase the pressures on the suction surface in the vicinity of the leading edge and reduce the pressures along the pressure surface of the blade. The viscous steady flow separates from the suction surface downstream of the shock, and is either separated or on the verge of separation from the shock to a point just upstream of the trailing edge.

Predictions for the unsteady transonic flows indicate that the unsteady pressure fluctuations on the suction surface are much stronger than those on the pressure surface, with severe fluctuations in surface pressure resulting from the motion of a shock. Viscous effects diminish the strength of the impulsive unsteady loads associated with shock motion. Also, viscous-displacement effects have only a small impact on global and local work per cycle predictions, causing significant changes in the local work per cycle predictions only in the vicinity of a shock. The transonic unsteady simulations indicate that large second- and higher-harmonic pressure variations occur in the region traversed by a shock, but the

higher-harmonic content of the unsteady pressure response has only a negligible impact on the local and global work per cycle responses, and hence, on the stability margins for the blade motions. Unfortunately, the LINFLO linearized inviscid results are not in good agreement with the nonlinear predictions in the vicinity of shock and in the supersonic region upstream of the shock. The linearized inviscid results are in reasonable agreement with the nonlinear inviscid and viscous predictions in subsonic regions of the flow.

There remain several issues which require further study before the impact of nonlinear and viscous displacement effects, as they apply to blade flutter prediction, can be fully understood. The present investigation has indicated that fully two-dimensional, unsteady far-field conditions should be implemented into the NPHASE code to avoid the need for calculating unsteady flows on stretched H-meshes. If NPHASE and LINFLO calculations are performed on similar H-meshes, the discrepancies between the results of the two analyses in supersonic regions and near blade leading edges may disappear. Also, a better understanding of shock phenomena is warranted. The goals here should be to bring the NPHASE and LINFLO unsteady transonic predictions into closer agreement, and to understand more clearly the reasons for the differences between the shock loads predicted by the two analyses.

The parametric studies conducted under the present effort pertained to inviscid flows and fully-turbulent, viscous flows at high Reynolds number. Any shocks occurring in these flows were present throughout the unsteady motion, and boundary layer separations were of limited extent. NPHASE has proven to be a robust code for such applications, which can give useful insights into the effects of nonlinear and viscous unsteady aerodynamic phenomena on blade response. Future research should be directed towards investigating unsteady flows in which shocks appear and disappear within a cycle of blade motion to gain insight into the importance of large shock excursions and their impact on aeroelastic stability. Also, unsteady flows in which large-scale viscous-layer separations occur should be investigated. Finally, the impact of various turbulence and transition models on predicted unsteady aerodynamic response behaviors should also be investigated.

8. References

[BH92] T. A. Beach and G. Hoffman. IGB Grid: User's Manual (A Turbomachinery Grid Generation Code). CR 189104, NASA, January 1992.

[BL78] B. S. Baldwin and H. Lomax. Thin-Layer Approximation and Algebraic Model for Separated Turbulent Flow. AIAA Paper 78-257, 16th Aerospace Sciences Meeting, Huntsville, Alabama, January 16–18 1978.

[Cas83] J. R. Caspar. Unconditionally Stable Calculation of Transonic Potential Flow through Cascades using an Adaptive Mesh for Shock Capture. *Transactions of the ASME: Journal of Engineering for Power*, 105(3):504–513, July 1983.

[CS74] T. Cebeci and A. M. O. Smith. *Analysis of Turbulent Boundary Layers*, pages 211–239. Academic Press, New York, 1974.

[DV94] D. J. Dorney and J. M. Verdon. Numerical Simulation of Unsteady Cascade Flows. *Trans. of the ASME: Journal of Turbomachinery*, 116(4):665–675, October 1994.

[FS83] T. H. Fransson and P. Suter. Two-Dimensional and Quasi Three-Dimensional Experimental Standard Configurations for Aeroelastic Investigations in Turbomachine-Cascades. Report LTA-TM-83-2, Ecole Polytechnique Federale de Lausanne, Lausanne, Switzerland, September 1983.

[FV93] T. H. Fransson and J. M. Verdon. Standard Configurations for Unsteady Flow through Vibrating Axial-Flow Turbomachine Cascades. *Unsteady Aerodynamics, Aeroacoustics and Aeroelasticity of Turbomachines and Propellers*, pages 859–889, 1993. Springer-Verlag, New York, edited by H. M. Atassi.

[Gil88] M. B. Giles. Calculation of Unsteady Wake Rotor Interaction. *Journal of Propulsion and Power*, 4(4):356–362, July–August 1988.

[Gil90] M. B. Giles. Nonreflecting Boundary Conditions for Euler Equation Calculations. *AIAA Journal*, 28(12):2050–2058, December 1990.

[HC93] K. C. Hall and W. S. Clark. Linearized Euler Predictions of Unsteady Aerodynamic Loads in Cascades. *AIAA Journal*, 31(3):540–550, March 1993.

[He90] L. He. An Euler Solution for Unsteady Flows Around Oscillating Blades. *Transactions of the ASME: Journal of Turbomachinery*, 112(4):714–722, October 1990.

[HR89] D. L. Huff and T. S. R. Reddy. Numerical Analysis of Supersonic Flow Through Oscillating Cascade Sections by using a Deforming Grid. AIAA Paper 89-2805, 25th Joint Propulsion Conference, Monterey, California, July 10–12 1989.

[HSR91] D. L. Huff, T. W. Swafford, and T. S. R. Reddy. Euler Flow Predictions for an Oscillating Cascade Using a High Resolution Wave-Split Scheme. ASME Paper 91-GT-198, International Gas Turbine and Aeroengine Congress and Exposition, Orlando, Florida, June 3–6 1991.

[MM93] D. V. Murthy and M. R. Morel. Turbine Blade Forced Response Prediction using FREPS. Technical Paper 931373, SAE, April 20–23 1993. Presented at the SAE Aerospace Atlantic Conference & Exposition.

[MW92] S. R. Manwaring and D. C. Wisler. Unsteady Aerodynamics and Gust Response in Compressors and Turbines. Paper 92-GT-422, ASME, Cologne, Germany, 1992.

[OC84] S. Osher and S. Chakravarthy. Very High Order Accurate TVD Schemes. Report 84-44, ICASE, September 1984.

[Rai87] M. M. Rai. Navier-Stokes Simulations of Rotor-Stator Interaction using Patched and Overlaid Grids. *AIAA Journal of Propulsion and Power*, 3(5):387–396, September 1987.

[Rai89] M. M. Rai. Three-Dimensional Navier-Stokes Simulations of Turbine Rotor-Stator Interaction; Part 1 – Methodology, Part 2 – Results. *AIAA Journal of Propulsion and Power*, 5(3):305–319, May–June 1989.

[Roe81] P. L. Roe. Approximate Riemann Solvers, Parameter Vectors and Difference Schemes. *Journal of Computational Physics*, 43:357–372, 1981.

[Roe85] P. L. Roe. Some Contributions to the Modelling of Discontinuous Flows. In B. Engquist, S. Osher, and R. Somerville, editors, *Large-Scale Computations in Fluid Mechanics*, volume 22 of *Lectures in Applied Mathematics*, pages 163–193. 1985. Part 2.

[Sch60] H. Schlichting. *Boundary Layer Theory*, page 339. McGraw Hill Book Company, Inc., New York, 1960.

[Sid91] L. D. G. Siden. Numerical Simulation of Unsteady Viscous Compressible Flows Applied to Blade Flutter Analysis. ASME Paper 91-GT-203, International Gas Turbine and Aeroengine Congress and Exposition, Orlando, Florida, June 3–6 1991.

[SLH⁺94] T. W. Swafford, D. H. Loe, D. L. Huff, D. H. Huddleston, and T. S. R. Reddy. The Evolution of NPHASE: Euler/Navier-Stokes Computations of Unsteady Two-Dimensional Cascade Flow Fields. AIAA Paper 94-1834, 12th Applied Aerodynamics Conference, Colorado Springs, Colorado, June 20–23 1994.

[Smi90] T. E. Smith. Aerodynamic Stability of a High-Energy Turbine Blade. Paper 90-2351, AIAA/SAE/ASME/ASEE 26th Joint Propulsion Conference, Orlando, Florida, July 16–18 1990.

[SW81] J. L. Steger and R. F. Warming. Flux Vector Splitting of the Inviscid Gasdynamic Equations with Application to Finite Difference Methods. *Journal of Computational Physics*, 40(2):263–293, April 1981.

[Tho79] P. D. Thomas. Numerical Method for Predicting Flow Characteristics and Performance of Nonaxisymmetric Nozzles — Theory. CR 3147, NASA Langley Research Center, September 1979.

[UV91] W. J. Usab, Jr. and J. M. Verdon. Advances in the Numerical Analysis of Linearized Unsteady Cascade Flows. *Transactions of the ASME: Journal of Turbomachinery*, 113(4):633–643, October 1991.

[Ver89a] J. M. Verdon. The Unsteady Aerodynamic Response to Arbitrary Modes of Blade Motion. *Journal of Fluids and Structures*, 3(3):255–274, May 1989.

[Ver89b] J. M. Verdon. The Unsteady Flow in the Far Field of an Isolated Blade Row. *Journal of Fluids and Structures*, 3(2):123–149, March 1989.

[Ver92] J. M. Verdon. Linearized Unsteady Aerodynamics for Turbomachinery Aeroelastic Applications. *Journal de Physique III*, 2(4):481–506, April 1992. Also presented as Paper 90-2355, AIAA/SAE/ASME/ASEE 26th Joint Propulsion Conference, Orlando, Florida, July 16–18, 1990.

[Ver93] J. M. Verdon. Unsteady Aerodynamic Methods for Turbomachinery Aeroelastic and Aeroacoustic Applications. *AIAA Journal*, 31(2):235–250, February 1993.

[VL74] B. Van Leer. Towards the Ultimate Conservative Differencing Scheme, Part II. *Journal of Computational Physics*, 14(4):361–370, March 1974.

[Whi87] D. S. Whitehead. Classical Two-Dimensional Methods. In M. F. Platzer and F. O. Carta, editors, *AGARD Manual on Aeroelasticity in Axial-Flow Turbomachines*, chapter III. AGARD, March 1987. Vol. 1, *Unsteady Turbomachinery Aerodynamics*, AGARD-AG-298.

[Whi90] D. S. Whitehead. A Finite Element Solution of Unsteady Two-Dimensional Flow in Cascades. *International Journal for Numerical Methods in Fluids*, 10(1):13–34, January 1990.

[WJS88] D.L. Whitfield, J.M. Janus, and L.B. Simpson. Implicit Finite Volume High Resolution Wave Split Scheme for Solving the Unsteady Three-Dimensional Euler and Navier-Stokes Equations on Stationary or Dynamic Grids. Report MSSU-EIRS-ASE-88-2, Mississippi State Engineering and Industrial Research Station, 1988.

[WT91] D. L. Whitfield and L. Taylor. Discretized Newton-Relaxation Solution of High Resolution Flux-Difference Split Schemes. Paper 91-1539, AIAA 10th Computational Fluid Dynamics Conference, Honolulu, Hawaii, June 24–26 1991.

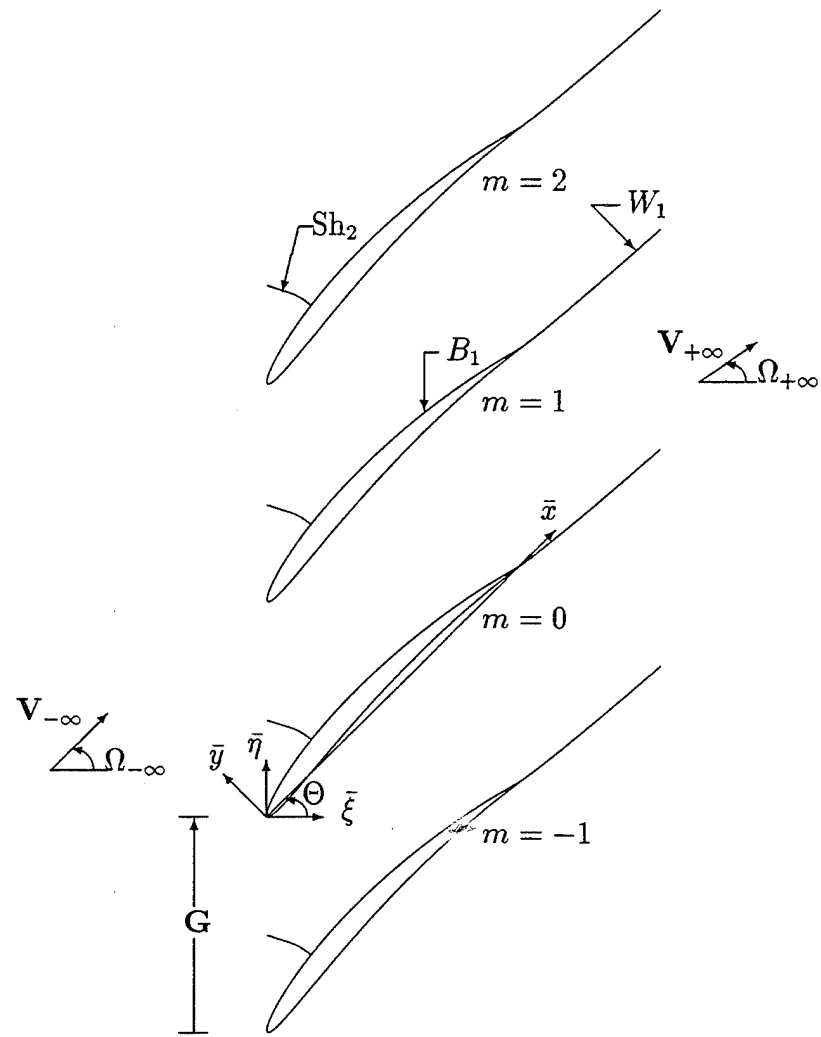


Figure 1: Two-dimensional transonic compressor cascade; $M_{+\infty} < M_{-\infty} < 1$.

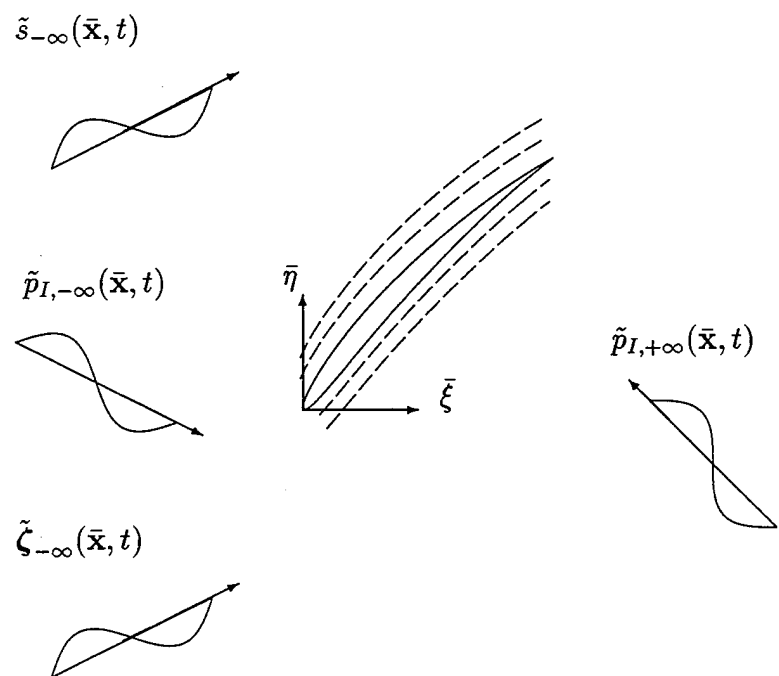


Figure 2: Unsteady excitations: blade motion, incident vortical and entropic disturbances from upstream, and incident acoustic disturbances from upstream and downstream.

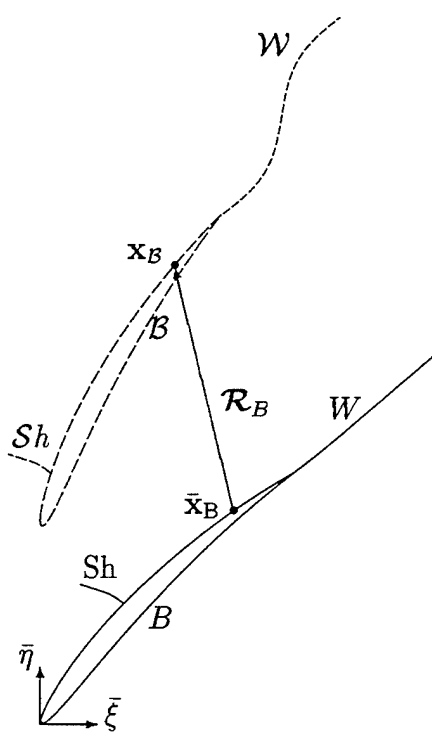


Figure 3: Steady state, —, and instantaneous, — — —, blade, wake and shock positions.

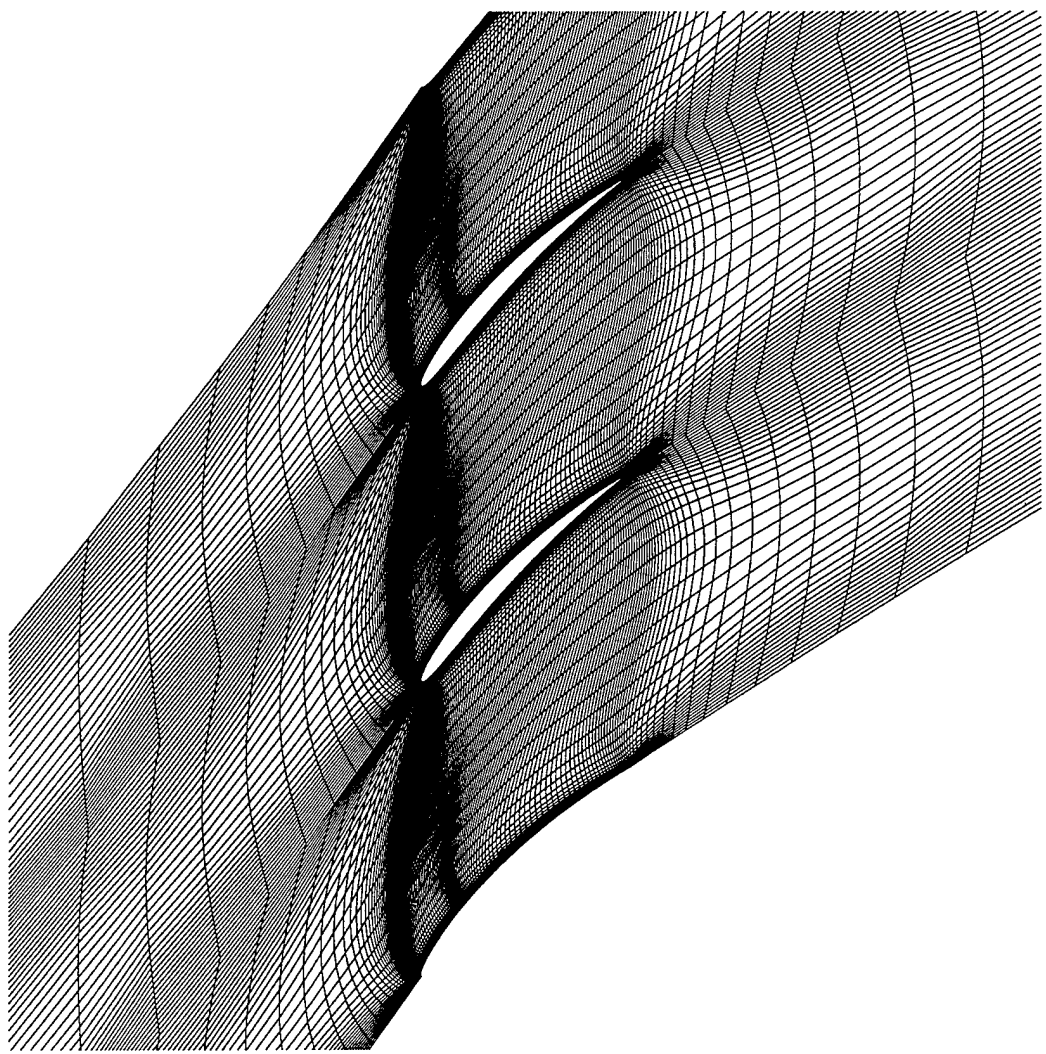


Figure 4: H-mesh used for the NPHASE, steady and unsteady, inviscid, transonic simulations.

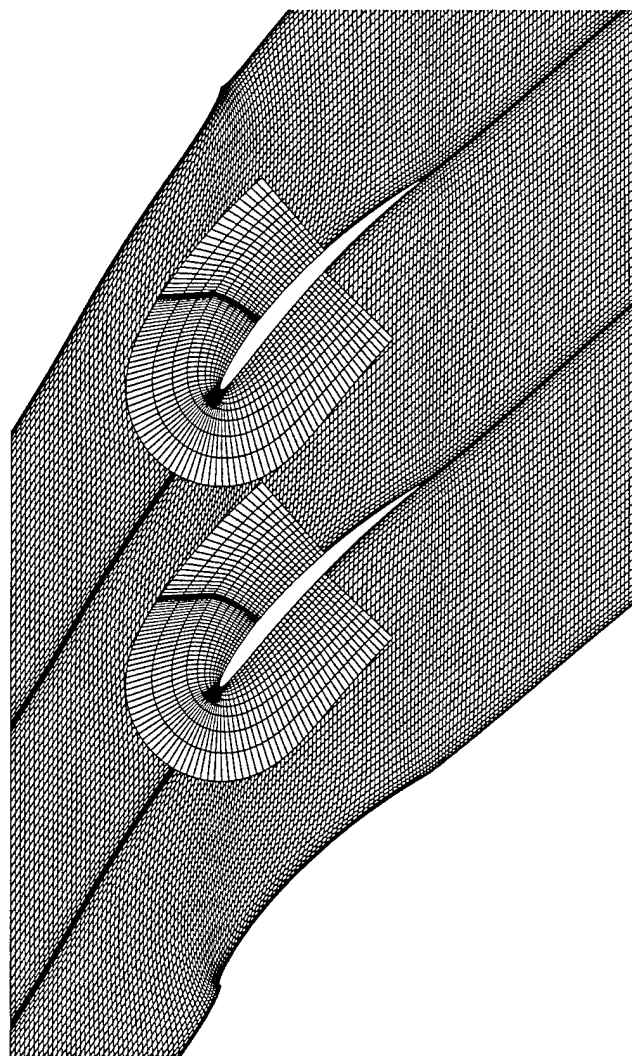


Figure 5: Composite H/C mesh used for the LINFL0 unsteady transonic calculations.

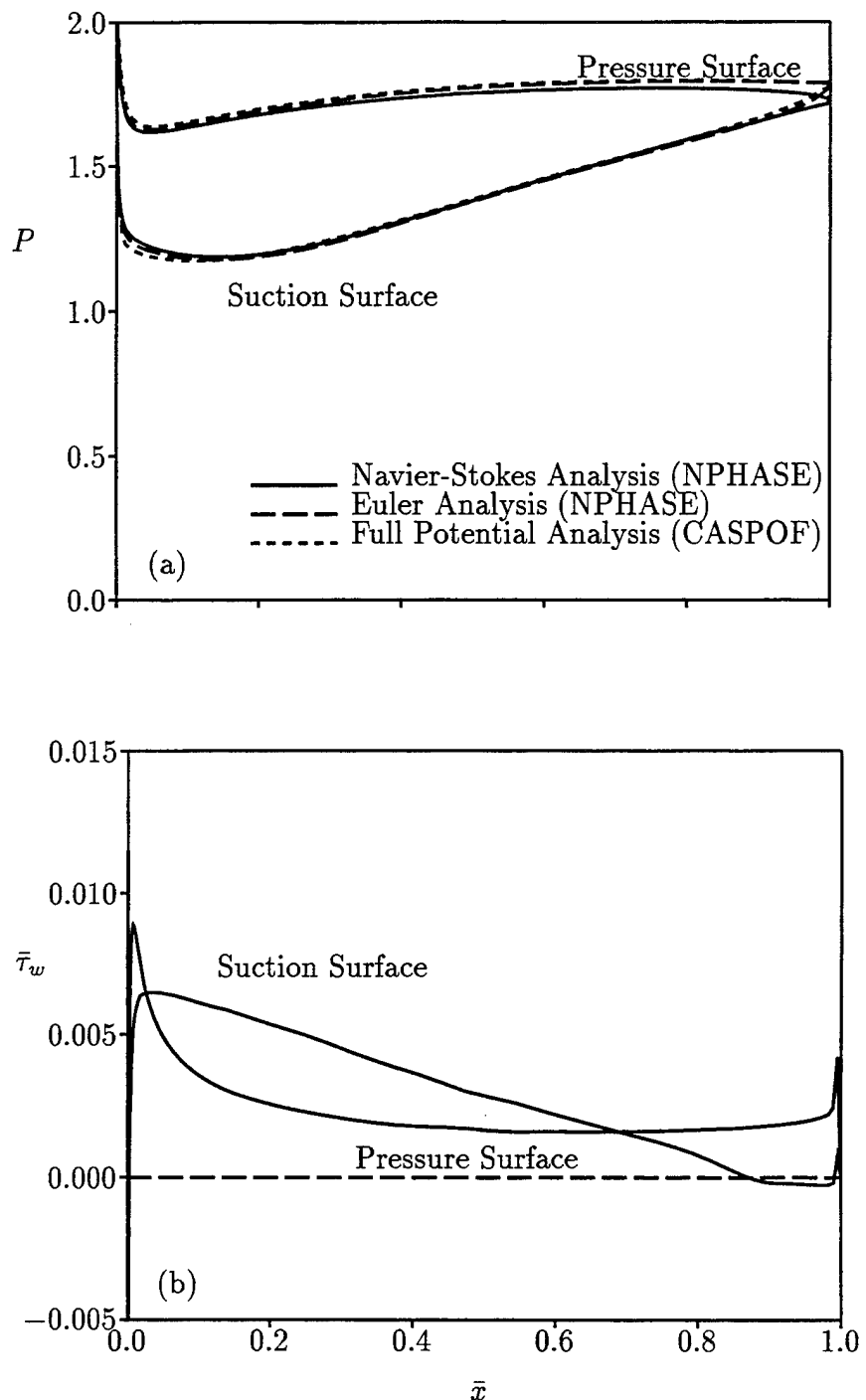


Figure 6: Predicted steady surface pressure (a) and skin friction (b) distributions for inviscid and viscid (at $Re = 10^6$) subsonic ($M_{\infty} = 0.7$, $\Omega_{\infty} = 55$ deg) flows through the 10th Standard Cascade.

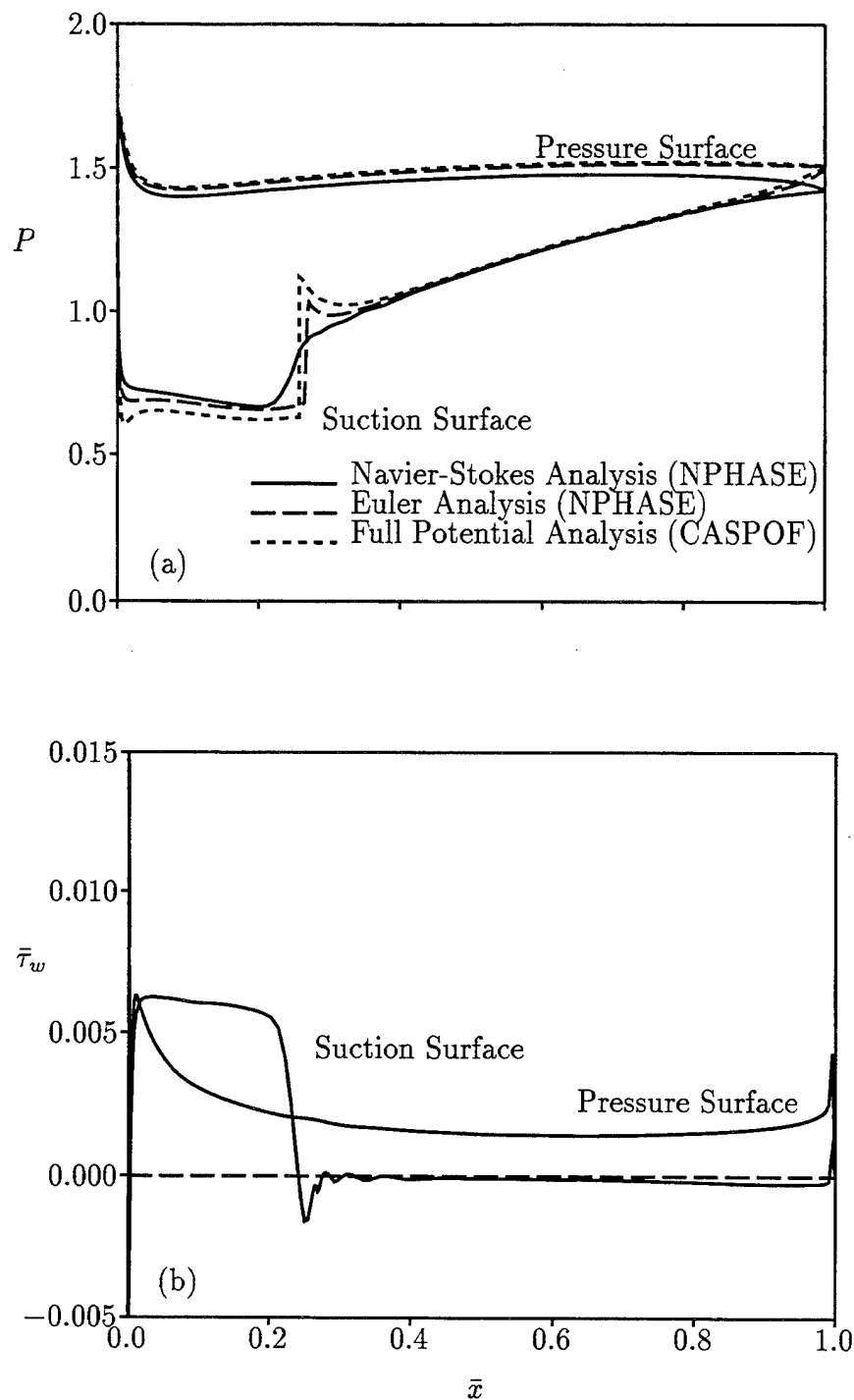


Figure 7: Predicted steady surface pressure (a) and skin friction (b) distributions for inviscid and viscid (at $Re = 10^6$) transonic ($M_{\infty} = 0.8$, $\Omega_{\infty} = 58$ deg) flows through the 10th Standard Cascade.

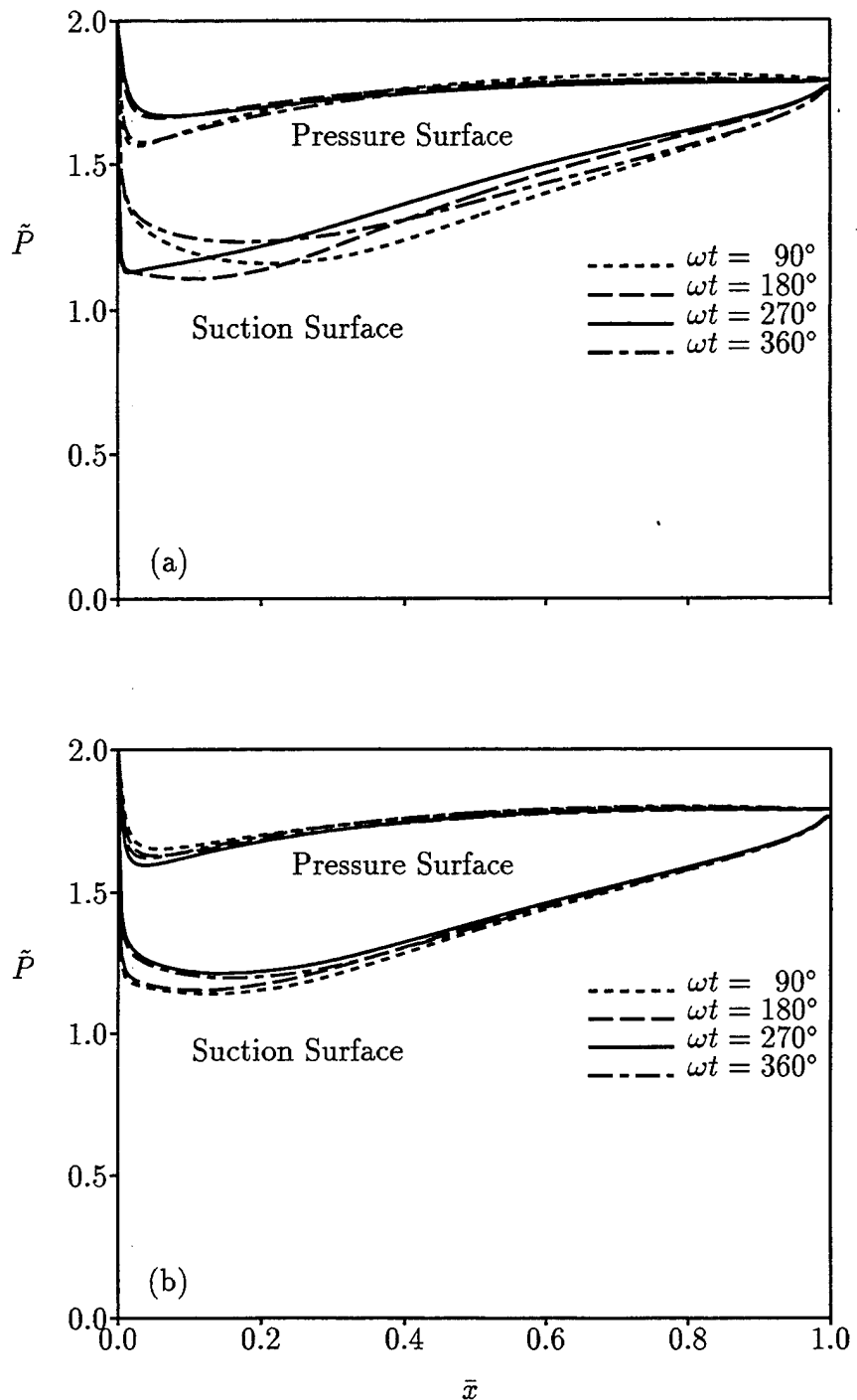


Figure 8: Instantaneous surface pressure distributions for inviscid flows through the subsonic ($M_\infty = 0.7$, $\Omega_\infty = 55$ deg) 10th Standard Cascade undergoing prescribed blade vibrations: (a) in-phase torsional vibration about midchord at $|\alpha| = 2$ deg, $\omega = 1$, and $\sigma = 0$ deg; (b) out-of-phase bending vibration at $|h_y| = 0.01$, $\omega = 1$, $\sigma = 180$ deg.

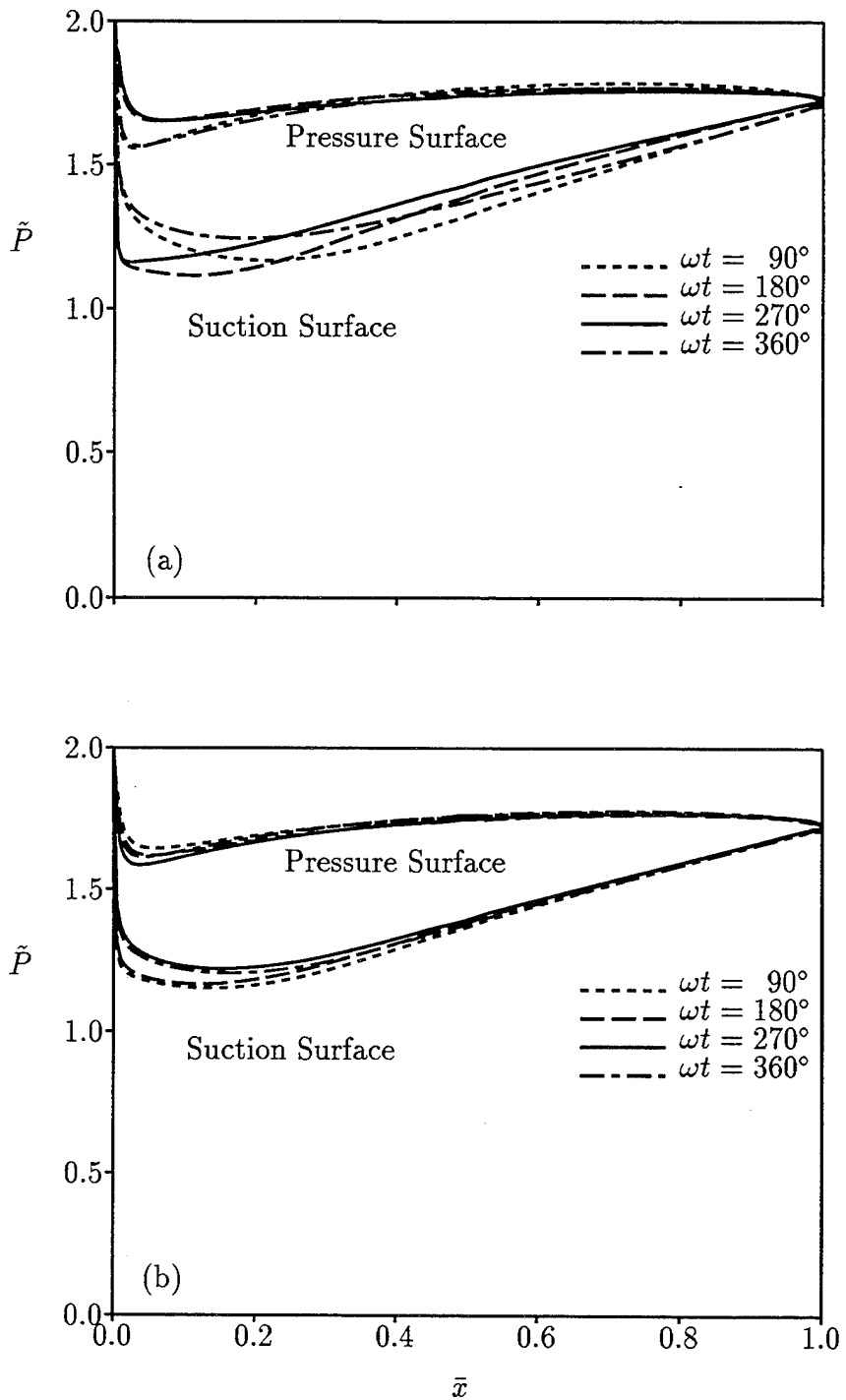


Figure 9: Instantaneous surface pressure distributions for viscous flows at $Re = 10^6$ through the subsonic ($M_{\infty} = 0.7$, $\Omega_{\infty} = 55$ deg) 10th Standard Cascade undergoing prescribed blade vibrations: (a) in-phase torsional vibration about midchord at $|\alpha| = 2$ deg, $\omega = 1$, and $\sigma = 0$ deg; (b) out-of-phase bending vibration at $|h_y| = 0.01$, $\omega = 1$, $\sigma = 180$ deg.

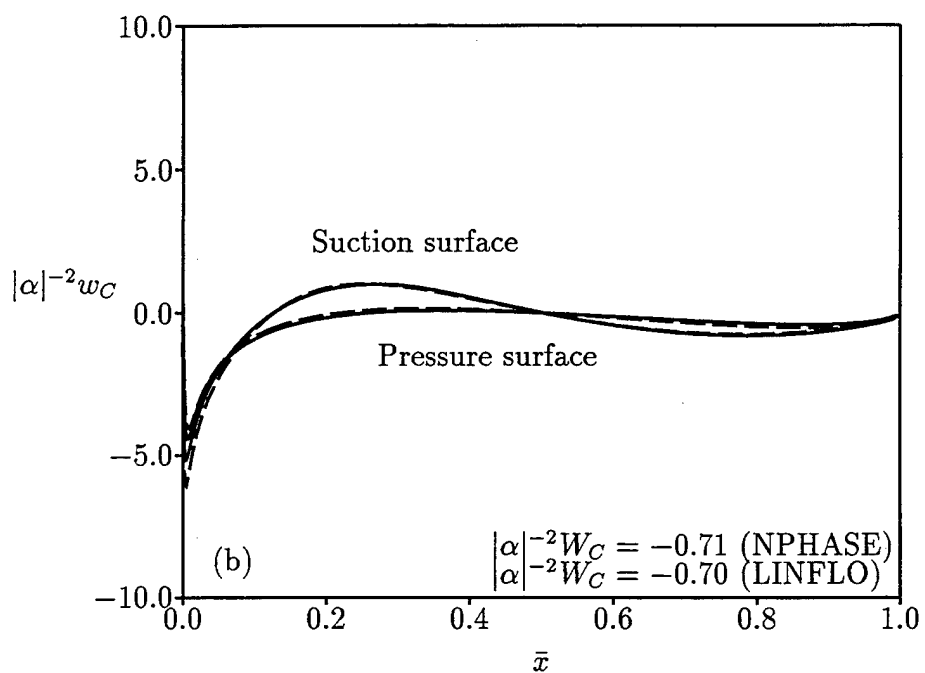
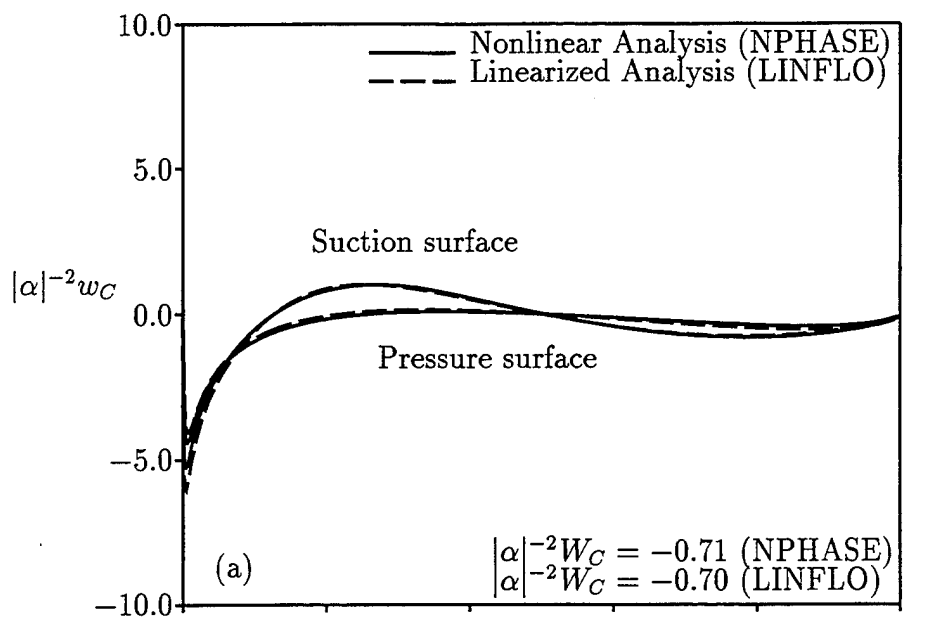


Figure 10: Pressure-displacement function distributions for inviscid subsonic flow ($M_{\infty} = 0.7$, $\Omega_{\infty} = 55$ deg) through the 10th Standard Cascade undergoing an in-phase torsional vibration about midchord at $|\alpha| = 2$ deg, $\omega = 1$, and $\sigma = 0$ deg: (a) NPHASE nonlinear prediction; (b) NPHASE first-harmonic prediction.

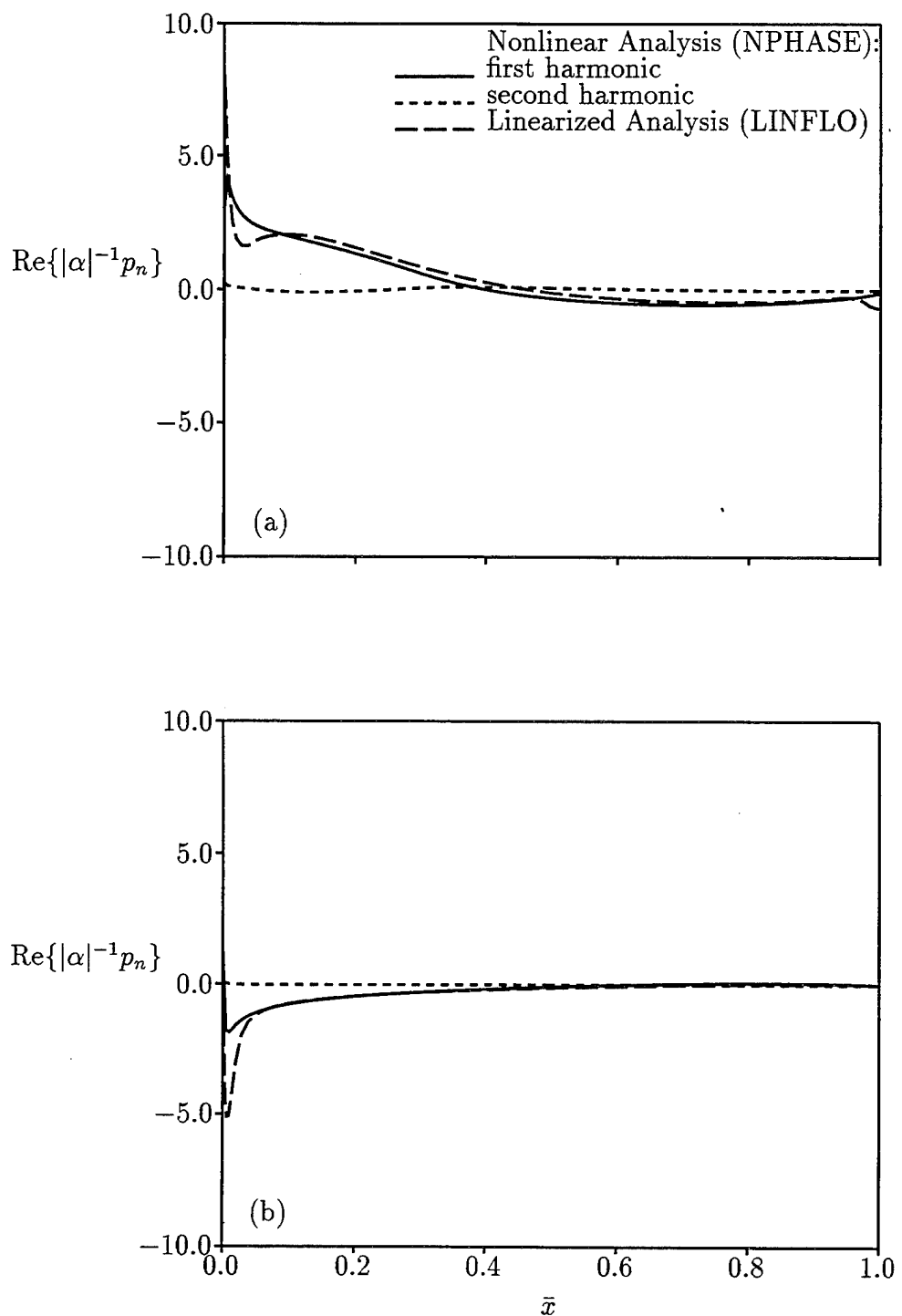


Figure 11: Real components of the Fourier amplitudes of the unsteady surface pressure distribution for inviscid subsonic ($M_{\infty} = 0.7$, $\Omega_{\infty} = 55$ deg) flow through the 10th Standard Cascade undergoing an in-phase torsional vibration about midchord at $|\alpha| = 2$ deg, $\omega = 1$, and $\sigma = 0$ deg: (a) Suction surface; (b) Pressure surface.

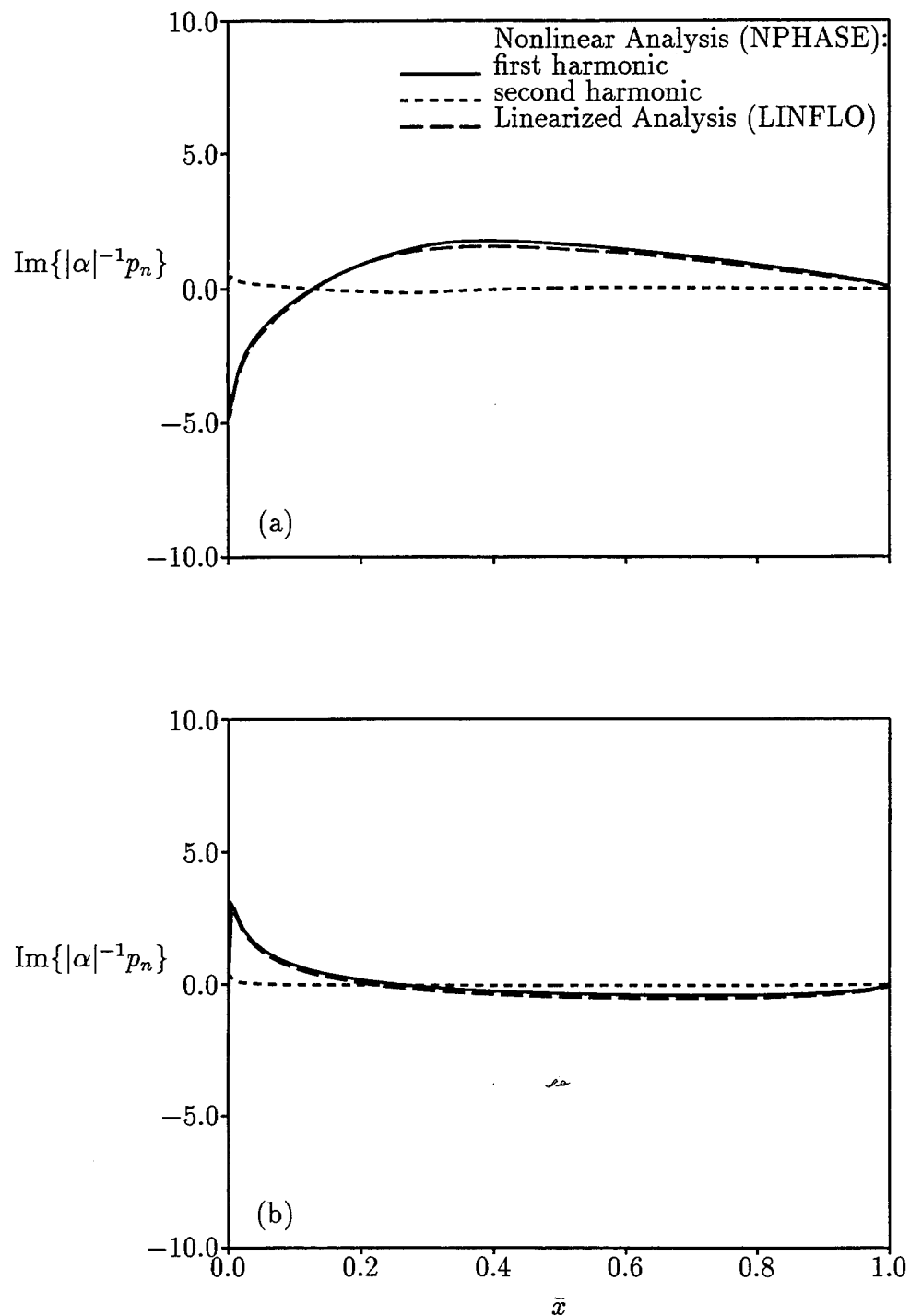


Figure 12: Imaginary components of the Fourier amplitudes of the unsteady surface pressure distribution for inviscid subsonic ($M_{\infty} = 0.7$, $\Omega_{\infty} = 55$ deg) flow through the 10th Standard Cascade undergoing an in-phase torsional vibration about midchord at $|\alpha| = 2$ deg, $\omega = 1$, and $\sigma = 0$ deg: (a) Suction surface; (b) Pressure surface.

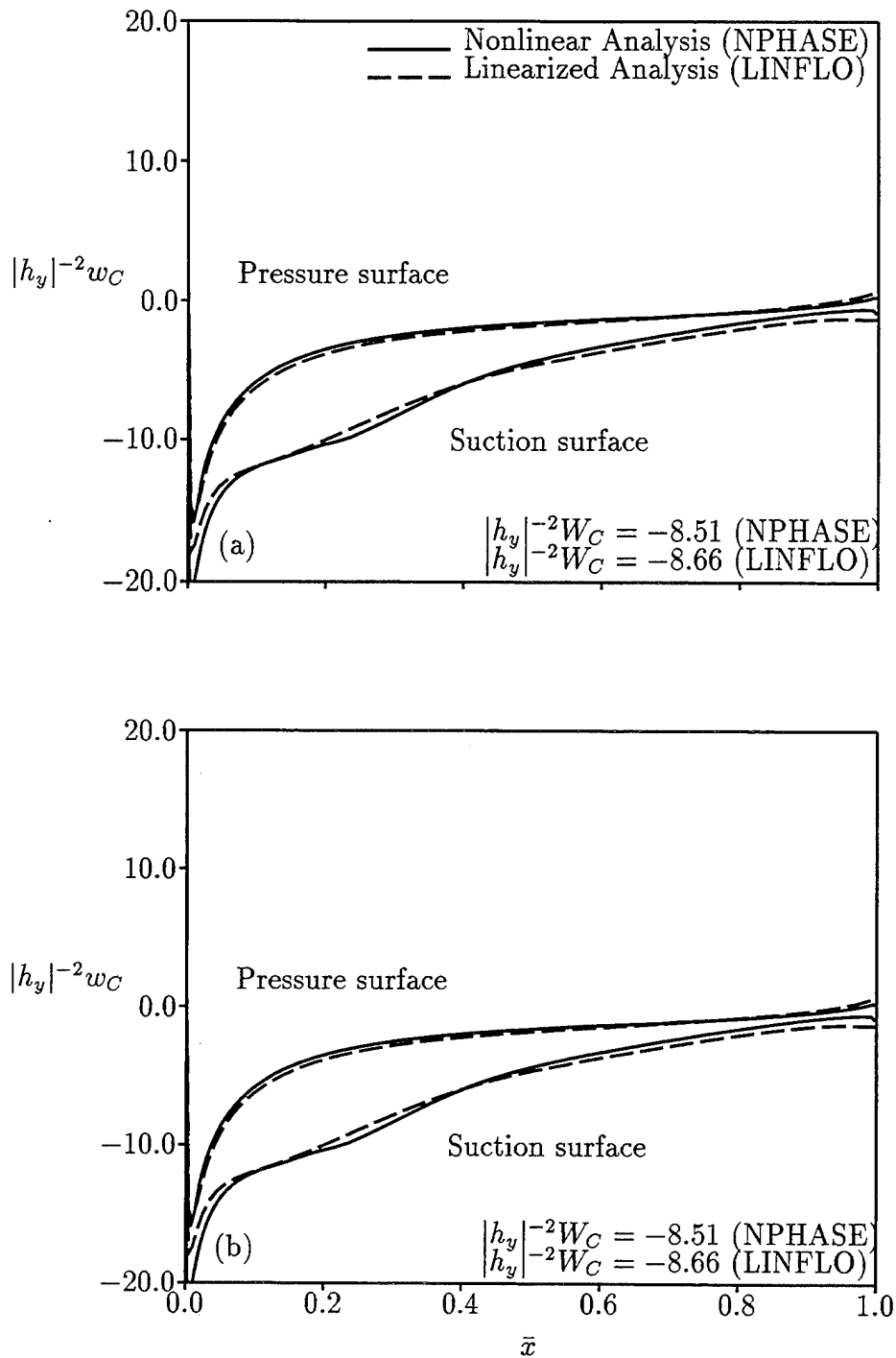


Figure 13: Pressure-displacement function distribution for inviscid subsonic ($M_{\infty} = 0.7$, $\Omega_{\infty} = 55$ deg) flow through the 10th Standard Cascade undergoing an out-of-phase bending vibration at $|h_y| = 0.01$, $\omega = 1$, and $\sigma = 180$ deg: (a) NPHASE nonlinear prediction; (b) NPHASE first-harmonic prediction.

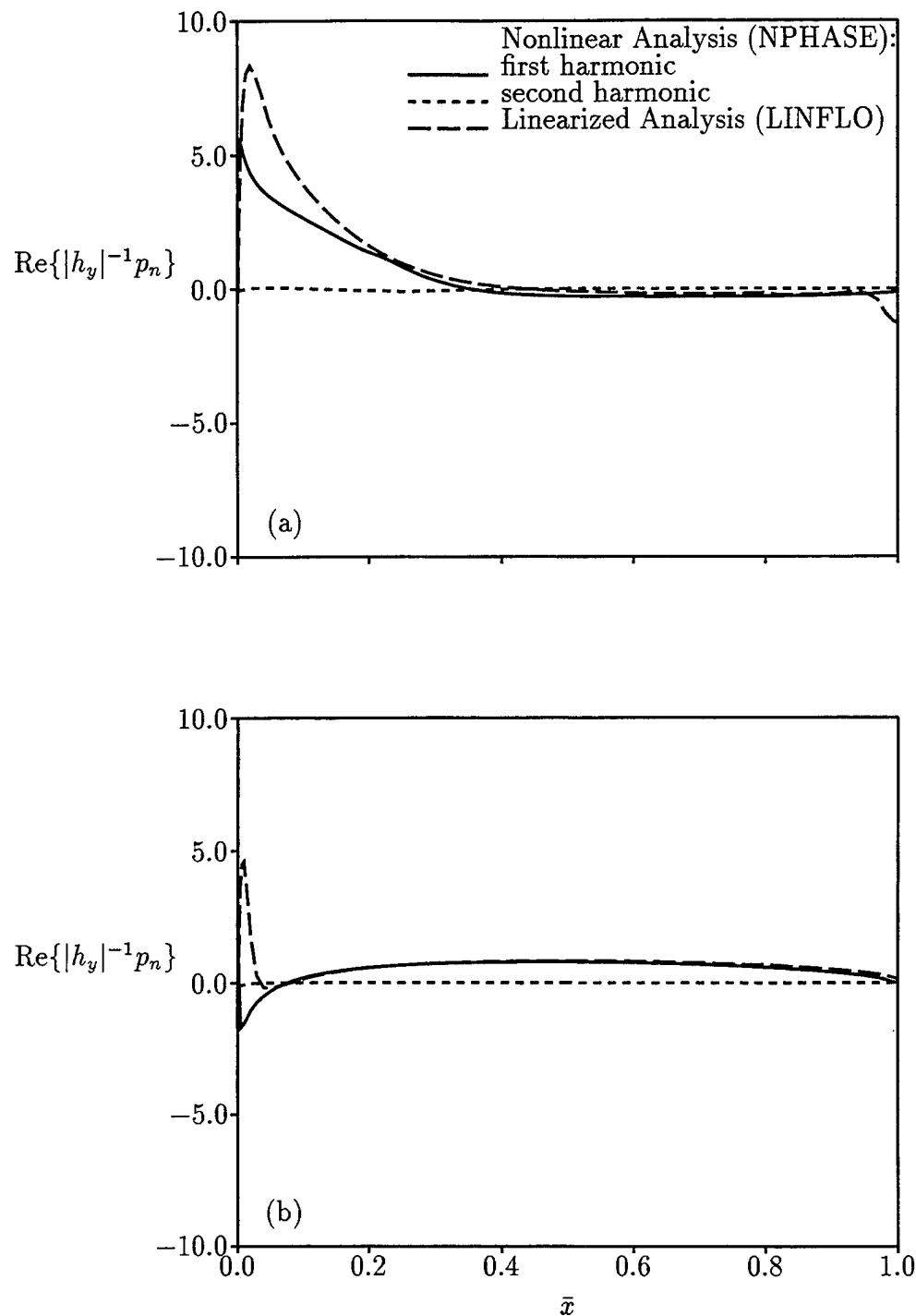


Figure 14: Real components of the Fourier amplitudes of the unsteady surface pressure distribution for inviscid subsonic ($M_{\infty} = 0.7$, $\Omega_{\infty} = 55$ deg) flow through the 10th Standard Cascade undergoing an out-of-phase bending vibration at $|h_y| = 0.01$, $\omega = 1$, and $\sigma = 180$ deg: (a) Suction surface; (b) Pressure surface.

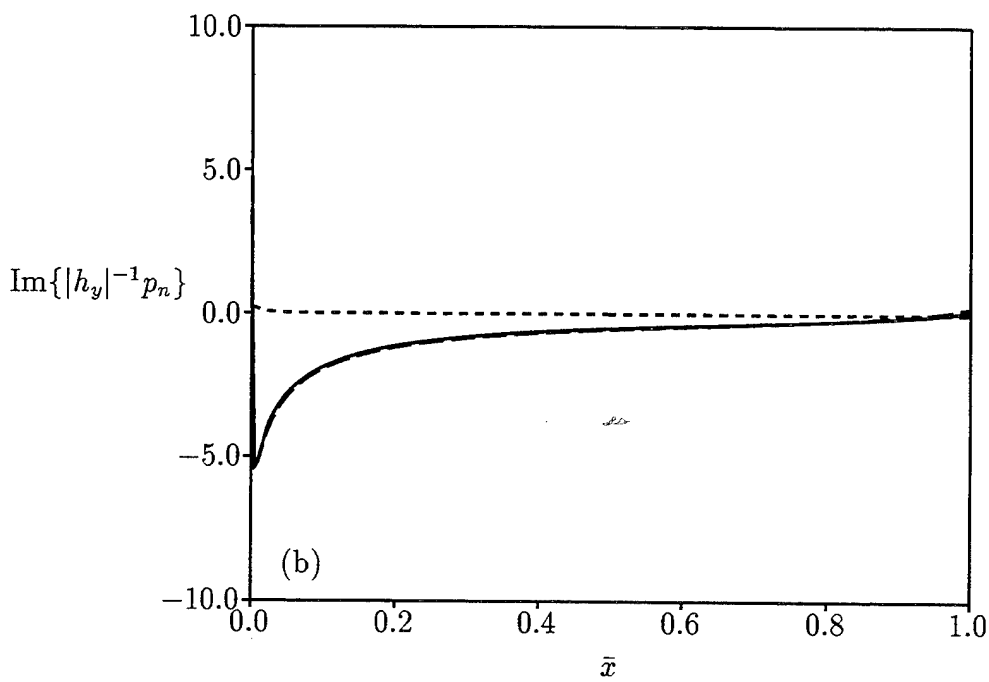
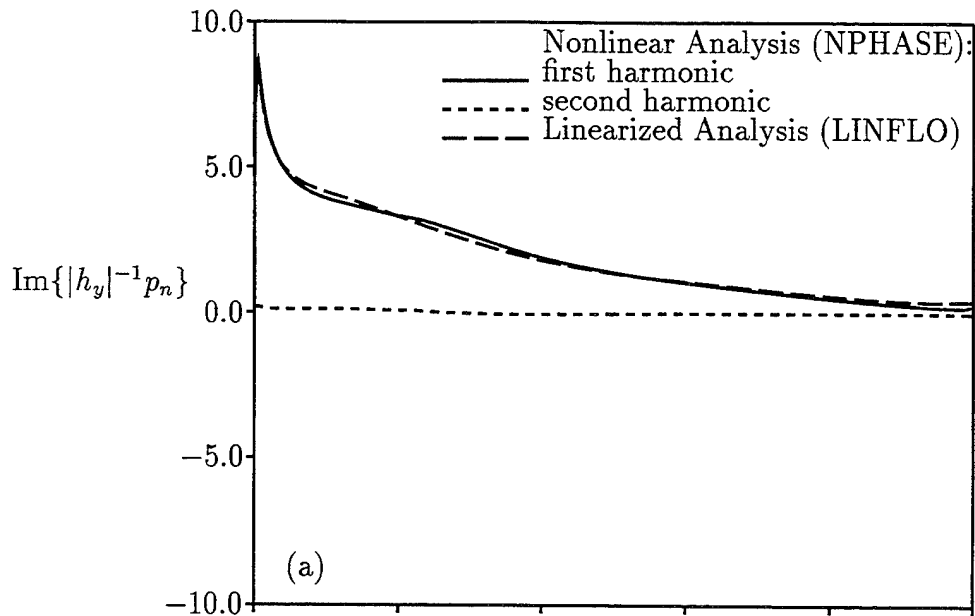


Figure 15: Imaginary components of the Fourier amplitudes of the unsteady surface pressure distribution for inviscid subsonic ($M_{\infty} = 0.7$, $\Omega_{\infty} = 55$ deg) flow through the 10th Standard Cascade undergoing an out-of-phase bending vibration at $|h_y| = 0.01$, $\omega = 1$, and $\sigma = 180$ deg: (a) Suction surface; (b) Pressure surface.

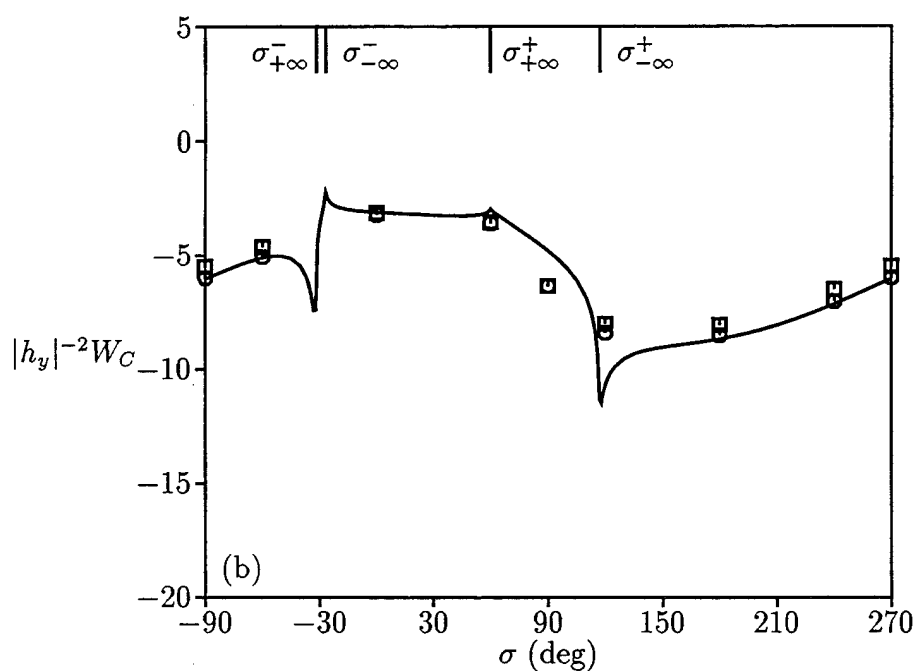
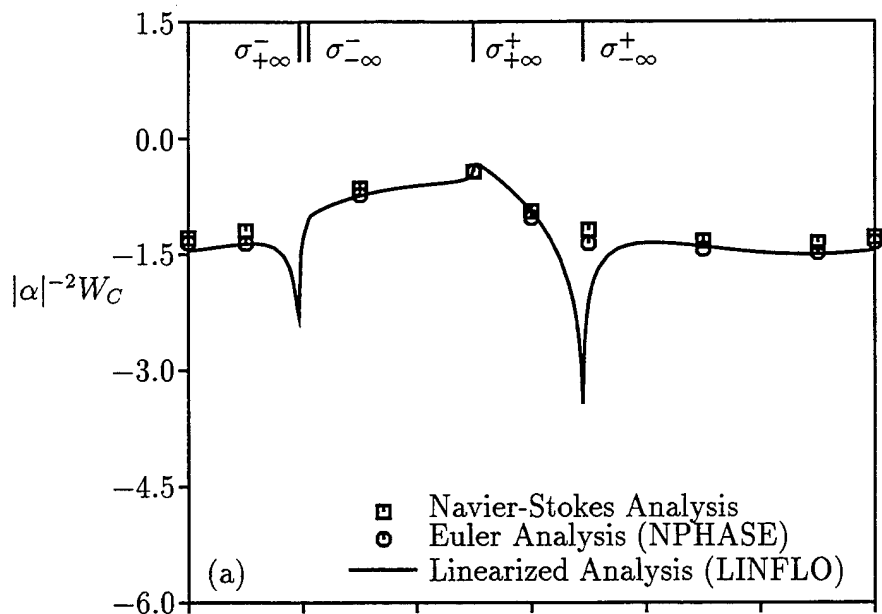


Figure 16: Work per cycle versus interblade phase angle for inviscid and viscous (at $Re = 10^6$) subsonic flows through the 10th Standard Cascade undergoing prescribed blade motions at unit frequency ($\omega = 1$): (a) torsional vibrations at $|\alpha| = 2$ deg about midchord; (b) bending vibrations at $|h_y| = 0.01$.

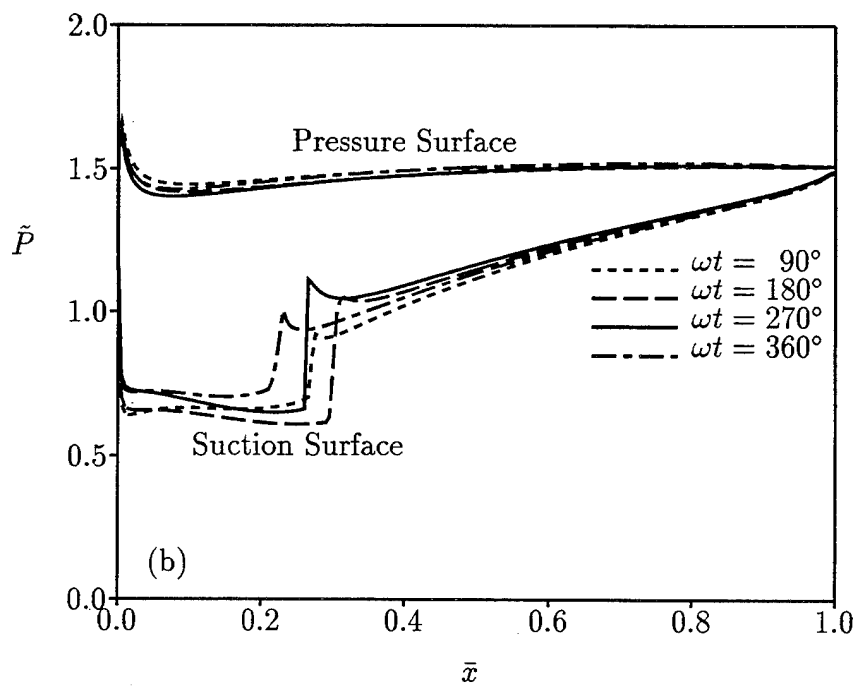
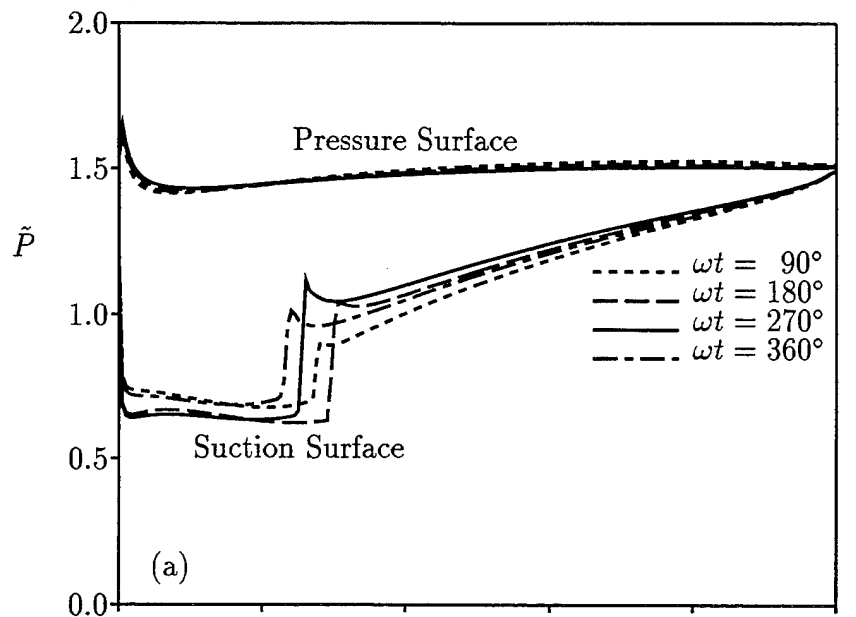


Figure 17: Instantaneous surface pressure distributions for inviscid flows through the transonic ($M_{\infty} = 0.8$, $\Omega_{\infty} = 58$ deg) 10th Standard Cascade undergoing prescribed blade vibrations: (a) in-phase torsional vibration about midchord at $|\alpha| = 1$ deg, $\omega = 1$, and $\sigma = 0$ deg; (b) out-of-phase bending vibration at $|h_y| = 0.01$, $\omega = 1$, $\sigma = 180$ deg.

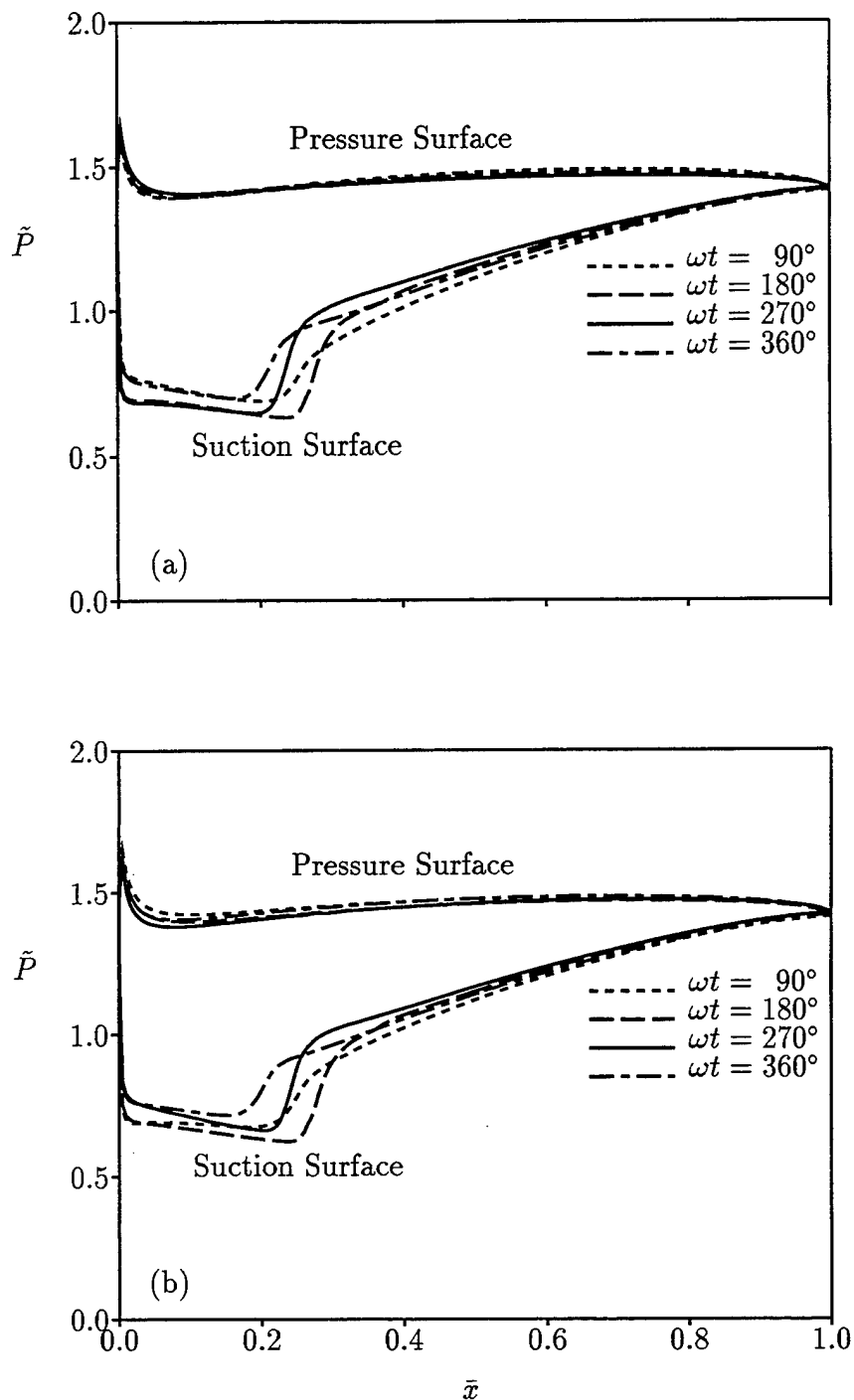


Figure 18: Instantaneous surface pressure distributions for viscous flows (at $Re = 10^6$) through the transonic ($M_{\infty} = 0.8$, $\Omega_{\infty} = 58$ deg) 10th Standard Cascade undergoing prescribed blade vibrations: (a) in-phase torsional vibration about midchord at $|\alpha| = 1$ deg, $\omega = 1$, and $\sigma = 0$ deg; (b) out-of-phase bending vibration at $|h_y| = 0.01$, $\omega = 1$, $\sigma = 180$ deg.

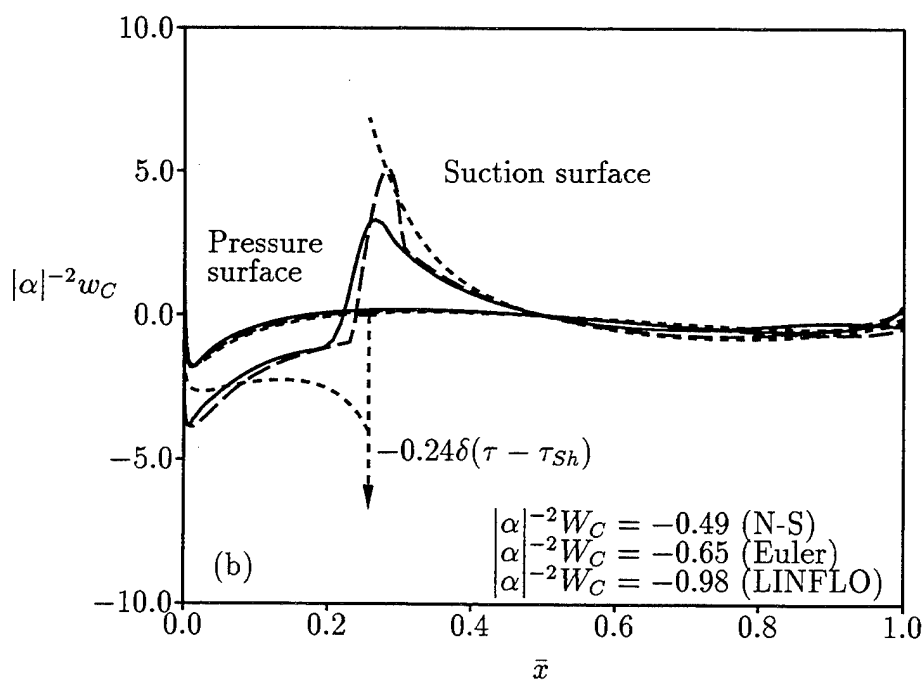
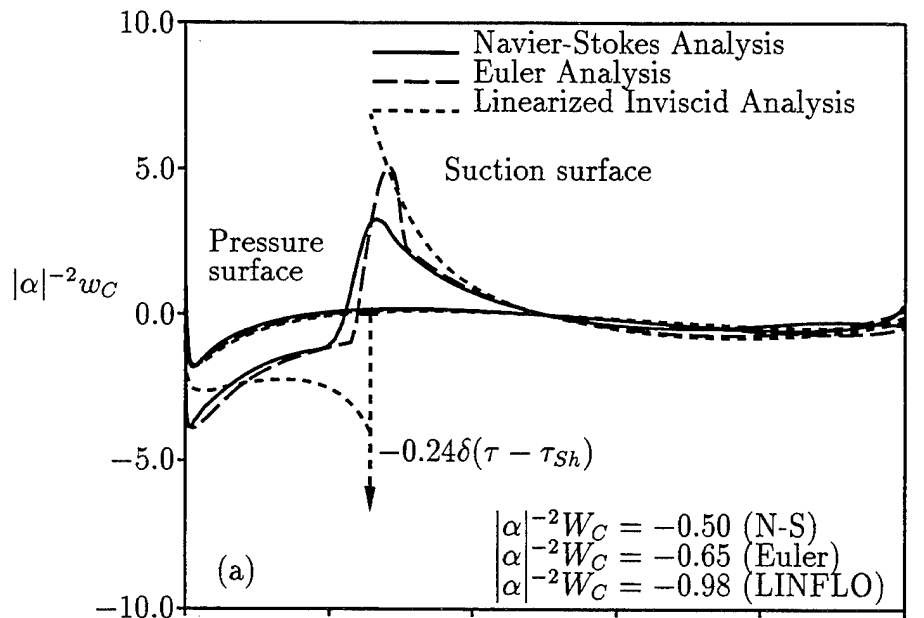


Figure 19: Pressure-displacement function distribution for viscous (at $Re = 10^6$) and inviscid transonic flows ($M_{\infty} = 0.8$, $\Omega_{\infty} = 58$ deg) through the 10th Standard Cascade undergoing an in-phase torsional vibration about midchord at $|\alpha| = 1$ deg, $\omega = 1$, and $\sigma = 0$ deg: (a) NPHASE nonlinear predictions; (b) NPHASE first-harmonic predictions.

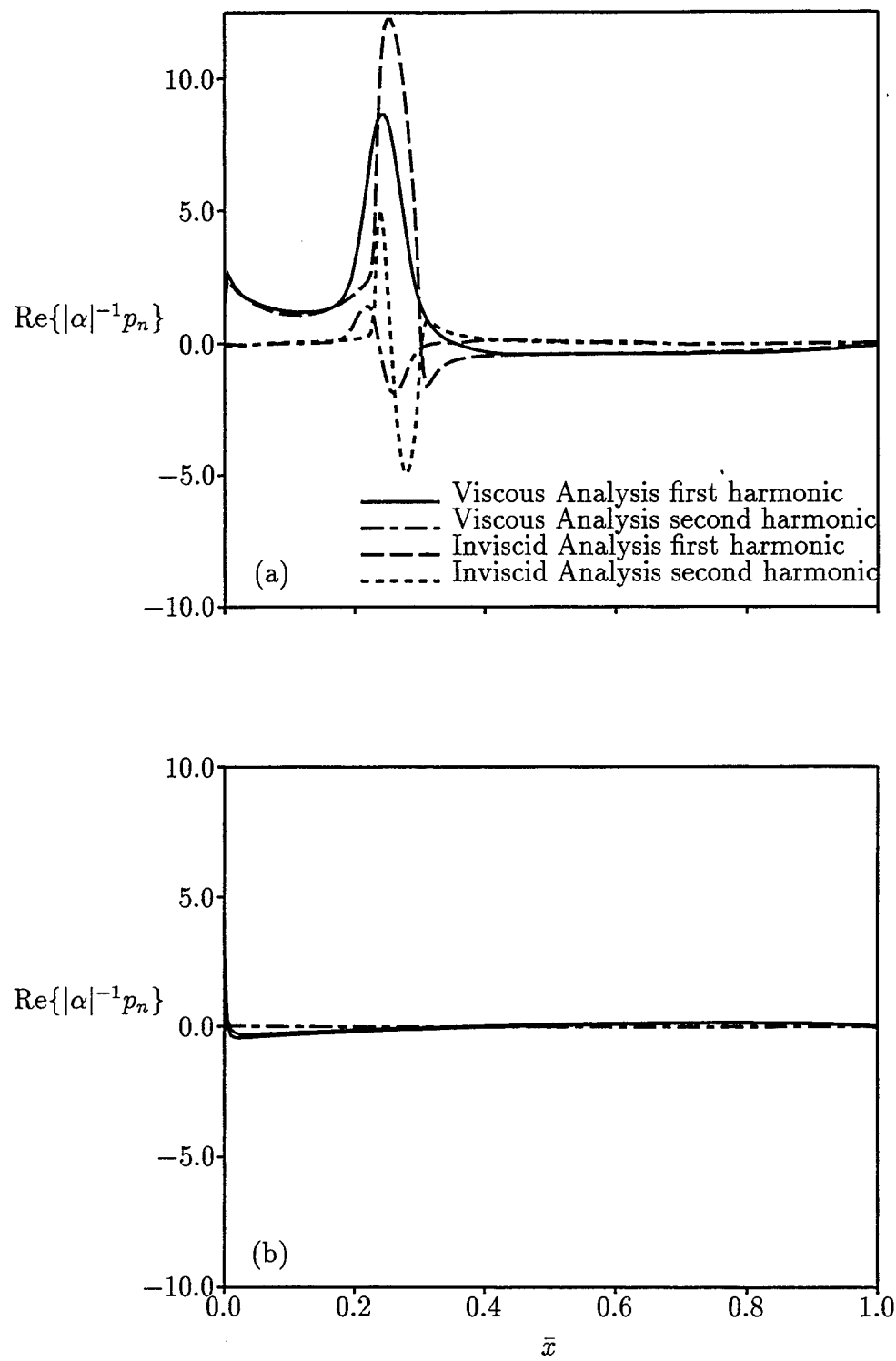
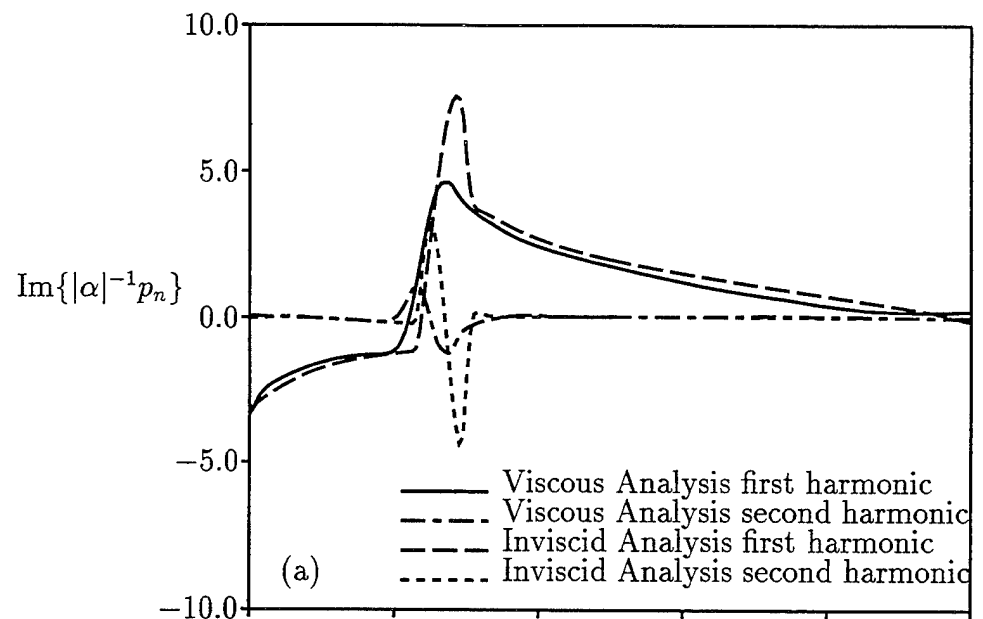
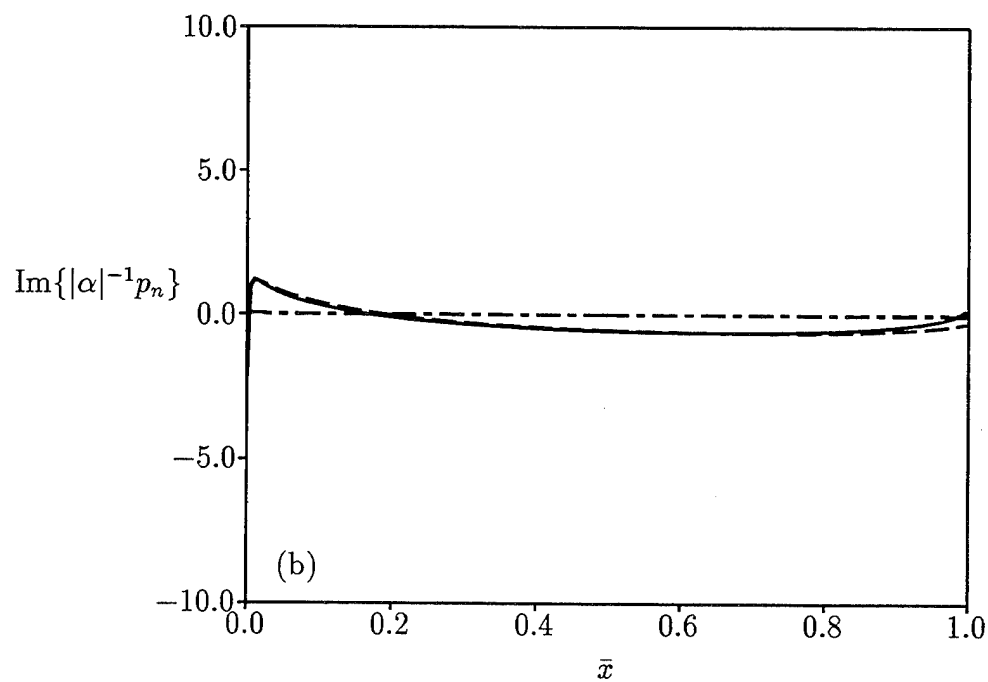


Figure 20: Real components of the Fourier amplitudes of the unsteady surface pressure distribution for viscous (at $Re = 10^6$) and inviscid transonic ($M_{\infty} = 0.8$, $\Omega_{\infty} = 58$ deg) flows through the 10th Standard Cascade undergoing an in-phase torsional vibration about midchord at $|\alpha| = 1$ deg, $\omega = 1$, and $\sigma = 0$ deg: (a) Suction surface; (b) Pressure surface.



(a)



(b)

Figure 21: Imaginary components of the Fourier amplitudes of the unsteady surface pressure distribution for viscous (at $Re = 10^6$) and inviscid transonic ($M_{\infty} = 0.8$, $\Omega_{\infty} = 58$ deg) flows through the 10th Standard Cascade undergoing an in-phase torsional vibration about midchord at $|\alpha| = 1$ deg, $\omega = 1$, and $\sigma = 0$ deg: (a) Suction surface; (b) Pressure surface.

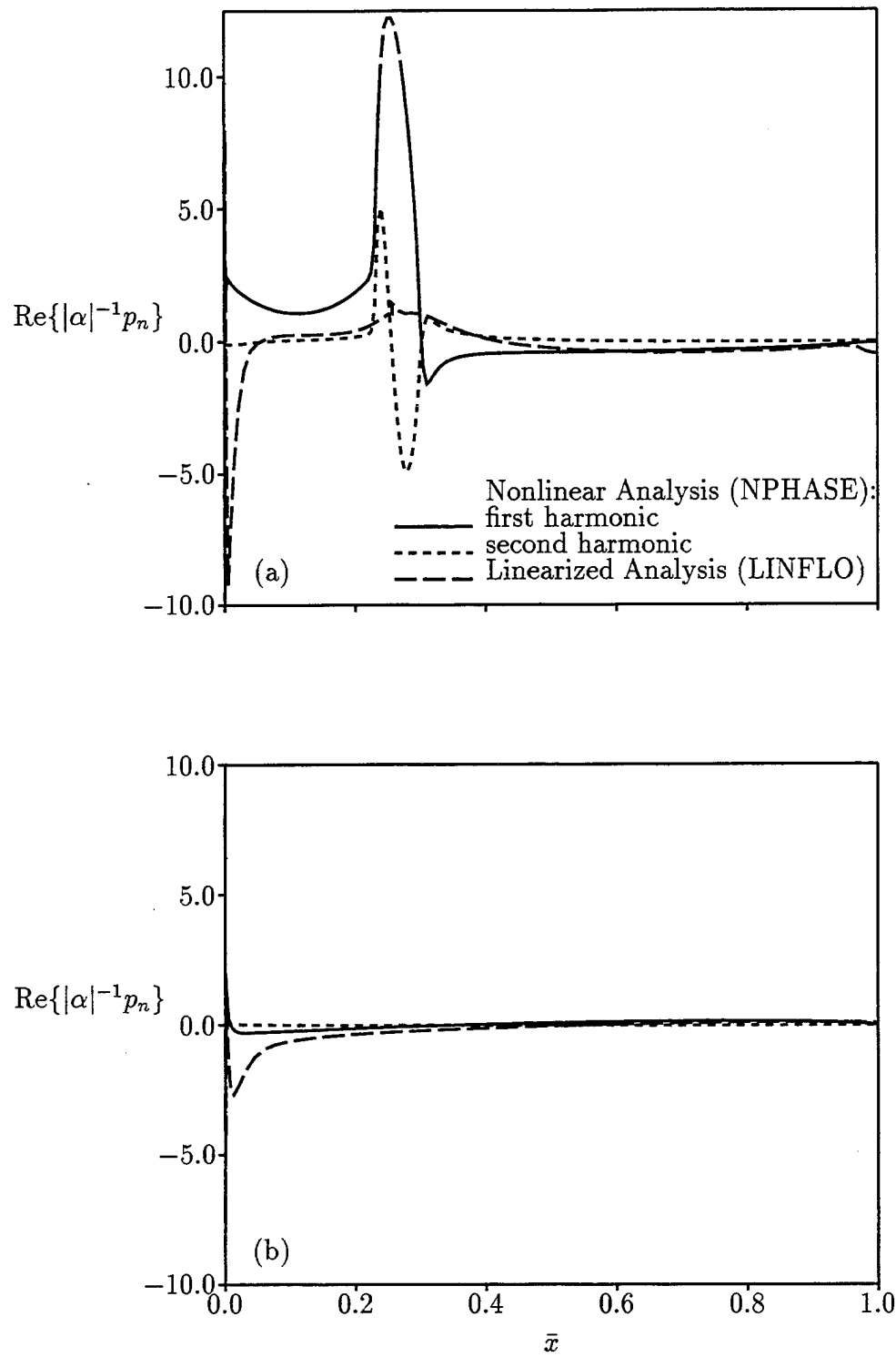


Figure 22: Real components of the Fourier amplitudes of the unsteady surface pressure distribution for inviscid transonic ($M_{\infty} = 0.8$, $\Omega_{\infty} = 58$ deg) flow through the 10th Standard Cascade undergoing an in-phase torsional vibration about midchord at $|\alpha| = 1$ deg, $\omega = 1$, and $\sigma = 0$ deg: (a) Suction surface; (b) Pressure surface.

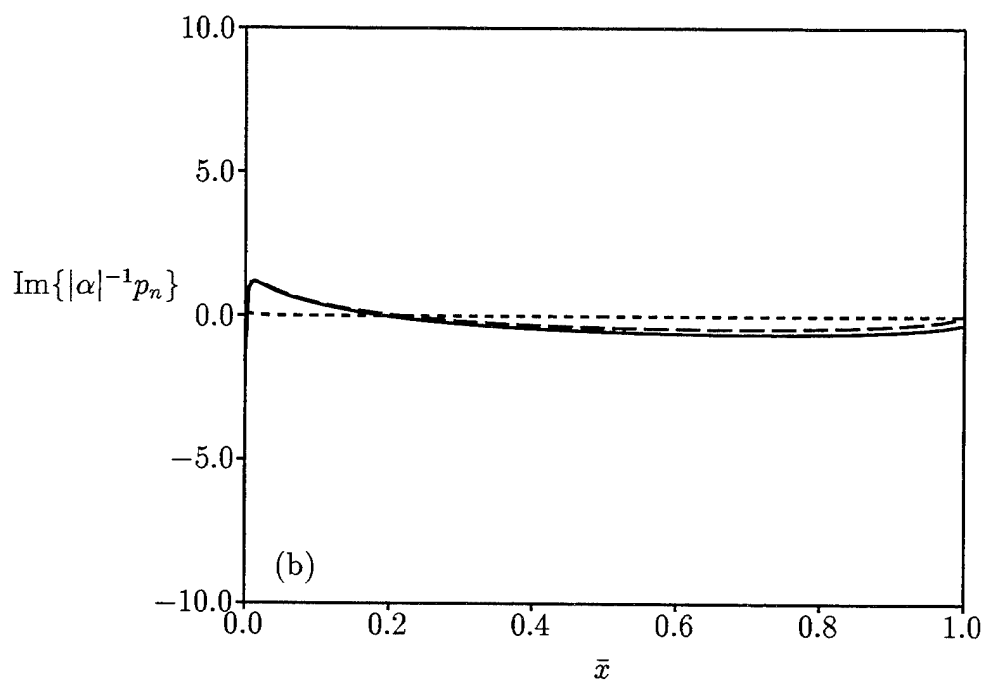
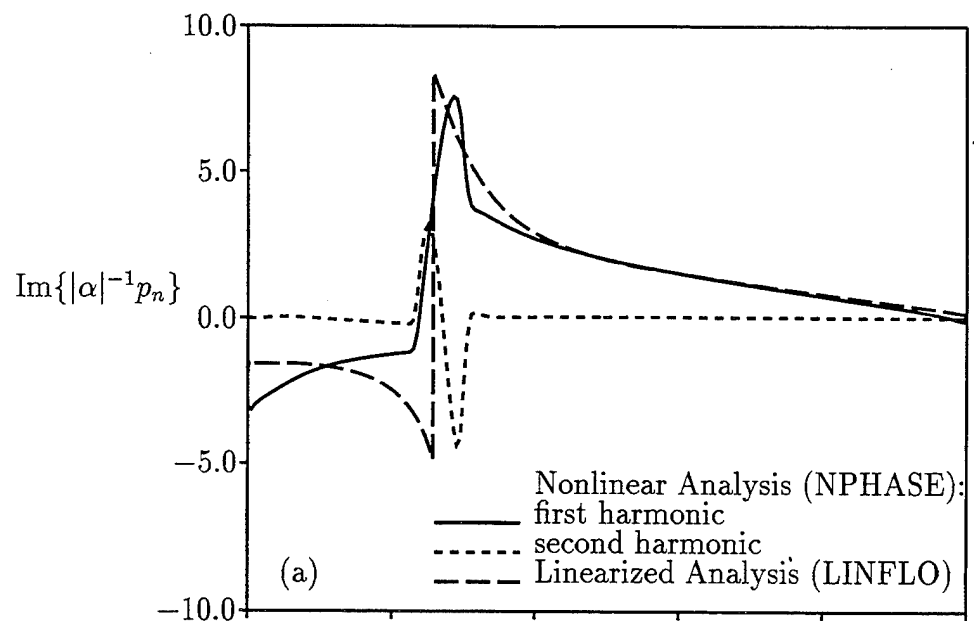


Figure 23: Imaginary components of the Fourier amplitudes of the unsteady surface pressure distribution for inviscid transonic ($M_{\infty} = 0.8$, $\Omega_{\infty} = 58$ deg) flow through the 10th Standard Cascade undergoing an in-phase torsional vibration about midchord at $|\alpha| = 1$ deg, $\omega = 1$, and $\sigma = 0$ deg: (a) Suction surface; (b) Pressure surface.

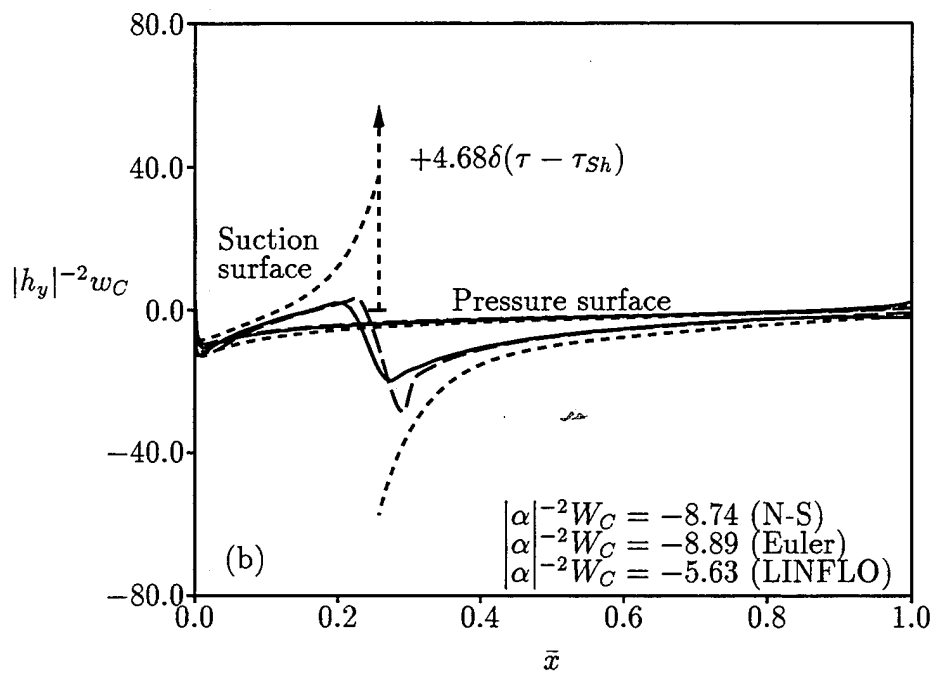
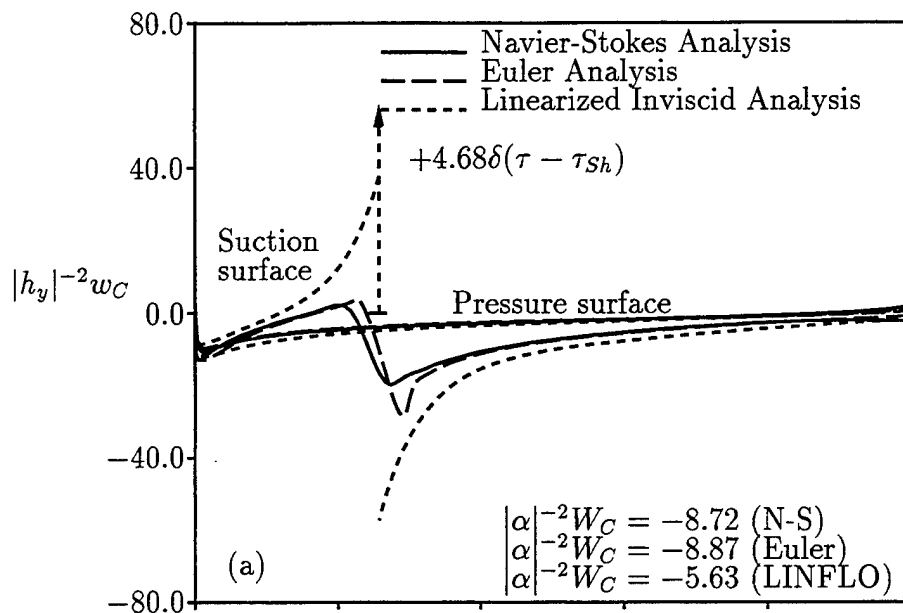


Figure 24: Pressure-displacement function distribution for viscous (at $Re = 10^6$) and inviscid transonic ($M_{\infty} = 0.8$, $\Omega_{\infty} = 58$ deg) flows through the 10th Standard Cascade undergoing an out-of-phase bending vibration at $|h_y| = 0.01$, $\omega = 1$, and $\sigma = 180$ deg: (a) NPHASE nonlinear predictions; (b) NPHASE first-harmonic predictions.

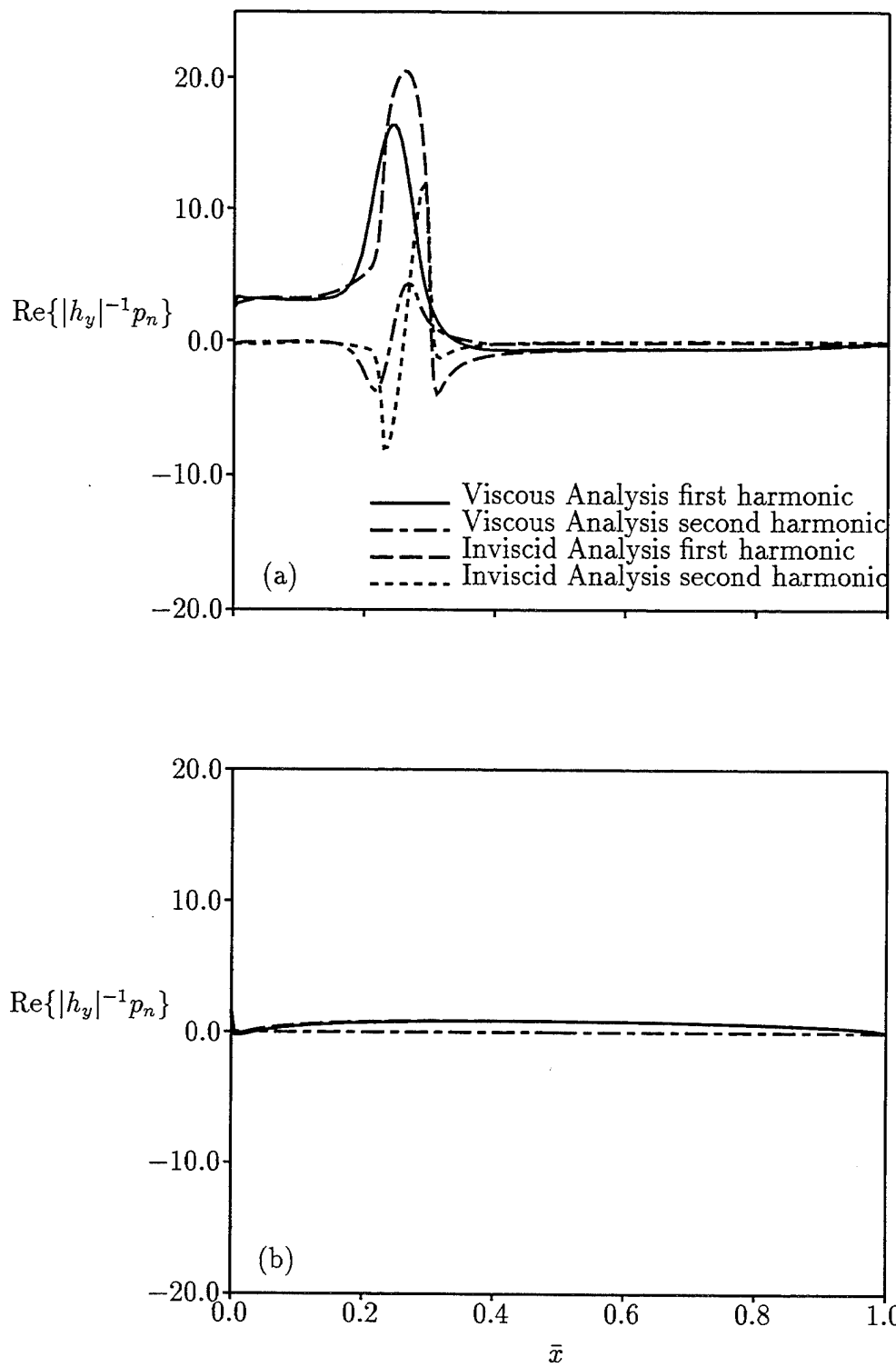


Figure 25: Real components of the Fourier amplitudes of the unsteady surface pressure distribution for viscous (at $Re = 10^6$) and inviscid transonic ($M_{\infty} = 0.8$, $\Omega_{\infty} = 58$ deg) flows through the 10th Standard Cascade undergoing an out-of-phase bending vibration at $|h_y| = 0.01$, $\omega = 1$, and $\sigma = 180$ deg: (a) Suction surface; (b) Pressure surface.

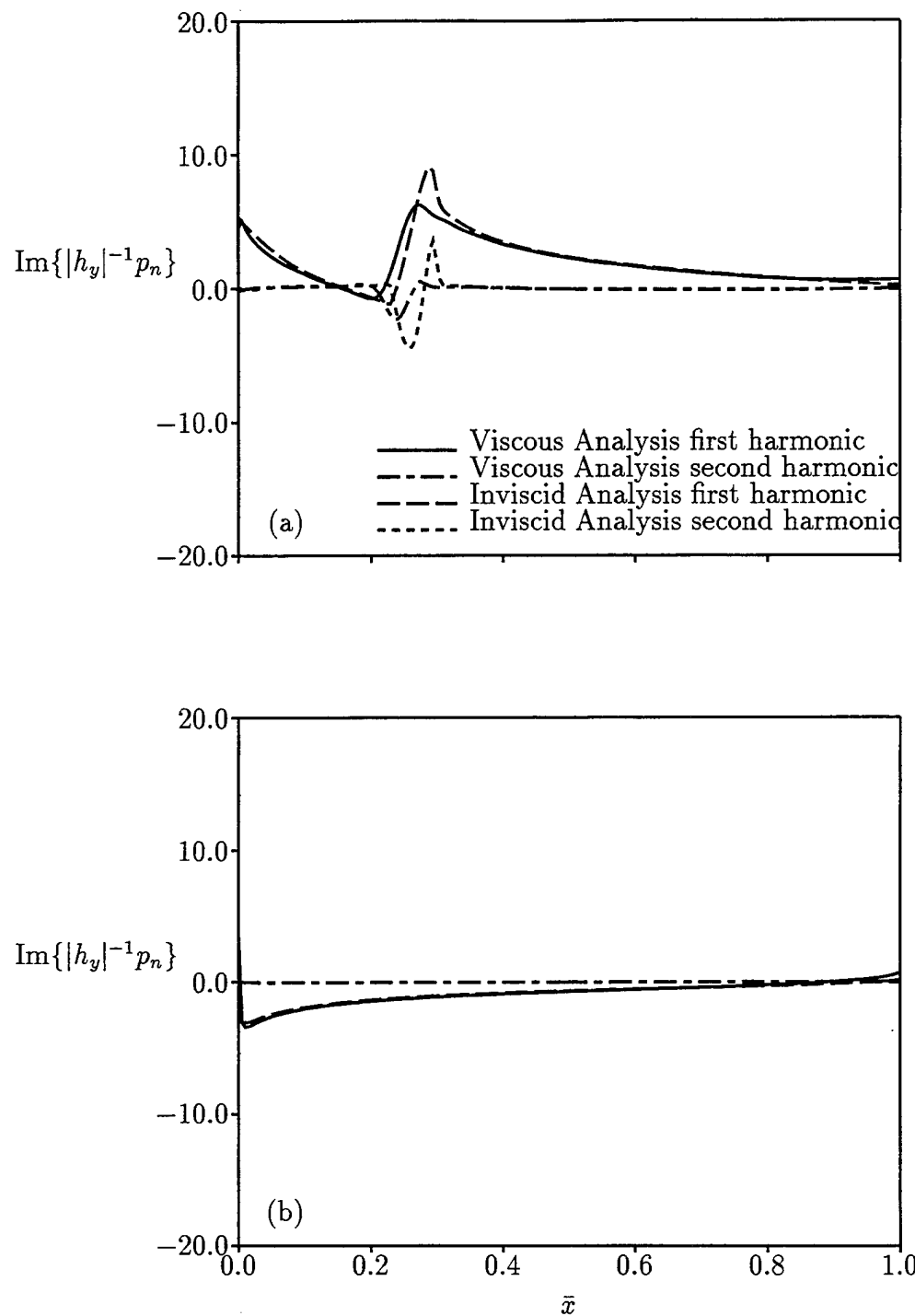


Figure 26: Imaginary components of the Fourier amplitudes of the unsteady surface pressure distribution for viscous (at $Re = 10^6$) and inviscid transonic ($M_{\infty} = 0.8$, $\Omega_{\infty} = 58$ deg) flows through the 10th Standard Cascade undergoing an out-of-phase bending vibration at $|h_y| = 0.01$, $\omega = 1$, and $\sigma = 180$ deg: (a) Suction surface; (b) Pressure surface.

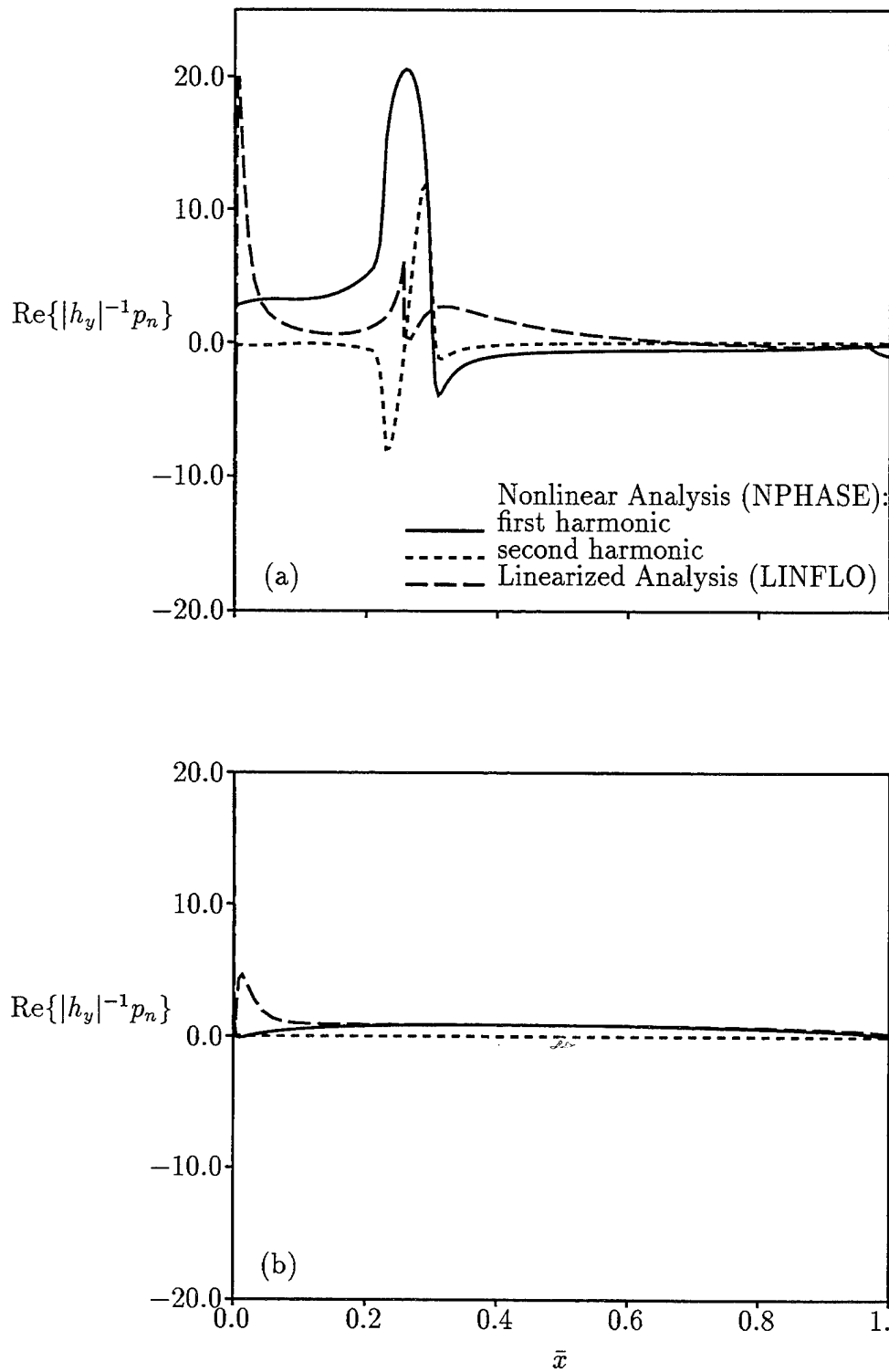


Figure 27: Real components of the Fourier amplitudes of the unsteady surface pressure distribution for inviscid transonic ($M_{\infty} = 0.8$, $\Omega_{\infty} = 58$ deg) flow through the 10th Standard Cascade undergoing an out-of-phase bending vibration at $|h_y| = 0.01$, $\omega = 1$, and $\sigma = 180$ deg: (a) Suction surface; (b) Pressure surface.

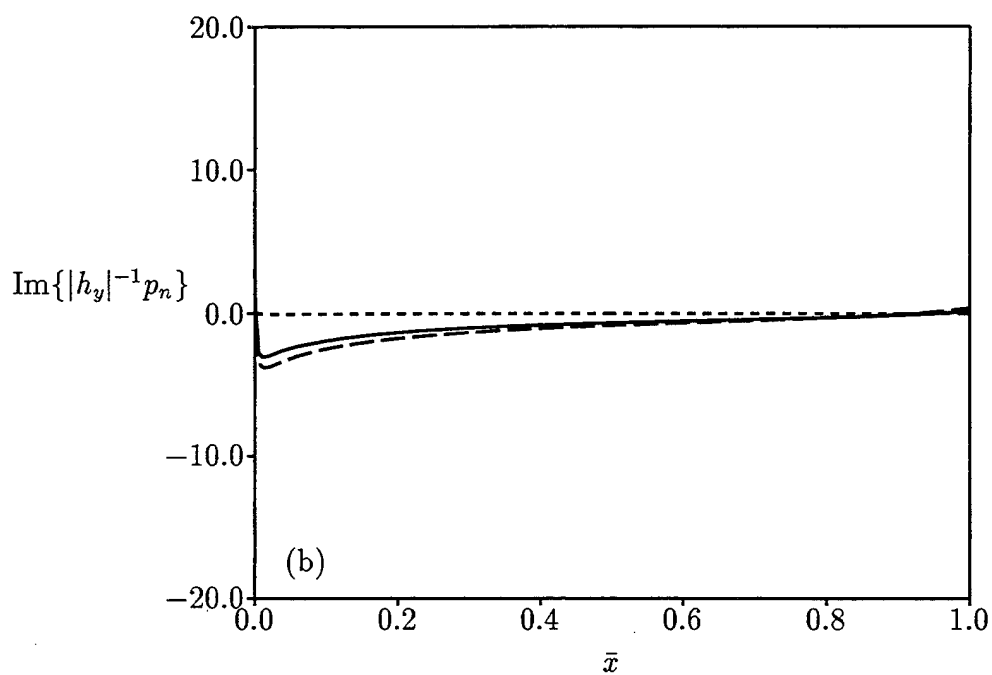
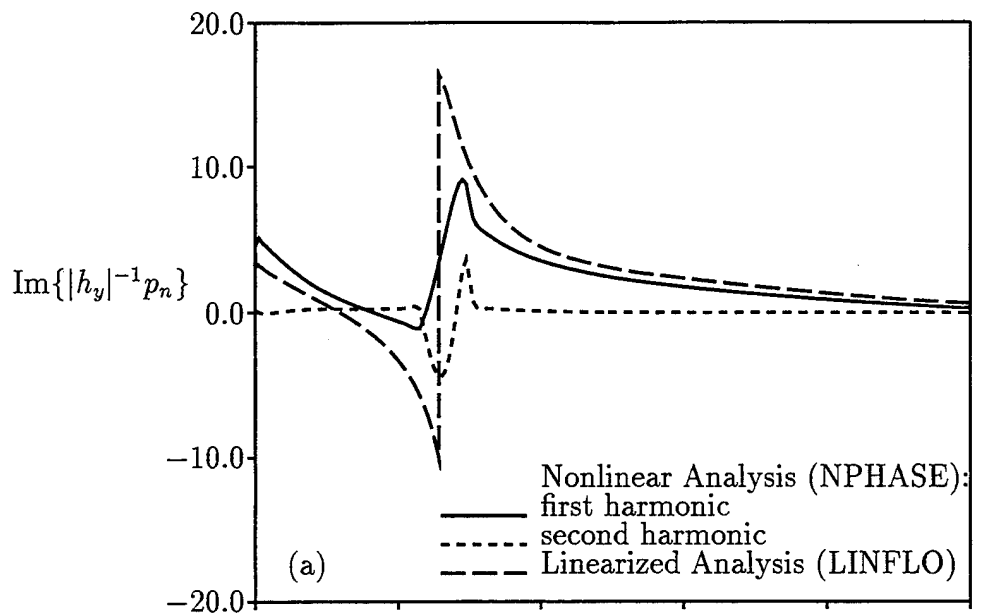


Figure 28: Imaginary components of the Fourier amplitudes of the unsteady surface pressure distribution for inviscid ($M_{\infty} = 0.8$, $\Omega_{\infty} = 58$ deg) flow through the 10th Standard Cascade undergoing an out-of-phase bending vibration at $|h_y| = 0.01$, $\omega = 1$, and $\sigma = 180$ deg: (a) Suction surface; (b) Pressure surface.

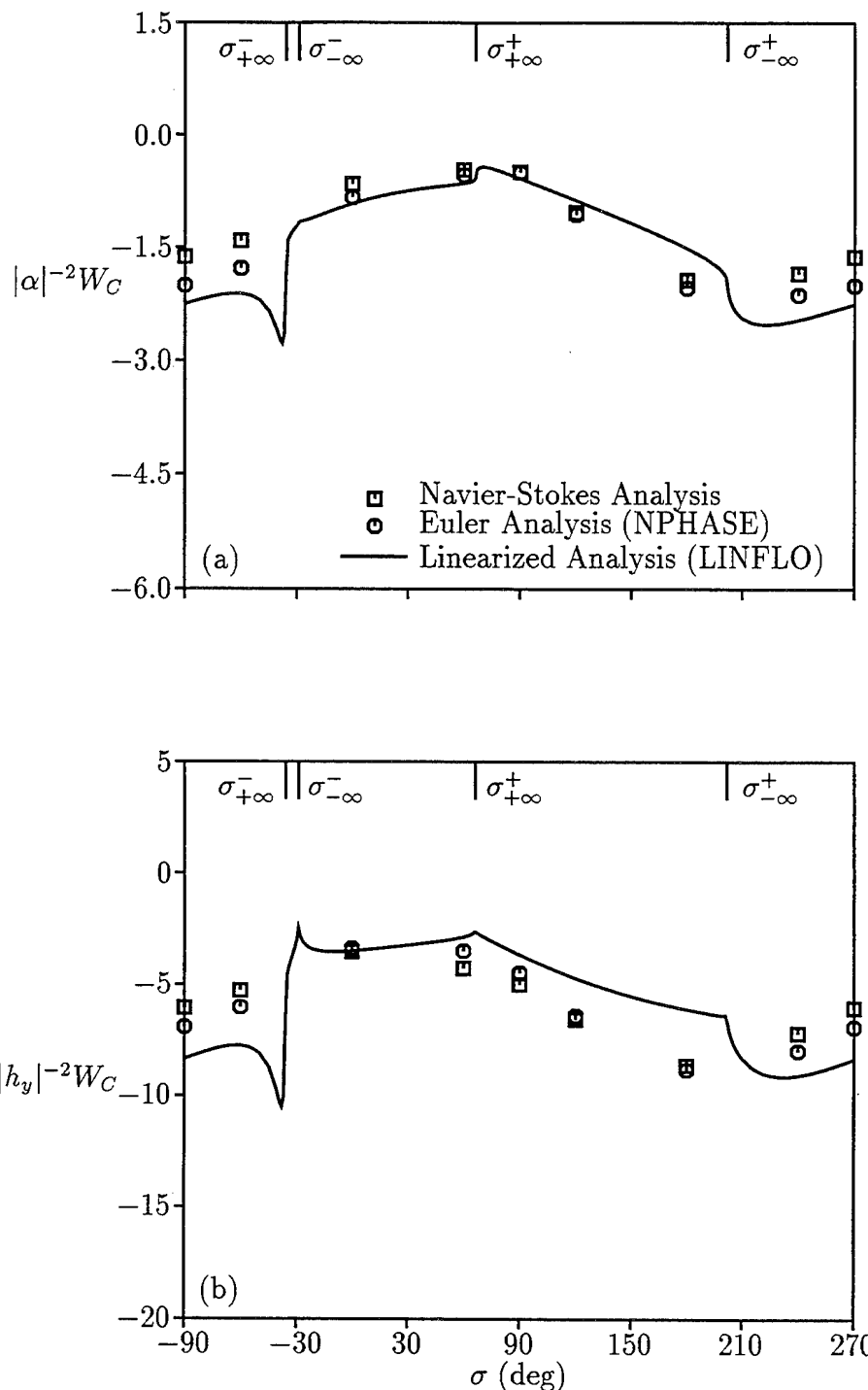


Figure 29: Work per cycle versus interblade phase angle for inviscid and viscous (at $Re = 10^6$) transonic flows through the 10th Standard Cascade undergoing prescribed blade motions at unit frequency ($\omega = 1$): (a) torsional vibrations at $|\alpha| = 1$ deg about midchord; (b) bending vibrations at $|h_y| = 0.01$.